UNIVERSITÀ DEGLI STUDI DI FIRENZE
DIPARTIMENTO DI FISICA
SCUOLA DI DOTTORATO IN SCIENZE

DOTTORATO DI RICERCA IN FISICA – XXI CICLO

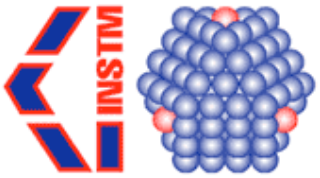

Magneto-optical studies of diluted systems of magnetic nanoparticles and single-molecule magnets

Tesi di Dottorato di
Rafael L. Novak

Tutors:
Prof.ssa Roberta Sessoli
Prof. Massimo Gurioli

Coordinatore:
Prof. Alessandro Cuccoli

Settore Scientifico-Disciplinare: FIS/03 - Fisica della Materia

27 dicembre 2008

Dedicated to my grandmother Fernanda.

“There is first of all the problem of the opening, namely, how to get us from where we are, which is, as yet, nowhere, to the far bank. It is a simple bridging problem, a problem of knocking together a bridge. People solve such problems every day. They solve them, and having solved them push on.
Let us assume that, however it may have been done, it is done. Let us take it that the bridge is built and crossed, that we can put it out of our mind. We have left behind the territory in which we were. We are in the far territory, where we want to be.”

J. M. Coetzee, *“Elizabeth Costello”*

Acknowledgments

First of all, I would like to thank Professors Roberta Sessoli and Andrea Caneschi for accepting my application for a PhD thesis in the Laboratory of Molecular Magnetism. It's been a great opportunity to work in a stimulating environment among excellent researchers. I also thank Prof. Dante Gatteschi for hosting me in his research group during these 3 years. I am grateful to all the members of the group for their support, fruitful scientific discussions and ideas. Claudio Sangregorio, Claudia Innocenti and Cesar de Julián Fernńdez for all the help they provided with the Physics of magnetic nanoparticles, and Dr. de Julián Fernández for helping with the experiments and measurements in the magneto-optics laboratory, as well as for finding and providing a never-ending amount of samples. Dr. Lorenzo Sorace and Dr. Maria Fittipaldi for the EPR spectra and all the help in their interpretation; Francesco Pineider and Dr. Matteo Mannini for all the Mn12 and Fe4 bulk and SAM samples, STM images, and discussions; Drs. Lapo Bogani and Lucia Cavigli for all they taught me about magneto-optics and the basic skills necessary to run an optics lab; Professor Massimo Gurioli for accepting being my co-supervisor, and for his help in the magneto-optics lab (lasers, alignment,...), and Professor Anna Vinattieri for giving a hand with practical issues that would come up every other day in the magneto-optics lab. Marco Neri from the Physics Department for technical support (gas handling, electronics) and for invaluable help when we stripped down the SPECTROMAG cryostat in order to clean its windows; and Dr. Marco Barucci for all the ideas, help and patience during the construction of the ac susceptometer, not to mention his invaluable technical expertise in cryogenics.

I thank Dr. Stergios Piligkos from the University of Copenhagen for providing the computer program used to analyze the MCD data, and for all the discussions concerning this part of my work. I should also thank Prof. Uwe Bovensiepen from the "Freie Universität Berlin" for giving some valuable tips about magneto-optical susceptometers; Profs. Vasily Oganesyan and Myles Cheesman from the University of East Anglia, and Prof. Eric McInnes from the University of Manchester, for very useful discussions about MCD measurements and the interpretation of the experimental data; Prof. Walter S. D. Folly, from the Federal University of Sergipe, for his suggestions and help with magnetic susceptibility measurements and electronics in general; Dr.

Patrick Rosa from the “Institut de Chimie de la Matière Condensée de Bordeaux”for suggestions concerning the susceptometer and the control software; Profs. João Paulo Sinnecker and Elis Sinnecker, from the Federal University of Rio de Janeiro, for discussions, and for providing me some nanoparticle samples; Profs. Miguel A. Novak from the Federal University of Rio de Janeiro, and Maria Vaz from “Universidade Federal Fluminense”(UFF), for their counseling, ideas and also for motivating me into doing my PhD work in the interesting field of Molecular Magnetism.

I am grateful to Prof. Andrea Cornia and to Dr. Chiara Danieli from the University of Modena for providing the Mn12 and Fe4 compounds necessary to prepare our polymer and SAM samples; and to Profs. G. Mattei, P. Mazzoldi and Dr. V. Bello from the University of Padova for the Ion-implanted nanoparticle samples.

I thank all the friends and colleagues from the LaMM group for all the good time together, in and out of the university: Francesco Pineider, Giordano Poneti, Lapo Gorini, Mael Etienne, Fabrice Pointillart, Kevin Bernot, Javier Luzon, Lisa Castelli, Ludovica Margheritti, Alessandra Beni, Rajaraman Gopalan, Francesco Carlà, Mario Rizzitano, as well as the visiting students: Eike, Diana, Anastasya and Francisco. I can’t forget to thank all my friends in Brazil, in special Rafael Monclar and Manoela Zanker.

This small paragraph is certainly not enough to express my gratitude for my family in Brazil, that despite the distance was always present and supportive, and always believed in my success: my parents Livia and Carlos, my grandparents Lidiya, Nicolas, Fernanda and Sergio, my stepfather Tarsis, my aunt Letizia, my uncles Fabio, Thomas, Miguel and Francesco. A special thanks also to our long time family friends Trude and Jochen.

I acknowledge the “Consorzio Interuniversitario Nazionale per la Scienza e Tecnologia dei Materiali” (INSTM) for the financial support.

Finally, I thank God.

Contents

List of Figures

List of Tables

1 Introduction

In the last decades the research community has witnessed the spectacular growth of nanoscience and nanotechnology, with its multitude of exciting new results and the prospect of spectacular technological applications brought to light by these. Surely, a long path has been trodden since R. P. Feynman gave his famous "There is plenty of room at the bottom" lecture in 1959, but even bigger breakthroughs should be expected as more and more scientists of different backgrounds commit themselves to this amazingly promising field of research. This interdisciplinarity caused nanoscience to branch out into many directions, comprising almost all the fields of Material Science and Condensed Matter Physics, in which new materials with different and even superior properties compared to their bulk counterparts are obtained and studied. Further progress is fostered by the development of new characterization techniques, scanning probe microscopies, and advances in nanofabrication both from the "top-down" as well as from the "bottom-up" approaches. The impact of nanoscience in current applied research areas such as spintronics, quantum computation and magnetic storage technologies cannot be overstressed. Among the many ramifications of Nanoscience, Nanomagnetism is the sub-field that deals with the preparation and characterization of magnetic materials in the nanoscale, for example nanoparticles, thin films and single-molecule magnets. From the pioneering studies of magnetic fine particle systems during the 1950's ([12], [13], [14], [15]) it evolved into a multidisciplinary field involving physicists, chemists, engineers and material scientists. Their combined efforts lead to novel preparation methods, physical characterization techniques and the ultimate goal, technical applications, not to mention the new insights on the basic physical processes underlying the phenomena observed in systems with reduced dimensions and dimensionalities including the possibility of studying quantum effects in carefully tailored model systems.

In this work two kinds of magnetic nanostructured systems will be studied: magnetic nanoparticles and single-molecule magnets. Magnetic nanoparticles offer multiple opportunities for experimentalist and theoreticians, as the magnetic properties of nanoparticles show strong size-dependent effects, important surface effects, enhanced coercivity compared to the bulk counterpart, and interesting optical properties that result from the peculiar electronic structure found

in these objects. The production of alloy nanoparticles allows the combination of interesting properties of each of the components, leading to multifunctional nanomaterials with one extra degree of freedom, the ratio of the components of the alloy. The subtle interplay between the intrinsic properties of nanoparticles and finite-size effects, as well as size distributions and inter-particle interactions still need clarification, making it a fertile ground for the willing theoretician. One important example of finite-size effect is superparamagnetism ([14],[16]), with significant implications in future high density data storage devices based in nanoparticles. Other examples of the exciting applications of magnetic nanoparticles may be found in magnetic refrigeration, sensing applications, permanent magnet design, quantum computation, spintronics and catalysis, not to mention the prospects found in the life sciences and therapeutic tools in medicine, bio-sensing, MRI contrast design, targeted drug delivery and cancer therapy through hyperthermia and thermoablation [17].

Single-molecule magnets are molecular systems made up of interacting paramagnetic centers (organic radicals or transitions metal ions) in which a combination of strong uniaxial anisotropy and high spin ground state give rise to slow relaxation of the magnetization and a blocked spin state under a certain temperature (in this case analogous to the superparamagnetic blocking temperature) in which the molecule will display magnetic hysteresis. In these materials the magnetic properties arise from the structure and the coupling between the paramagnetic centers, and are not generally given by the superposition of single-ion properties. These chemically synthesized nanomagnets represent an example of the "bottom-up"approach to the preparation of nanomaterials as they are obtained through synthetic chemistry pathways, in which the use of techniques of molecular and supramolecular chemistry gives the synthesizer the possibility of fine-tuning the magnetic properties in unprecedented ways. A great advantage of this approach is the possibility of synthesizing materials whose magnetic units are identical, with well defined properties and orientations in the case of single-crystals. Entire families of molecular magnets may be created with small variations in structure, anisotropy, compositions, etc, allowing comprehensive studies of magnetic properties, anisotropy, structural effects, and quantum effects, to cite some examples. A deep understanding of the fundamental properties of these molecules, the origin of their magnetic anisotropy and of the quantum tunneling of the magnetization, as well as the ways to organize them on functional structures is of fundamental interest for applications, as these materials are potentially important as a new generation of data storage devices in which each molecule could store a bit of digital information. Besides, molecular magnets may have several other interesting applications in spintronics [18],[19] and quantum computing [20],[21],[22], and even biomedical applications should not be ruled out.

It is evident that novel measurement and characterization techniques, or at least modified versions of old methods, with increased sensitivity and resolution, are needed as the dimensions of the physical systems get so reduced as to push the available "traditional" magnetic characterization techniques (SQUID, VSM, suceptometers) to their limits. In this sense, many new techniques have been developed in order to address the magnetism of nanostructures, as micro-SQUID [23] and micro-Hall probe magnetometry [24], not to mention the family of scanning probe microscopies (mainly STM and MFM), and synchrotron techniques (XAS, XMCD). Among the group of new versions of older methods, a classical example is the Surface Magneto-Optical Kerr Effect (SMOKE)[25], a powerful way of probing the magnetism of thin-films with high enough sensitivity to probe a monolayer. Furthermore, Magneto-Optical (MO) methods may be used as a spectroscopic tool, providing information about the electronic structure of the magnetic system (metals, alloys, oxides or molecules) under study through the optical transitions that contribute to the Kerr rotation or MCD spectrum. Among the many applications of Magneto-Optics, data storage is at the forefront, with MO techniques providing a fast and highly sensitive way of reading the spin polarization of magnetic molecules or nanoparticles organized in transparent media, a situation in which the use of bulky samples such as single crystals or oriented crystallites, is not convenient. Metallic, oxide or alloy nanoparticles, as well as molecular magnets, embedded in dielectric matrices may lead to the production of multifunctional materials with interesting optical and magneto-optical properties. Furthermore this offers the possibility of studying the individual constituents of otherwise bulk or crystalline systems in conditions closer to those found in spintronic devices. Powerful synthetic techniques, such as Sol-Gel or ion-implantation, are available and allow the production of nanoparticles with various compositions and dimensions. Chemical synthesis is also possible, as for example in [26], [27] and [28] in which M. Brust et al. demonstrate the chemical synthesis of thiol capped gold nanoparticles; and the Sol Gel method (the literature is extensive, a review may be found in [29]), a powerful way of synthesizing inorganic nanoparticles that will be further discussed in chapter 5. The flexibility of chemical synthesis may also allow the obtention of Single-Molecule Magnet samples in many different final forms, such as single-crystals, powders (polycrystalline) and nano-aggregates. This flexibility also offers the possibility of tailoring the affinity with the host material by employing appropriate ligands during the molecule preparation phase. So families of SMMs sharing the same magnetic core may be produced according to the target host into which they will be embedded. This example of molecular engineering leads to the possibility of studying these systems in several environments besides the single-crystal and powder that are traditionally studied. The small concentration and reduced number of constituents rules out

effects due to inter-particle interactions and so the resulting measurement will correspond to the average of truly single-particle (or molecule) properties.

In this work SMMs belonging to two different families, the Mn12 and the Fe4, were embedded in different non-crystalline environments (polymers, thin-films and self-assembled monolayers), in order to verify the optical addressability of their magnetism in these conditions [30]. As mentioned before, these assemblies also offer the possibility to study their constituents in highly diluted samples where inter-molecule interactions are insignificant. MCD characterization of the Fe4 molecule in the paramagnetic state was carried out. The same magneto-optical methods were applied to Co-Ni and Au-Fe magnetic alloy nanoparticles, that were characterized in silica hosts as well as in polymeric environments (the same used as hosts for the magnetic molecules). A Faraday/MCD magnetometer was used for most of the measurements, in addition to traditional magnetic characterization methods (SQUID, VSM, ac-susceptibility). A significant part of the work consisted in upgrading the Faraday/MCD magnetometer, enabling it to measure the magnetic ac-susceptibility of these diluted systems, which in many cases cannot be properly studied in traditional ac-susceptometers. The ac-susceptibility measurements, both traditional and MO, together with magnetization measurements, were employed to get deeper insight in the interaction of light with the magnetism of magnetic alloy nanoparticles. In these systems different magnetic responses are observed as the measurement is carried out by "traditional"(SQUID, VSM) or by MO means, evidencing the subtle interplay between optical and magnetic properties found in these materials. The influence of the surface plasmon resonance of the nanoparticles in their magnetization will be discussed.

In chapter 2 an introduction to magnetism and to the magnetic materials of interest here will be presented. We then proceed to chapter 3 in which the theory behind magneto-optic phenomena is presented. In chapter 4 the experimental methods employed in the magnetic and magneto-optical characterization of nanoparticles and single-molecule magnets will be presented, together with the description of the magneto-optical ac-susceptometer designed specifically for this purpose. In chapter 5 the results of the measurements done on nanoparticles will be shown and discussed. In chapter 6 the same will be done with the measurements of single-molecule magnets. Finally, in chapter 7 the general conclusions of this work will be drawn.

2 A brief introduction to magnetism and magnetic materials

In this chapter, a brief introduction to the physics behind magnetic phenomena will be presented, beginning with the magnetism of single ions, and then molecules and metallic nanoparticles. In this last case the treatment is phenomenological, following the treatments based on the Stoner-Wohlfart and the Neel-Brown models.

2.1 The magnetism of ionic systems

The magnetism of materials has its origins in the magnetic moment (spin and orbital) of electrons, a consequence of the electronic structure of atoms (or solids). The combination of spin magnetic moment ($\mu_{\mathbf{s}} = -g\mu_B \mathbf{s}_i$) and orbital magnetic moment ($\mu_{\mathbf{l}} = -\mu_B \mathbf{l}_i$) of single electrons in an atom, according to the Pauli principle and Hund's rules, give rise to the atomic magnetic moment $\mathbf{M} = -\mu_B(\mathbf{L}+2\mathbf{S}) = -g_J\mu_B\mathbf{J}$ where $\mu_B = 9.274\text{x}10^{-24}$ J/T is the Bohr magneton, $\mathbf{l}_i$ and $\mathbf{s}_i$ are the orbital and spin angular momenta of electron i, $\mathbf{L} = \sum_i \mathbf{l}_i$ and $\mathbf{S} = \sum_i \mathbf{s}_i$. $\mathbf{J}$ is the total angular momentum, arising from the coupling between the spin and the orbital angular momentum through the spin-orbit coupling: $\mathbf{J} = \mathbf{L}+\mathbf{S}$, with coupling energy given by $E_{SO} = \lambda \mathbf{L}\cdot\mathbf{S}$. The g-factor is then given by:

$$g = 1 + \frac{J(J+1)+S(S+1)-L(L+1)}{2J(J+1)} \tag{2.1}$$

equal to 2 for a free electron (the actual value is $g = 2.0023$ if QED corrections are considered). This approach to the spin-orbit coupling is known as the Russel-Saunders coupling, and is a good approximation for metals of the first transition series. The ground state of 3d single ions may then be labeled by the symbols ${}^{2S+1}L_J$ where $L = \sum_i m_{Li}$ and follows the spectroscopic labeling convention ($L = 0 \rightarrow S$, $L = 1 \rightarrow P$, $L = 2 \rightarrow D$, etc) and $S = \sum_i m_{Si}$. To give an example, the Mn(II) ion, with its 5 d-electrons, will have a ${}^6S$ ground state, the same as the Fe(III) ion. The macroscopic magnetization of a material, namely its response to an external

magnetic field, is defined as the density of magnetic moment $\mathbf{M} = \frac{1}{V}\sum_i \mu_i$ where V is the volume of the sample. For small fields, it is proportional to an external magnetic field $\mathbf{H}$: $\mathbf{M} = \chi\mathbf{H}$, where the quantity χ is the static magnetic susceptibility. More generally, the susceptibility is given by $\frac{\partial M}{\partial H}$. These relations are directly related to two methods of measuring the magnetic susceptibility of a material: in the first case (static), a small field is applied on the sample, the magnetization is measured and the susceptibility is determined from the relation $\chi = \frac{M}{H}$; in the second case, a small oscillating magnetic field is applied on the sample and its response gives the so called ac (or dynamic) susceptibility $\chi = \frac{\partial M}{\partial H}$. More details about this last method will be given in chapter 4, section 4.2, where the assembling of a susceptometer for this thesis work will be explained in more details.

The single-ion properties outlined above give rise to macroscopic magnetic behavior, immediately identified by susceptibility measurements. Atoms with a closed shell electronic structure (so that $L = S = 0$) give rise to diamagnetic behavior, characterized by a very small and negative temperature independent susceptibility. It may be regarded as originating from shielding currents induced by an applied field in the filled electron shell of ions. These currents are equivalent to a small induced magnetic moment with direction opposite to that of the external magnetic field. It is present in all materials, but generally obscured by stronger effects (paramagnetism, ferromagnetism, etc). In molecular compounds the diamagnetic contribution to the susceptibility arising from ions or groups of atoms is tabulated as the Pascal constants. The general formula for the diamagnetic contribution is:

$$\chi_D = -\frac{N\mu_0 e^2}{6m_e}\sum_i \langle r_i^2 \rangle \tag{2.2}$$

where $\langle r_i^2 \rangle$ is the mean-square distance of the ith electron from the nucleus, μ_0 is the permeability of the vacuum, N is the number of ions,m_e is the electron mass and e is the electron charge.

The presence of unpaired electrons in ions gives rise to paramagnetic behavior. In this case L and S have non-zero values, an applied magnetic field may magnetize the sample, and this magnetization will be given by the Brillouin function:

$$\begin{gathered} M = Ng\mu_B J B_J(\alpha) \\ B_J(\alpha) = \frac{2J+1}{2J} coth(\frac{(2J+1)\alpha}{2J}) - coth(\frac{\alpha}{2J}) \\ \alpha = \frac{g\mu_0\mu_B JH}{kT} \end{gathered} \tag{2.3}$$

This expression is obtained from the thermal average of the Boltzmann populations of the $2J+1$ levels of the ground state multiplet split by the magnetic field. At the high field limit ($\mu_0\mu_B H \ggg kT$) the magnetization reaches saturation, while at the low field limit ($\mu_0\mu_B H \lll kT$) the Brillouin function may be approximated by the first term of its series expansion:

$$B_J(\alpha) = \frac{J+1}{3J}\alpha + \frac{[(J+1)^2+J^2](J+1)}{90J^3}\alpha^3 + \ldots \tag{2.4}$$

so the magnetization will be given by:

$$M = Ng\mu_B JB_J(\alpha) = Ng\mu_B J\frac{J+1}{3J}\frac{Jg\mu_B\mu_0 H}{kT} = \frac{N\mu_0 g^2 J(J+1)\mu_B^2 H}{3kT} \tag{2.5}$$

Recalling that the susceptibility is given by $\chi = M/H$, dividing (2.5) by H we obtain the Curie law:

$$\chi = \frac{N\mu_0 g^2 J(J+1)\mu_B^2}{3kT} = \frac{C}{T} \tag{2.6}$$

where C is the Curie constant and $\mu_{eff} = g\mu_B\sqrt{J(J+1)}$ is defined as the effective magnetic moment. The Curie law as expressed by (2.6) is a consequence of the fact that the thermal average that yields (2.3) involves only the $2J+1$ equally spaced levels of the ground state multiplet split by the magnetic field. Deviations from the Curie behavior may be expected whenever more than these $2J+1$ levels are involved, or when these levels are no longer equally spaced in a magnetic field or degenerate in zero-field. The latter situation occurs when crystal fields come into play. The crystal field is the electrostatic field generated by the charge distributions of the other ions (part of the ligands) surrounding the magnetic ion in a coordination complex. The treatment of these interactions from an electrostatic point of view is know as the ligand field theory. In this framework the influence of the ligand orbitals is not taken directly into account in the description of the electronic structure of the ion, but is introduced as a perturbation through the Hamiltonian: $H = H_{el-el} + H_{LF} + H_{SO}$ where the first term describes the electron-electron repulsion, the second is the ligand field interaction and the third is the spin-orbit coupling. The distribution of neighboring charges has the symmetry of the crystal structure. As the orbitals of the magnetic ion are not spatially symmetric, some of them will feel more or less the repulsion of the neighbors, thus having their energies raised or lowered. This is the origin of the ligand field. For example, if a magnetic ion is in an octahedral environment surrounded by 6 negatively charged ligands, its orbitals dx^2-y^2 and dz^2 will have higher energies as they point to the ligands, while the dxy, dxz and dyz will lie lower in energy. This also gives rise to anisotropy, because the orbital moments will have preferred directions, and so the spin, which is coupled to

the orbital moment through the SO interaction. The combined contributions of spin-orbit coupling, exchange interactions and ligand fields can split the levels of a ground state multiplet (for systems with $S > 1/2$) even at zero applied magnetic field, giving rise to the so-called zero-field splitting (ZFS). As the energies involved lie within the range of UV and visible (UV-Vis) light, this fact gives rise absorption of wavelengths corresponding to transition energies and so to the characteristic colors of coordination compounds containing 3d metal ions. For 3d metal ions, however the ligand field and the electron-electron repulsion term are more important and the SO coupling may be treated perturbatively. The states are then labeled as $^{2S+1}\Gamma_\gamma$, where S is the total spin and Γ_γ are the labels of the irreducible representation of the point group symmetry of the molecule induced by the orbital component.

At this point it is convenient to introduce the spin Hamiltonian (SH) description of a magnetic system. With this approach the system is described only by spin coordinates and tensors describing the effect of zero-field splitting (**D**), the g factor (**g**) and the exchange coupling **J**. The influences of the orbital part and of the chemical surrounding are inserted by means of these parameters. Other terms such as the hyperfine interaction between electrons and nuclei, and higher order anisotropy terms may be also included. A typical spin Hamiltonian for a system of N magnetic ions is given by:

$$H = -\mu_B \sum_{i=1}^{N} S_i g_i H - \sum_{i,k\neq i}^{N/2} S_i J_{ik} S_k + \sum_{i=1}^{N} S_i D_i S_i \tag{2.7}$$

in which the first term is the Zeeman term, describing the interaction of the spin system with an external magnetic field, the term in the middle is the exchange term, describing the exchange interactions between the spins (ferromagnetic interactions have $J > 0$, antiferromagnetic interactions have $J < 0$) and the last is the crystal field term.

In the case of clusters containing more than 1 magnetic ion, the SH approach is still valid. The cases of interest here are those in which the ions are strongly coupled through exchange interactions, giving rise to a "giant spin". In this case the tensors **D** and **g** are derived from complex combinations of the single-ion parameters according to the appropriate coupling scheme between the magnetic moments of the ions. In this case, for a system with N spins S_i ferromagnetically coupled to give a total spin $S = NS_i$ the following relations can be demonstrated:

$$\begin{aligned} \mathbf{D_S} &= \sum_i d_i \mathbf{D_i} + \sum_{i<j} d_{ij} \mathbf{D_{ij}} \\ d_i &= \frac{2S_i - 1}{N(2NS_i - 1)} \; ; \; d_{ij} = \frac{2S_i}{N(2NS_i - 1)} \\ H &= \sum_i \mathbf{S_i} \cdot \mathbf{D_i} \cdot \mathbf{S_i} + \sum_{i<j} \mathbf{S_i} \cdot \mathbf{D_{ij}} \cdot \mathbf{S_j} \end{aligned} \tag{2.8}$$

An appropriate way to treat the problem is then to write the crystal field term as:

$$H_{CF} = \mathbf{S} \cdot \mathbf{D} \cdot \mathbf{S} \tag{2.9}$$

where **S** is the total spin operator and **D** is a real, symmetric tensor [4]. It has therefore 3 orthogonal eigenvectors. If the coordinate axes are chosen parallel to these eigenvectors, **D** is diagonal and (2.9) takes the form:

$$H_{CF} = D_{xx} S_x^2 + D_{yy} S_y^2 + D_{zz} S_z^2 \tag{2.10}$$

Subtracting $(1/2)(D_{xx} + D_{yy})(S_x^2 + S_y^2 + S_z^2) = (1/2)(D_{xx} + D_{yy})S(S+1)$ we obtain:

$$H_{CF} = D S_z^2 + E(S_x^2 - S_y^2) \tag{2.11}$$

where

$$D = D_{zz} - \frac{1}{2} D_{xx} - \frac{1}{2} D_{yy} \; ; \; E = \frac{1}{2}(D_{xx} - D_{yy}) \tag{2.12}$$

Subtracting the constant $DS(S+1)/3$ from (2.11) we obtain:

$$H_{CF} = D\left[S_z^2 - \frac{1}{3} S(S+1)\right] + E(S_x^2 - S_y^2) \tag{2.13}$$

This last equation crystal field term is traceless and if one introduces the eigenvectors $|m\rangle$ of S_z, defined by $S_z|m\rangle = m|m\rangle$, it is easily seen that the second term of (2.11) has no diagonal elements ($\langle m|S_x^2 - S_y^2|m'\rangle$) if $m' = m$ while the first term of (2.11) has no off-diagonal elements. Introducing a parameter B so that (2.11) can be rewritten using the raising and lowering operators S_+ and S_- as:

$$H_{CF} = D S_z^2 + \frac{B}{4}(S_+^2 + S_-^2) \tag{2.14}$$

we can use the alternative notation $H_{CF} = -D' S_z^2 + B S_x^2$ where $D' = -(D + B/2)$.

If a further approximation is considered, that of axial symmetry, it follows from (2.12) that $D_{xx} = D_{yy}$ and $E = 0$, so the crystal field part of the spin Hamiltonian (2.11) may be written as:

$$H_{CF} = D S_z^2 \tag{2.15}$$

In axial symmetry only the D parameter defined by (2.12) is necessary to express the energies of the $(2S+1)$ spin levels of the S multiplet within this approximation. The effect of this Hamiltonian term is that of splitting the $(2S+1)$ levels even in the absence of an applied magnetic field, being then called the zero-field splitting. These properties lead to the simplification of the perturbative treatment of the second term in (2.11) if $|E|$ is sufficiently smaller than $|D|$ ($-1/3 \leq E/D \leq +1/3$). At $E/D = 1/3$, $D_{xx} = 0$, $D_{yy} = -2D/3$, $D_{zz} = 2D/3$ and the splitting between the 3 components is maximum (maximum rhombic splitting). At $E/D = 1$, $D_{xx} = D_{zz} = 2D/3$ and $D_{yy} = -4D/3$. The x and z axes are now equivalent and the system is axial with y as unique axis (the axis have simply been renamed in this case, with the system having axial symmetry).

The eigenvectors of (2.11) or (2.13) in axial symmetry ($E = 0$) are the eigenvectors $|m\rangle$ of S_z, with eigenvalues $W(m) = Dm^2 - S(S+1)/3$. At this level of approximation $W(m) = W(-m)$. Including a non-zero E (reducing the symmetry below the axial one) the $|m\rangle$ and $|-m\rangle$ states remove their degeneracy if S is integer, while if S is half-integer they remain degenerate in pairs (Kramers doublets). Finally, D can be positive or negative: in the former case the levels with lowest $|m|$ are the most stable, while for negative D the levels with high $|m|$ lie lowest. So positive D corresponds to an easy-plane magnetic anisotropy and negative D to easy-axis magnetic anisotropy.

2.2 Magnetic Nanoparticles

Magnetic nanoparticles are clusters containing from a few hundreds up to some thousand of atoms, with typical diameters lying in the range from a few nanometers up to hundreds of nanometers. The presence of elements that normally order ferromagnetically in bulk (Fe, Co, Ni) is necessary, while alloying with other elements gives a further possibility of tailoring the structural and magnetic properties of these materials. The striking novel properties observed in these materials arises from the reduced dimensions (size-effect) and from the high surface-to-volume ratio, with surface effects dominating the properties of very small nanoparticles. Ensembles of single-domain nanoparticles, in which each nanoparticle behaves as a giant spin, are the current subject of intense research as they present several interesting phenomena (superparamagnetism, enhanced magnetic moment and coercivity, spin-glass behavior, tunnel magnetoresistance, Coulomb blockade) and yet the mechanisms that give rise to these novel properties (especially surface effects, modified electronic structure and interparticle interactions) are not totally understood.

In ferromagnetic materials, the minimization of the magnetostatic energy due to free poles at the material boundary gives rise to the domain structure. Domains are regions of uniform magnetization separated by boundaries called domain walls (or Bloch walls). Two processes dominate the magnetization process: the displacement of domain walls, and the rotation of the magnetization vector. The first process, when irreversible, gives rise to hysteresis with very low coercivity in these materials, while the second process may be reversible or irreversible, and leads to the saturation of the magnetization. In this last process the magnetization vector must be rotated against the anisotropy if the field is not applied parallel to one of the easy axes. This causes the saturation of the magnetization to be attained only for applied fields high compared to the anisotropy field. In case the anisotropy is high enough, a high magnetic field will be necessary to overcome the anisotropy energy barrier, both for the nucleation of reversed domains and for the rotation of the magnetization vector. This process leads to a significant increase in the coercivity, as found in high performance permanent magnets such as SmCo and NdFeB based materials. In figure 2.1 a very simple domain structure consisting of two domains with magnetizations differing by 180° is depicted. The transition region between the two uniform magnetization domains is the domain wall. In this figure, the process of wall motion is shown, with the wall moving from right to left. The details behind domain wall motion, dynamics and conformations are beyond the scope of this work. It is enough to say that the domain wall thickness (regardless of the DW geometry) results from the competition between the exchange and the anisotropy energy, and is given by (2.17). The exchange interactions (see (2.16)) will favor a parallel orientation of adjacent magnetic moments, while the anisotropy will favor moments parallel to the easy axes of the crystal. It is clear then that the former favors a wide DW, while the last favors narrow walls. This balance gives the domain wall thickness, which is strongly dependent on the material composition and displays large variations, typically from 10nm to a few hundreds of nanometers.

$$E_{ex} = -\sum_{i \neq j} J_{ij} S_i \cdot S_j \tag{2.16}$$

$$E_{dw} \propto \sqrt{\frac{J}{K}} \tag{2.17}$$

where J is the exchange energy and K is the anisotropy energy constant present in series expansions for the anisotropy energy of the form: $E_{an} = K_1 \sin^2\theta + K_2 \sin^4\theta + K_3 \sin^6\theta + \cdots$. As an example, for magnetocrystalline anisotropy K_1 corresponds to Δ_{SO}, the difference between spin-orbit energies along an easy and a hard axis.

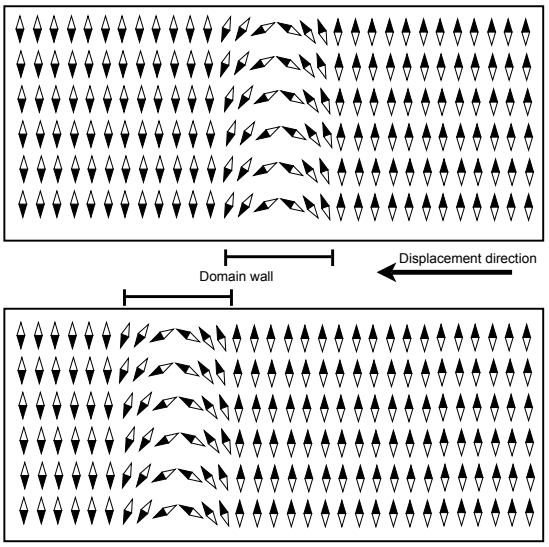

Figure 2.1: Two magnetic domains separated by a 180° domain wall. The movement of this wall is occurring from right to left.

If the volume of small particles made of ferromagnetic materials is below a certain critical value, the energy employed to generate a domain wall may be larger than the magnetostatic energy due to the free poles at the boundaries. In this case, the particle will have only one magnetic domain, being called a monodomain (or single-domain) particle, even in the absence of an applied field. For spherical particles, the characteristic diameter under which single-domain is formed is given by (2.18):

$$d = \frac{18E_\sigma}{\mu M_S^2} \tag{2.18}$$

where $E_\sigma = 2\sqrt{(K/A)}$ is the domain wall energy and M_S is the saturation magnetization. Typical values of this critical diameter are 15 nm for iron, 35 nm for cobalt, 55 nm for Ni, reaching values as high as 100 nm for NdFeB and 750 nm for $SmCo_5$ [16].

In this case the particle may be regarded as a "giant spin"and the magnetization reversal is governed by the rotation of this "giant spin", the sum of all the magnetic moments, against the anisotropy of the particle. This anisotropy may have several sources:

- Magnetocrystalline : This is intrinsic to the material and has its origin in geometry of the crystal and the spin-orbit coupling. The orbitals in the atom will have their degeneracy lifted according to their orientations with respect to lattice directions (analogous to the

crystal field effects in single ions introduced in the previous section), and the atomic spin "senses" this through the spin-orbit coupling.

- Shape : This has magnetostatic origin, and is due to the presence of magnetic poles on the boundary of a magnetized body. These poles create a demagnetizing field, which interacts with the magnetization originating the magnetostatic energy $E_{demag} = -\vec{M} \cdot \vec{H}_D$. The demagnetizing field H_D depends on the geometry of the sample and in general is lower for poles far from each other.

- Surface : The atoms that form the surface of a nanoparticle are in a lower symmetry environment with respect to the rest of the crystal, notably with a smaller number of nearest neighbors. This introduces a new coupling of atoms to the environment through both spin-orbit coupling and exchange, giving rise to anisotropy with crystal field origin, analogous to magnetocrystalline anisotropy. Another source of surface anisotropy may be the strains induced by lattice deformations at the surface, which couples to the magnetostriction and give rise to an additional anisotropy (see the next item). Surface anisotropy is the dominant source of anisotropy for very small particles due to the high surface-to-volume ratio. In fact, for particles with diameter under 10 nm a significant percentage of the atoms are located on the particle's surface and so this will be the main source of anisotropy.

- Stress : This anisotropy is due to the presence of magnetostriction, the process by which a magnetized body changes its length in the direction of magnetization. In the opposite case, magnetization changes may be induced by stress. This gives rise to an additional term in the anisotropy energy.

- Exchange and dipolar : magnetic dipolar interactions may introduce anisotropy related to the relative positions of two particles. The exchange interaction may act in the same fashion, if the particles are close enough.

The anisotropy of a nanoparticle depends, then, on all these contributions, and the resulting overall anisotropy may be approximated, in most cases, as uniaxial ([31], [16], [32]), which means that there is an easy axis for the magnetization, and has the form (see, for example, [15], where the problem of the magnetization of an ensemble of non-interaction uniaxial magnetic particles was treated for the first time by E. C. Stoner and E. P. Wohlfarth; or [12], [13] and [14] where the problem of single-domain particles at thermal equilibrium is treated; other references

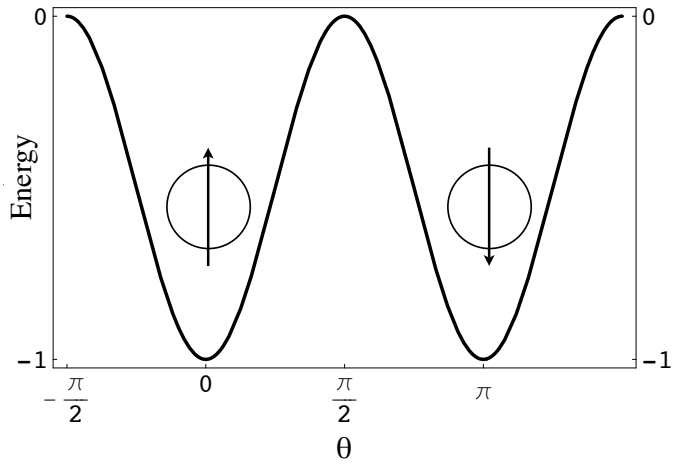

Figure 2.2: The anisotropy energy barrier for a nanoparticle with uniaxial anisotropy. The barrier height is given by KV.

are [33], [16], [34], [35], [36], [32]):

$$E_{an} = -KV\cos^2\theta \tag{2.19}$$

where K is the anisotropy energy per unit volume, V is the particle's volume and θ is the angle between the easy-axis and the particle magnetization. The energy barrier given by (2.19) is plotted in figure 2.2. The two minima correspond to the magnetization parallel or anti-parallel to the easy-axis of the particle. If an external magnetic field ($\vec{H} = H_0(\sin\theta_0\cos\phi_0, \sin\theta_0\sin\phi_0, \cos\theta_0)$) is applied in a direction making an angle θ_0 with the easy-axis (taken to be parallel to the z axis), the energy of the nanoparticle will be given by:

$$\begin{aligned} E = E_{an} + E_{mag} = -K\cos^2\theta - \vec{M}_s\cdot\vec{H} = \\ -\frac{M_s}{2}[H_k\cos^2\theta + 2H_0(\sin\theta\sin\theta_0\cos\phi\cos\phi_0 + \sin\theta\sin\theta_0\sin\phi\sin\phi_0 + \cos\theta\cos\theta_0)] \end{aligned} \tag{2.20}$$

where the anisotropy field $H_k = \frac{2K}{M_s}$ was introduced, and M_s is the saturation magnetization. The geometry of the problem may be seen in figure 2.3. In order to find the minima as a function of θ and ϕ, we first calculate:

$$\begin{aligned} \frac{\partial E}{\partial\phi} &= -M_sH_0(-\sin\theta\sin\theta_0\cos\phi_0\sin\phi + \sin\theta\sin\theta_0\sin\phi_0\cos\phi) = 0 \\ &\sin\theta\sin\theta_0\sin(\phi_0-\phi) = 0 \\ &\therefore \sin(\phi_0-\phi) = 0 \end{aligned} \tag{2.21}$$

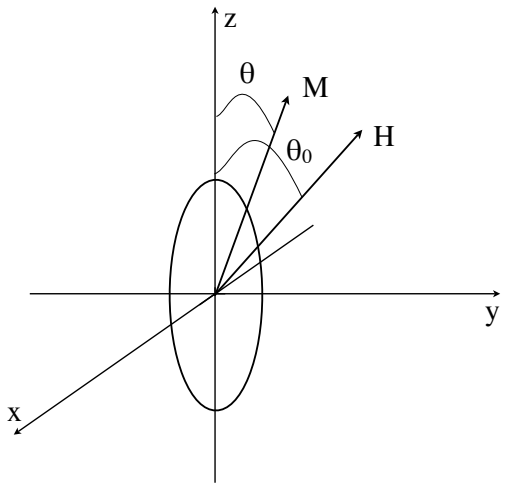

Figure 2.3: The geometry of the problem. The nanoparticle is represented as an ellipsoid centered at the origin, the applied field vector $\vec{H}$ and the magnetization $\vec{M}$ at angles of θ_0 and θ to the z axis, parallel to the easy-axis of the particle.

showing that the magnetization and the applied field must lie on the same plane. This fact allows (2.20) to be simplified:

$$\begin{aligned} E &= -\frac{M_s}{2}[H_k \cos^2\theta + 2H_0 \cos(\theta_0 - \theta)] = \\ &\quad -\frac{M_s}{2}[H_k \cos^2\theta + 2H_z \cos\theta + 2H_{xy} \sin\theta] \\ H_z &= H_0 \cos\theta_0 \\ H_{xy} &= H_0 \sin\theta_0 \end{aligned} \tag{2.22}$$

The effect of a magnetic field applied parallel to the easy-axis on the potential barrier is given by (2.22, with $H_{xy} = 0$. It is depicted in figure 2.4. It is clear that for very high field values (with respect to the anisotropy) only one side of the double well will be populated, and the particle will become magnetized in that direction.

In case the thermal energy is low compared to the height of the barrier ($kT \ll KV/k$), the magnetic field may be turned off and the particle will remain magnetized. A magnetic field must then be applied in the other direction in order to cancel or reverse the magnetization. In this situation, in which the magnetization relaxation is too slow compared to the characteristic time window of the measurement, the particle is said to be in the blocked state. A measurement of magnetization in function of applied field will result in a hysteresis cycle, but in this case not

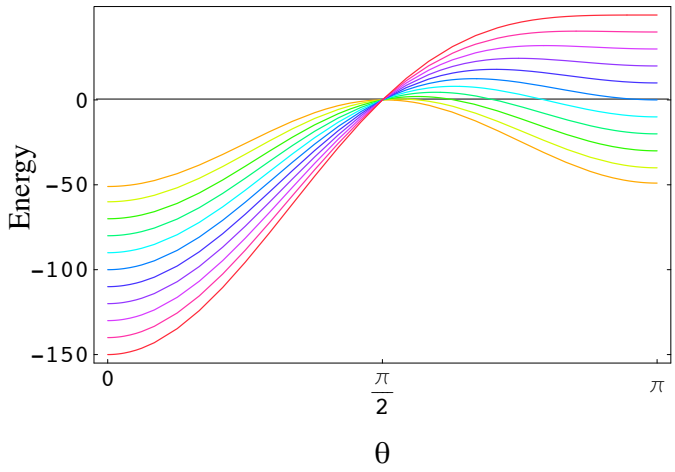

Figure 2.4: The effect of an applied magnetic field on the anisotropy barrier. The double minima potential well under zero field is represented in orange.

originating from domain wall movement as in a bulk material, but from the anisotropy barrier being higher than the thermal energy. As the energy necessary to overcome the barrier is much higher than the typical energy to displace a domain wall, superior coercive fields and remanent magnetizations may be achieved in nanoparticle ensembles, two important factors for designing permanent magnets. As the temperature is raised, kT increases, increasing the probability of the magnetic moment jumping above the barrier, causing the particle's magnetization to relax faster and faster. When it becomes of the order of the anisotropy energy barrier KV/k, the particle magnetic moment will fluctuate and no net magnetization will be observed unless an external magnetic field is applied. Under the influence of an external magnetic field the magnetization will be given by the classical Langevin function:

$$M = M_s L\left(\frac{\mu H}{kT}\right) = M_s coth\left(\frac{\mu H}{kT}\right) - \frac{kT}{\mu H} \tag{2.23}$$

μ is the magnetic moment of the particle. In this state the static susceptibility follows the Curie law:

$$\chi = \frac{M_s^2 V}{3kT} \tag{2.24}$$

Both the Langevin function dependence of the magnetization and the Curie law for the susceptibility are results obtained for a paramagnet with magnetic moment arising from a spin 1/2. The only difference here is that the magnetic moment for a nanoparticle is very high, resulting from the sum of the magnetic moments of the $10^2 - -10^4$ atoms found in the nanoparticle. As

this state resembles the behavior of a paramagnetic substance, it is called superparamagnetic state. The temperature at which the transition from blocked to superparamagnetic state is called the blocking temperature, T_B. It is important to stress that the blocking temperature is strongly dependent on the characteristic time window of the measurement employed to probe the system's magnetization. Very fast measurements, like Mössbauer spectroscopy, may yield, for the same sample, very high blocking temperatures compared to slower techniques such as SQUID magnetometry.

Superparamagnetic relaxation, the process by which the magnetization of a nanoparticle changes, can occur in different ways. Coherent rotation is the mode described in the pioneering work by Stoner and Wohlfarth [15], in which all the magnetic moments inside the particle rotate in unison during magnetization reversal, leaving the exchange energy constant. The other two modes, curling and buckling, cause the exchange energy to increase, while they decrease the magnetostatic energy. Considering that the exchange interaction is a short-range interaction, while magnetostatic forces (dipolar) are long-ranged, large particles should present relaxation modes that minimize the magnetostatic energy, such as curling or buckling. Small particles (smaller than $\sim 20-30$nm), on the other hand, relax preferably through coherent rotation, so this is the main relaxation mode for very small particles, like the ones we have studied in this thesis.

The first systematic studies of the temperature dependence of the relaxation times of magnetic nanoparticles systems date back to L. Néel in 1949. He considered single-domain particles with uniaxial anisotropy and magnetization reversal occurring by coherent rotation. He associated the superparamagnetic relaxation time, τ, to an Arrhenius law:

$$\tau = \tau_0 e^{\frac{KV}{kT}} \tag{2.25}$$

where τ_0 is a pre-exponential factor of the order of 10^{-9} - 10^{-12} s for ferromagnetic particles, and is related to the attempt frequency with which the magnetic moment tries to overcome the barrier. This was further refined by Brown (the Néel-Brown model), Aharoni and Coffey, but the results obtained by these last differ only in the pre-exponential factor τ_0. The formula for the relaxation time obtained by Brown ([13], [31]) is:

$$\tau = \tau_0 \frac{\sqrt{\pi}}{4} \left(\frac{kT}{KV}\right)^{\frac{3}{2}} e^{\frac{KV}{kT}} \tag{2.26}$$

It can be assumed that the different pre-exponential factors in (2.25) and (2.26) have little importance since the temperature dependence of the relaxation time is governed by the exponential. The strong dependence of the blocking temperature on the time scale of the measurement is evident from (2.25). If τ_m, the experimental time-window, is much longer than τ, the relaxation

time of the nanoparticle assembly, the outcome of the measurement will be a time average of the magnetization and the particles will be in the superparamagnetic state. On the other hand, if $\tau \gg \tau_m$, the relaxation will be so slow that only static properties are observed (as in a bulk magnetized crystal) and the particles will be in the blocked state. Within this framework, T_B may be defined as the temperature at which $tau = \tau_m$. As mentioned before, T_B will depend on the measurement technique, being higher for faster measurements. If the same experimental technique is employed, it will increase for higher anisotropy energy barriers, or for larger particles [32].

$$T_B = \frac{KV}{kln(\frac{\tau_m}{\tau_0})} \tag{2.27}$$

For example, SQUID magnetometry, with a characteristic measurement time of the order of 100 s, gives (for $\tau_0 = 10^{-9}$ s, a typical value) $ln(\tau_m/\tau_0) = 25$ while Mössbauer spectroscopy, with $\tau_m \sim 10^{-8}$ s, yields $ln(\tau_m/\tau_0) = 4$. $T_B^{Moss}/T_B^{SQUID} \sim 6.25$, demonstrating that a fast measurement technique yields blocking temperatures much higher than a slow one. There are many ways of determining the blocking temperature, covering several decades in the measurement time window, from the slow magnetometric measurements ($\tau_m \sim 100$ s) to ac susceptibility ($\tau_m \sim 10 - 10^{-5}$ s) and the very fast spectroscopic techniques such as Ferromagnetic Resonance ($\tau_m \sim 10^{-9}$ s) and Mössbauer spectroscopy ($\tau_m \sim 10^{-8}$ s, but only useful for systems containing iron, cobalt or nickel). The most typical are relaxation (magnetometric) and ac susceptibility measurements. In a relaxation measurement, the magnetization is saturated with a high magnetic field and then its time evolution is measured with a magnetometer, after the field is removed. The time dependence should follow an exponential law like $M(t) = M_0 exp(-t/\tau)$, characteristic of a thermally activated process [37]. In ac susceptibility measurements the in-phase (χ') and out-of-phase (χ'') components of the magnetic susceptibility are measured in a wide range of frequencies (typically from 0.1 Hz up to 100 kHz), thus making a wide range of characteristic measurement times available to the experimentalist (more details about this technique are found in chapter 4, section 4.2). The susceptibility may be written as $\chi(\omega) = \chi'(\omega) + i\chi''(\omega)$, with χ' (in-phase component) being related to the susceptibility and χ'' (out-of-phase component) to dissipation, being related to the fact that a hysteresis cycle opens. The onset of the imaginary part, with a frequency dependent maximum, is a signature of the transition from superparamagnetic to blocked state. The maximum of χ'' in function of measurement frequency at a certain temperature T yields the value of τ (the inverse of the frequency at which the maximum is observed, as χ'' has a maximum at $\omega = 1/\tau$) for that temperature. This is valid for the idealized case of an assembly of monodispersed particles, namely, particles with the same dimensions. In

a typical assembly of single-domain nanoparticles, however, a characteristic distribution of particle volumes is always present. This distribution generally follows a log-normal law, as shown in 2.28 [16]:

$$f(V) = \frac{1}{\sqrt{2\pi}\sigma V} exp\big[-\frac{ln^2(V/V_0)}{2\sigma^2}\big] \tag{2.28}$$

where V_0 is the average particle volume and σ is the standard deviation of V. This implies a distribution of energy barriers and of blocking temperatures, so if a certain measurement technique is employed to probe the magnetism of the system, a fraction of the nanoparticles will appear blocked while another fraction will appear superparamagnetic. Thus, for real systems, the measurement yields an average blocking temperature. In this case, the magnetization decay $M(t)$ introduced above must be substituted by:

$$\begin{aligned} M(t) &= \frac{1}{Z}\int_0^\infty M_0 e^{(\frac{-t}{\tau})} V f(V) dV \\ Z &= \int_0^\infty V f(V) dV \end{aligned} \tag{2.29}$$

which enormously complicates the interpretation of the experimental data. In many cases the relaxation of the magnetization may be interpreted by the following logarithmic law [16]:

$$M(t) = M(0)(1 - S(T,H) ln(t/\tau_0)) \tag{2.30}$$

in which $S(T,H) = kT f(E_c)$ is defined as the magnetic viscosity, and $f(E_c)$ is the distribution of energy barriers equivalent to the volume distribution (2.28). For temperatures much lower than T_B the viscosity is expected to be linear with T. Its physical meaning, however, is still a matter of discussion, and equation (2.30) is only valid if we assume that the distribution of energy barriers $f(E_B)$ is nearly constant in the range that can be observed during the measurement time. Other distributions of energy barriers give rise to other time dependencies in (2.30), power laws or stretched exponentials, to cite a couple of examples. The size distribution also complicates the analysis of the ac susceptibility data, because the position of the maximum of χ'' (and also of χ') depend on the shape of this distribution. In this case the temperature dependence of χ_{ac} is given by:

$$\chi(T,\omega) = \frac{1}{Z}\int_0^\infty \chi(T,\omega) V f(V) dV \tag{2.31}$$

where Z is defined in (2.29) and $f(V)$ is the distribution of particle volumes. $\chi f(V) dV$ is the contribution to the total ac susceptibility of particles with volumes comprised between V and $V + dV$. Several models have been proposed to explain the temperature dependence of the susceptibility for a given distribution of particle sizes ([38], [31]), but no one is fully able to account

for the complexity of an actual ensemble of magnetic nanoparticles. Despite these complications, ac susceptibility measurements is a very powerful technique for studying the magnetization dynamics in magnetic nanoparticle systems. It covers a broad range of measurement times and since a very small magnetic field is employed the energy barrier is only slightly modified.

A complete understanding of the magnetic properties of these nanoscopic systems is not simple, in particular because of the complexity of real nanoparticle assemblies, involving particle size distributions, magnetic interparticle interaction and different contributions to the magnetic anisotropy. Magnetic interparticle interactions may have magnetostatic origin (dipolar interactions), or in case the matrix where the nanoparticles (NPs) are dispersed is conductive, RKKY[1] or exchange effects may be important.

2.3 Single-Molecule Magnets

2.3.1 The Mn12 cluster

The $Mn_{12}O_{12}(CH_3COO)_{16}(H_2O)_4$ (Mn12Acetate, or Mn12Ac) was the first molecule to display SMM behavior [39], and has been intensely studied due to the multitude of interesting physical phenomena it shows, the most striking of all being the macroscopic tunneling of the magnetization [40],[41]. A combination of a high spin $S = 10$ ground state and an easy-axis type anisotropy arising from zero-field splitting of the ground state manifold gives rise to slow relaxation of the magnetization below 3K, and magnetic hysteresis of dynamic origin. The molecule's magnetic core has 4 Mn(IV) ions with $S = 3/2$ organized in a cubane structure and 8 Mn(III) with $S = 2$ bridged by oxide and carboxylate groups. The structure of this compound is shown in figure 2.5. Exchange interactions create a ferrimagnetic ground state, with all the Mn(III) and Mn(IV) ions aligned parallelly if they have the same oxidation number, and anti-parallelly in they have different numbers (2.5). The zero-field splitting value, D, is of the order of $-0.5\ \text{cm}^{-1}$. The 21 M levels of the ground state multiplet are then split in zero magnetic field (figure 2.6), with the $M_s = \pm 10$ lying $\sim 50\text{cm}^{-1}$ lower than the $M_s = 0$ level (the energy difference between states with highest and lowest $|M|$ value is given, for integer spin, by $\Delta = |D|S^2$, see for example (2.13) and (2.15) [4],[42]). This creates an energy barrier for the magnetization reversal that, when the temperature is so low that the thermal energy is smaller than the barrier height, blocks it in one direction. This gives rise to a hysteresis loop that is strongly dependent on the measurement

[1] Rudermann-Kittel-Kasuya-Yosida, a coupling mechanism of localized inner d or f electron spins through the conduction electrons

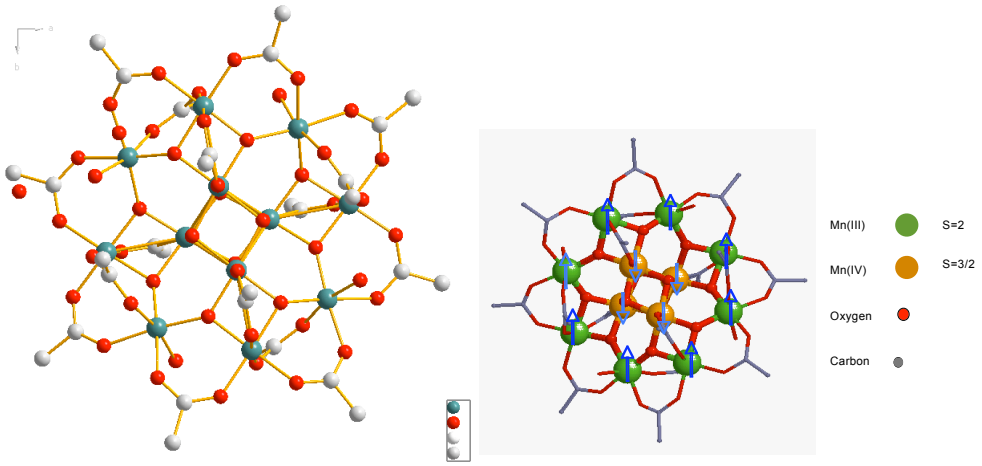

(a) View along the c-axis.

(b) The magnetic core. The arrows show the spin configuration in the ground $S = 10$ state.

Figure 2.5: The structure of the Mn12Ac cluster.

timescale and on the temperature, a behavior analogous to superparamagnetism, with the magnetization relaxation time given by an Arrhenius law $\tau = \tau_0 e^{\frac{\Delta}{kT}}$ (2.25). But the magnetization reversal process is not only thermally activated, with quantum tunneling of the magnetization playing a major role, giving rise to the characteristic stepped hysteresis loop seen in figure 2.6. The steps correspond to field values in which energy levels at both sides of the double well cross, and tunneling between these accelerates the relaxation. These field values are given by $H_n = \frac{nD}{g\mu_B}[1 + \frac{A}{D}(m^2 + m'^2)]$, where the second term in brackets is related to fourth order terms in the spin Hamiltonian. Without all levels would be aligned simultaneously. The tunneling may be thermally activated, which means that the spin is excited from a higher level, and then tunnels if this level is aligned with another on the other side of the well; or it may originate directly from the ground state at very low temperatures. The knowledge of the mechanism involved in tunneling is fundamental, as it is one of the processes that must be suppressed in order to achieve high blocking temperatures. The other conditions are a high spin ground state and a high uniaxial anisotropy barrier.

2.3.2 The Fe4 cluster

Another interesting family of single-molecule magnets is the Fe4 family. It is a tetranuclear iron(III) cluster with an $S = 5$ ground state at low temperatures and easy-axis magnetic anisotropy,

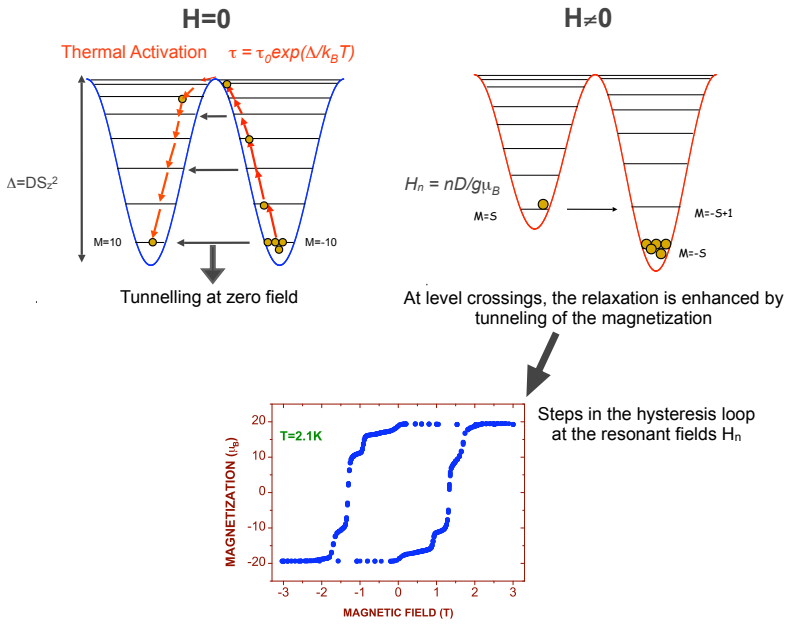

Figure 2.6: The spin energy levels of the Mn12Ac cluster, at zero field and under an external magnetic field. The thermally activated reversal process is indicated by red arrows on the left panel, while the tunneling at zero field is depicted with black arrows. On the right-hand side a level crossing is depicted. In this case resonant tunneling between the crossed levels increases the relaxation rate and a step is seen in the hysteresis loop at the resonant field, given by $H_n = \frac{nD}{g\mu_B}$.

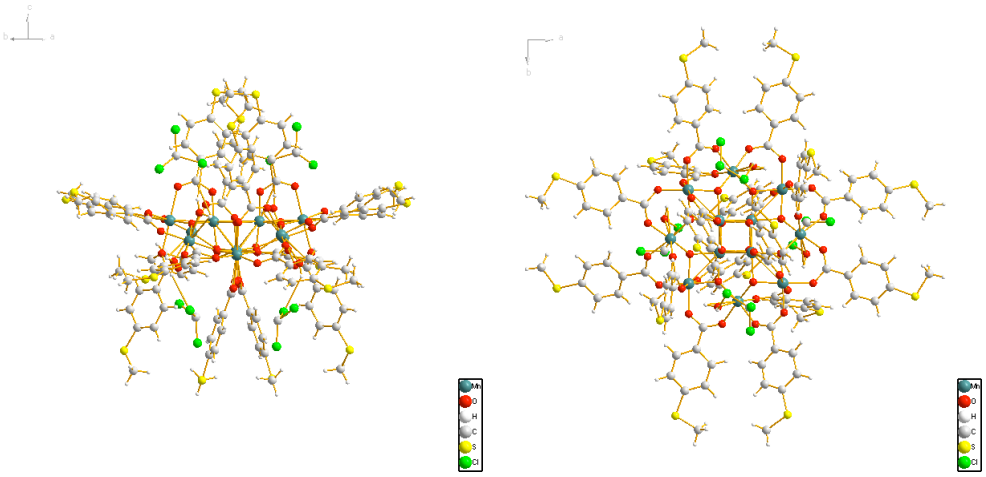

(a) View along an axis making 45° with the a-axis. (b) View along the crystallographic c-axis.

Figure 2.7: Structure of the Mn12PhSMe derivative.

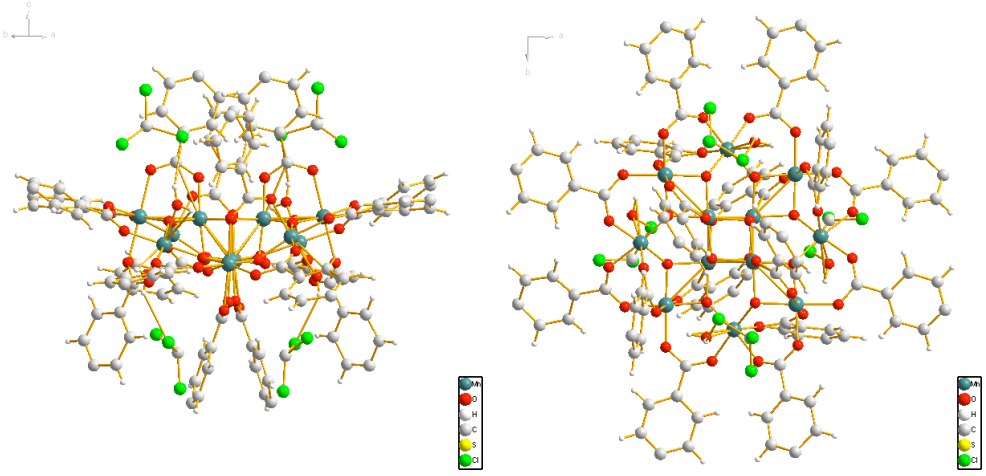

(a) View along an axis making 45° with the a-axis. (b) View along the crystallographic c-axis.

Figure 2.8: Structure of the Mn12Bz derivative.

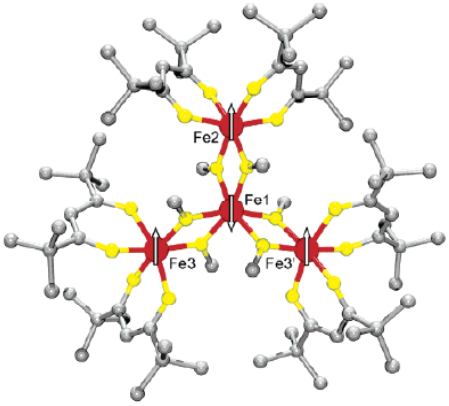

Figure 2.9: The molecular structure of compound **I**, with Fe ions in red, O in yellow and C in gray. The arrows show the spin configuration in the ground $S = 5$ state. From [1]

two conditions required for slow magnetic relaxation and SMM behavior. The compound displays superparamagnetic-like behavior. The blocking temperature is, however, very low, typically below 1K. The first synthesized compound has formula $Fe_4(OCH_3)_6(dpm)_6$ (Hdpm = dipivaloylmethane), **I**, but many other derivatives are know. The magnetic part of the cluster is shaped like an isosceles triangle (or a propeller, or even a star) with one Fe ion at its center (Fe_1) bridged by μ-methoxide ligands to 3 other Fe ions at the vertexes (Fe_2, Fe_3 and $Fe_{3'}$) (see figure 2.9). The magnetic coupling is antiferromagnetic between the central and the peripheral ions, and ferromagnetic between the peripheral ions, with the later coupling much weaker than the former ($J_2/J_1 \sim 0.1$). The total spin resulting from this combination of the $S = 5/2$ spins of the four Fe ions in equal to 5 [43].

The results presented in this work were obtained working with two derivatives of **I**, in which the six methoxide bridges in **I** were substituted by different ligands. In one case, the methoxide groups were exchanged with the tripod ligand H_3L = 11-(acetylthio)-2,2-bis(hydroxymethyl)-undecan-1-ol [44] (figure 2.10), or shortly C9SAc, which yields a compound (herein called **II**) with 2 long alkyl chains on both faces of the plane defined by the 4 iron ions that can be grafted on gold surfaces by the self-assembly method thanks to the . In the other case the substitution was made with a tripod containing a phenyl group, that we will call **III** (see, for example, [1], where it is depicted as H_3L^3). These substitutions not only may lead to the functionalization of the Fe4 cluster, but are also capable of enhancing its energy barrier, demonstrating the strong magnetostructural correlation present in these compounds. It was demonstrated in [45]

and [1] that the energy barrier may be increased from about 7K in **I** to 17K in the derivative with the tripod 1,1,1-tris(hydroxymethyl)ethane. This can be exploited to produce, for example, compounds with higher barriers and so higher blocking temperatures.

II was employed in most of the polymeric samples measured, as it is the derivative used to produce self-assembled monolayers of Fe4 on Au surfaces. It has a good solubility in the polymers used (PMMA, PS, PDMS) and so forms samples with good optical quality and no agglomerates. The same may be said about **III**, with the advantage that its synthesis is simpler, as the ligand in this case in commercially available.

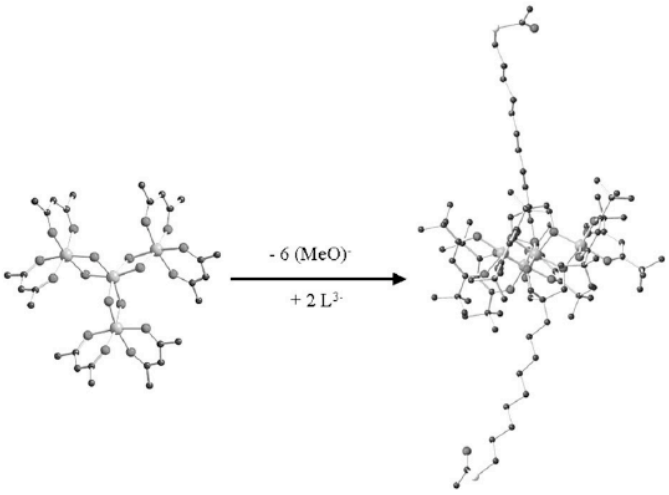

(a) The ligand substitution in compound **I**.

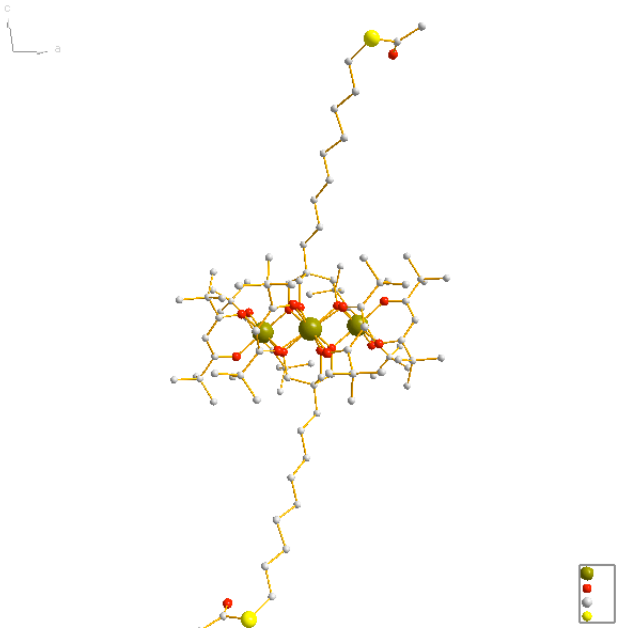

(b)

Figure 2.10: The ligand substitution that yields compound **II**, and its molecular structure. From [2]

3 Magneto-Optics

The field of Magneto-Optics (MO) consists in the study of the interaction between light and magnetized matter. The first attempts to find a relation between a propagating beam of polarized light and a magnetized material were made by M. Faraday in 1845, after a series of unsuccessful experiments conducted by himself and other scientists during the first half of the nineteenth century focused on studying the interaction between light and electrical fields. After he decided to substitute magnetic for electric forces he was able to observe the magneto-optical effect that would subsequently bear his name, the Faraday Effect. He essentially observed a magnetic field-dependent change in the polarization plane of a beam of polarized light after it passed through a glass ("a silicoborate of lead") placed in a magnetic field, with the angle of rotation given by the simple formula $\theta(\omega) = V(\omega)Hl$[1] [46]. Thirty-two years after, the Rev. John Kerr discovered that light reflected from a polished electromagnet pole also presented a rotation in the plane of polarization, an effect that would come to be know as the Kerr effect. Faraday, after his discovery, wrote in his diary that "This fact will most likely prove exceedingly fertile, and of great value in the investigation of conditions of nature force"[47],[25], while Kerr, in response to the perplexity of his presenter that, during the ceremony to award him the Royal Medal for his research results, observed that it was a wonder how he could have learned so much with the "comparatively simple and ineffectual apparatus at his disposal", stated "Simple it may be, but not ineffectual; rude, but not crude.". Faraday's and Kerr's words could not have been more prophetical and epitomize more the essence of these techniques, as they put together experimental simplicity and a great power of in-depth analysis of magnetic and electronic properties of a great variety of systems allied to a very high sensitivity. In fact, Magneto-Optics grew to become an important research field with great impact in nanosciences. Magneto-optical techniques such as the Faraday rotation, MOKE (Magneto-Optic Kerr Effect), SMOKE (Surface Magneto-Optic Kerr Effect), MCD (Magnetic Circular Dichroism) are important tools in the investigation of magnetic properties of thin-films (with monolayer sensitivity in some cases) and surface magnetism [25](and references therein), magnetic nanoparticles [48], [49], [50], [51], [52], [53],

[1] H is the applied magnetic field, l is the sample's thickness and $V(\omega)$ is the Verdet constant

biochemistry of metalloproteins [54], [55], [56], diluted magnetic semiconductors [57], and superconductor physics [58], [59], to cite some examples. Imaging of magnetic domains can be achieved by SMOKE microscopy techniques **cite** and Surface Near-field Optical Microscopy (SNOM), when combined to SMOKE, is a powerful way to visualize magnetic structures at the nanoscale **cite**. And to mention technological applications, magneto-optical data storage disks have been available for a long time as back-up solutions for computer systems and portable music player storage devices (Sony Minidisc ®); and optical isolators based on the Faraday effect are commonplace components in every fiber optics datalinks that literally keep the world "online".

In this chapter we are going to introduce the basic properties of an electromagnetic wave and its interaction with magnetized matter from a classical viewpoint. The Jones matrices, useful to represent the states of polarized light beams are going to be introduced and a phenomenological treatment will be given to the Faraday and the Kerr effects. At the end a small section will be dedicated to the quantum theory of Magnetic Circular Dichroism (MCD).

3.1 The Jones Formalism

Magneto-optic effects are experimentally detected as changes in the polarization state of a light beam after it is reflected by or transmitted from a magnetized medium. It is, then, very convenient to have a "toolbox"mathematical framework to represent polarization states and devices that change them. Exactly with this purpose in mind, R.C. Jones introduced the Jones matrix formalism in 1941 [60]. It uses 2 element column matrices (the Jones vectors) to represent a polarization state of light, and 2x2 matrices to represent optical devices that act upon these vectors.

An electromagnetic plane wave propagating through a homogeneous medium along the z direction will have its electric field $\mathbf{E}$ lying on the xy plane. Its general representation as a Jones vector is then given by:

$$\mathbf{J} = \begin{pmatrix} E_{0x}e^{i(kz-\omega t)} \\ E_{0y}e^{i[(kz-\omega t)+\phi]} \end{pmatrix} = \begin{pmatrix} A_x \\ A_y e^{i\phi} \end{pmatrix} \tag{3.1}$$

where A_x and A_y are complex numbers, ϕ is real, k is the wave vector (parallel to z) and ω is the angular frequency. The vector (3.1) corresponds to an elliptical polarization on the plane perpendicular to k (the xy plane in our coordinate system), which is the most general state of polarization light. This means that $\Re\mathbf{J}(z_0,t)$ describes an elliptic trajectory during propagation.

There are two particular cases: when $\phi = 0$ both components of (3.1) oscillate in phase and the polarization is linear; when $\phi = \pi/2$ and $A_x = A_y$, the polarization is circular. Taking advantage of the fact that multiplying the components of (3.1) does not change the polarization state, we can normalize (3.1) for the sake of convenience. So the normalized Jones vector for linearly polarized light making an angle α with the x axis is given by:

$$\hat{\mathbf{J}} = \begin{pmatrix} \cos(\alpha) \\ \sin(\alpha) \end{pmatrix} \tag{3.2}$$

The two normalized vectors representing the linear basis, with linear polarizations parallel to the x and y axes, respectively, are:

$$\hat{\mathbf{X}} = \begin{pmatrix} 1 \\ 0 \end{pmatrix} \text{ and } \hat{\mathbf{Y}} = \begin{pmatrix} 0 \\ 1 \end{pmatrix} \tag{3.3}$$

Another useful basis is the circular basis, which uses the two normalized Jones vectors representing left (LCP) and right-circularly polarized light (RCP):

$$\hat{\mathbf{L}} = \frac{1}{\sqrt{2}} \begin{pmatrix} 1 \\ i \end{pmatrix} \text{ and } \hat{\mathbf{R}} = \frac{1}{\sqrt{2}} \begin{pmatrix} 1 \\ -i \end{pmatrix} \tag{3.4}$$

where the $1/\sqrt{2}$ factors are orthonormalization factors.

A general state of elliptical polarization is given by the following vector:

$$\begin{pmatrix} \cos(\beta) \\ \sin(\beta) e^{i\phi} \end{pmatrix} \tag{3.5}$$

It describes an ellipse with generic orientation α with respect to the x axis given by $\tan 2\alpha = \frac{2\tan\beta\cos\phi}{1-\tan\beta^2} = \tan 2\beta\cos\phi$. If $\phi = \pi/2$ (3.5) becomes:

$$\begin{pmatrix} \cos(\beta) \\ i\sin(\beta) \end{pmatrix} \tag{3.6}$$

which represents an elliptically polarized wave with the principal axes parallel to the x and y coordinate axes and with ellipticity given by $\tan\beta$.

As stated before, in this formalism the optical elements that act upon light polarization are represented by 2x2 matrices. Some of these matrices are going to be presented here, as they will

be used to connect the measured magneto-optic signal to the physical quantities of interest (Kerr rotation or MCD, see chapter 4, subsection 4.1.4).

The most elementary optical elements used in polarimetric measurements are linear polarizers, wave plates (retarders) and the photoelastic modulator, which is just a wave plate with periodic time-varying retardance. The matrices corresponding to these elements are:

$$\begin{pmatrix} 1 & 0 \\ 0 & 1 \end{pmatrix} \tag{3.7}$$

The vector $\mathbf{E}^{'}$ resulting from the action of general matrices $\mathbf{O_1}$, $\mathbf{O_2}$, ..., $\mathbf{O_i}$ on the incoming vector $\mathbf{E}$ is:

$$\mathbf{E}^{'} = \mathbf{O_i} \ldots \mathbf{O_2 O_1 E} \tag{3.8}$$

3.2 A classical (and phenomenological) description of the magnetized medium

Phenomenologically, magneto-optic effects can be understood as the result of changes in the elements of the macroscopic dielectric tensor $\vec{\varepsilon}$ of a medium that cause the appearance of off-diagonal terms. These are created by a magnetization caused by magnetic ordering (ferro- or antiferromagnetic) and/or by an external magnetic field [61],[62],[46],[25]. The dielectric tensor summarizes the linear response of the medium and depends on the molecular (or crystalline) structure of the material, as well as bulk properties like temperature and density. This approach to light-matter interaction allows the calculation of macroscopic parameters that can be directly related to experimental observations [63], [61],[64]. We start from Maxwell's equation in a dielectric medium:

$$\begin{aligned} \nabla \cdot \mathbf{D} = \rho \; ; \nabla \cdot \mathbf{B} = 0 \; ; \\ \nabla \times \mathbf{E} = -\frac{\partial \mathbf{B}}{\partial t} \; ; \nabla \times \mathbf{H} = \frac{\partial \mathbf{D}}{\partial t} + \mathbf{J} \end{aligned} \tag{3.9}$$

Since at optical frequencies the magnetization cannot follow the high-frequency magnetic field of the electromagnetic wave, the relative permeability may be approximated by $\mu_r \sim 1$ and $\mathbf{B} = \mu_0 \mathbf{H}$ [65], [62]. so that, using this and the fact that $\mathbf{D} = \varepsilon_0 \mathbf{E} + \mathbf{P} = \vec{\varepsilon}\mathbf{E}$ ($\vec{\varepsilon} = \varepsilon_0(1+\chi) = \varepsilon_r$, the relative dielectric tensor), (3.9) become:

$$\begin{aligned} \nabla\cdot\mathbf{E} &= -\frac{1}{\varepsilon_0}\nabla\cdot\mathbf{P}\ ;\ \nabla\cdot\mathbf{H}=0\ ; \\ \nabla\times\mathbf{E} &= -\mu_0\frac{\partial\mathbf{H}}{\partial t}\ ;\ \nabla\times\mathbf{H}=\vec{\varepsilon}\frac{\partial\mathbf{E}}{\partial t} \end{aligned} \tag{3.10}$$

assuming that the medium is electrically neutral and non-conducting. Taking the curl of the $\nabla\times\mathbf{E}$ equation, and substituting $\nabla\times\mathbf{H}$ we obtain the following wave equation:

$$\nabla(\nabla\cdot\mathbf{E})-\nabla^2\mathbf{E}=-\mu_0\varepsilon_0\vec{\varepsilon}_r\frac{\partial^2\mathbf{E}}{\partial t^2} \tag{3.11}$$

A plane wave solution like: $\mathbf{E}(\mathbf{r},t)=\mathbf{E}_0e^{i(\mathbf{k}\cdot\mathbf{r}-\omega t)}$ yields the following equation:

$$n^2E_j-\sum_i\left(\varepsilon_{ji}E_i+\frac{k_jk_i}{k_0^2}E_i\right)=0 \text{ for } i,j=x,y,z, \tag{3.12}$$

that relates the components of the dielectric tensor $\vec{\varepsilon}$ to the complex refraction index $n=n'+in''=\frac{|\mathbf{k}|}{k_0}$ where $k_0^2=\varepsilon_0\mu_0\omega^2$ is the square of the vacuum wave vector. The resulting expression for the electric field is then:

$$\mathbf{E}(\mathbf{r},t)=\mathbf{E}_0e^{-n''\mathbf{k_0}\cdot\mathbf{r}}e^{i(n'+\mathbf{k_0}\cdot\mathbf{r}-\omega t)} \tag{3.13}$$

where n', the real part of the refractive index, causes the phase velocity of light to change and the imaginary part, n'', is seen to describe the absorption of light by the medium, the absorption coefficient being $2n''k_0$. Both n' and n'' are experimentally accessible.

Now we turn to the dielectric tensor. In general its form depends on the structural symmetry of the medium. In the simplest case of cubic symmetry it reduces to $\varepsilon_{ij}=\varepsilon\delta_{ij}$. But if we assume that the medium has a static magnetization $\mathbf{M}$, spontaneous in case the material is ferro- or antiferromagnetic, and in more general cases induced by an external magnetic field, the overall symmetry of the system changes, thus changing $\vec{\varepsilon}$. This effect may be described, in a first approximation, by ([62], [61], [63]):

$$\varepsilon_{ij}(\omega)=\varepsilon^0_{ij}(\omega)+\Delta\varepsilon_{ij}(\omega,\mathbf{M}) \tag{3.14}$$

where $\varepsilon_0(\omega)$ is the tensor in the absence magnetization. If we expand $\Delta\varepsilon(\omega,\mathbf{M})$ in a series in $\mathbf{M}$ up to second order:

$$\Delta\varepsilon_{ij}(\omega,\mathbf{M})\equiv\sum_{k=1}^{3}K_{ijk}(\omega)M_k+\sum_{k=1}^{3}\sum_{l=1}^{3}G_{ijkl}(\omega)M_kM_l, \tag{3.15}$$

we may define $\mathbf{K}(\omega)$ and $\mathbf{G}(\omega)$ as the linear and the quadratic magneto-optic tensors [62]. So, for a cubic crystal (in which $\vec{\varepsilon_{ij}}^{0}(\omega) = \delta_{ij}\varepsilon^0(\omega)$) with magnetization in the z direction ($\mathbf{M} = (0,0,M_z)$) and elements given by (3.14) and (3.15) the dielectric tensor will be the following:

$$\varepsilon(\omega,\mathbf{M}) = \begin{pmatrix} \varepsilon^0 + G_{12}M_z^2 & KM_z & 0 \\ -KM_z & \varepsilon^0 + G_{12}M_z^2 & 0 \\ 0 & 0 & \varepsilon^0 + G_{11}M_z^2 \end{pmatrix} \tag{3.16}$$

where the following contraction of indices $jk \to l$ was used for the $\mathbf{G}$ tensor elements: $(1,1) \to 1$; $(2,2) \to 2$; $(3,3) \to 3$; $(1,2) \to 4$; $(2,3) \to 5$; $(1,3) \to 6$. The elements are in general complex, $\varepsilon_{ij}(\omega) = \varepsilon'_{ij}(\omega) + \varepsilon''_{ij}(\omega)$, depend on the magnetization and must satisfy the Onsager relations [62],[25],[46], as the electric field is invariant under time-reversal transformations, while the magnetic field changes sign (antisymmetric):

$$\varepsilon_{ij}(\omega,-\mathbf{M}) = \varepsilon_{ji}(\omega,\mathbf{M}) \tag{3.17}$$

which means that the diagonal components of this tensor are even functions of $\mathbf{M}$, while the off-diagonal ones are odd functions of $\mathbf{M}$. Considering a light wave propagating in the medium with wave vector $\vec{k} = k\hat{z}$, and $\mathbf{M} \parallel \hat{z}$ (the Faraday geometry), we can substitute (3.16) in the eigenvalue equation (3.12) to obtain the following pair of equations:

$$\begin{cases} (n^2 - \varepsilon^0)E_x) - \varepsilon_{xy}E_y = 0 \\ \varepsilon_{xy}E_x + (n^2 - \varepsilon^0)E_y = 0 \end{cases} \tag{3.18}$$

where the small second order G_{ijkl} terms from 3.16 were ignored with respect to the first order K_{ijk} and the dependence on ω was dropped. Solving the system (3.18) for n^2, the following eigenvalues are obtained:

$$\begin{cases} n_+^2 = \varepsilon^0 + i\varepsilon_{xy} \\ n_-^2 = \varepsilon^0 - i\varepsilon_{xy} \end{cases} \tag{3.19}$$

In both (3.18) and (3.19) ε_{xy} refers to the KM_z component of (3.16). Plugging these expressions for n^2 in (3.18), we obtain that $E_y = \pm iE_x$ respectively. This shows that in this geometry (figure 3.1) the modes of light propagation in a magnetized medium are eigenstates of right- and left-circularly polarized light. Their complex refractive indexes are given by $n_\pm$, so these components propagate inside the medium with different phase velocities and attenuation. This gives rise to the Faraday effect, both rotation (given by the resulting phase difference) and ellipticity (given

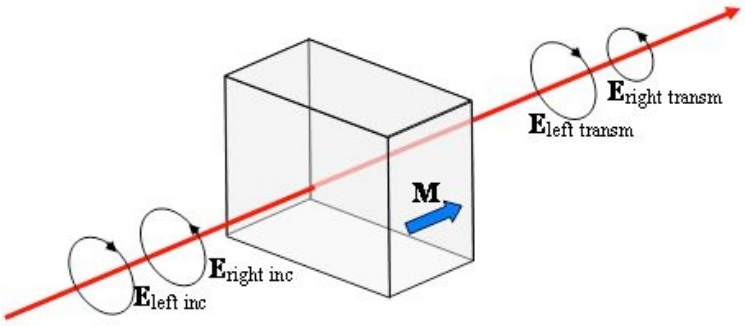

Figure 3.1: The Faraday geometry, with the light propagation vector parallel to the magnetization.

by the resulting absorption difference). The origin of the Kerr effect may be understood within the same formalism.

In order to establish the equation for the Faraday rotation and ellipticity (dichroism) we consider an incoming light beam with linear polarization along the x axis. It can be decomposed into the sum of a left- and a right-circularly polarized component (3.4):

$$\begin{pmatrix} 1 \\ 0 \end{pmatrix} = \frac{1}{2}\left[\begin{pmatrix} 1 \\ i \end{pmatrix} + \begin{pmatrix} 1 \\ -i \end{pmatrix}\right] \tag{3.20}$$

These two components propagate through the medium with different wavevectors $k_{\pm} = n_{\pm}k_0$, and after a path d is crossed, the total field will be:

$$\begin{aligned}
\begin{pmatrix} E_x \\ E_y \end{pmatrix} &= \frac{E_0}{2}\left[\left[e^{i[k_0(n'_+ + in''_+)d - \omega t]}\begin{pmatrix} 1 \\ i \end{pmatrix}\right] + \left[e^{i[k_0(n'_- + in''_-)d - \omega t]}\begin{pmatrix} 1 \\ -i \end{pmatrix}\right]\right] = \\
&= \frac{E_0}{2}\begin{pmatrix} e^{i[k_0(n'_+ + in''_+)d - \omega t]} + e^{i[k_0(n'_- + in''_-)d - \omega t]} \\ ie^{i[k_0(n'_+ + in''_+)d - \omega t]} - ie^{i[k_0(n'_- + in''_-)d - \omega t]} \end{pmatrix} = \\
&= \frac{E_0}{2}e^{i\left[\frac{k_0(n'_+ + n'_-)d}{2} - \omega t\right]}\begin{pmatrix} e^{-k_0 n''_+ d - i[\frac{k_0(n'_- - n'_+)d}{2}]} + e^{-k_0 n''_- d + i[\frac{k_0(n'_- - n'_+)d}{2}]} \\ ie^{-k_0 n''_+ d - i[\frac{k_0(n'_- - n'_+)d}{2}]} - ie^{-k_0 n''_- d + i[\frac{k_0(n'_- - n'_+)d}{2}]} \end{pmatrix}
\end{aligned} \tag{3.21}$$

Defining $\theta = \frac{k_0(n'_- - n'_+)d}{2}$ and $\beta_{\pm} = k_0 n''_{\pm} d$, 3.21 may be written as:

$$\begin{pmatrix} E_x \\ E_y \end{pmatrix} \propto \begin{pmatrix} e^{-\beta_+}(\cos\theta - i\sin\theta) + e^{-\beta_-}(\cos\theta + i\sin\theta) \\ ie^{-\beta_+}(\cos\theta - i\sin\theta) - ie^{-\beta_-}(\cos\theta + i\sin\theta) \end{pmatrix} = \begin{pmatrix} \cos\theta - i\tanh\psi\sin\theta \\ \sin\theta + i\tanh\psi\cos\theta \end{pmatrix} = \begin{pmatrix} \cos\theta - \sin\theta \\ \sin\theta + \cos\theta \end{pmatrix} \begin{pmatrix} 1 \\ i\tanh\psi \end{pmatrix} \tag{3.22}$$

with $\psi = \frac{\beta_- - \beta_+}{2} = \frac{k_0(n''_- - n''_+)d}{2}$. The vector in 3.22 describes an elliptically polarized wave with ellipticity equal to $\tanh\psi$ and principal axis rotated by θ with respect to the original polarization (see 3.6). The Faraday rotation θ_F may then be defined as the rotation after a unit path:

$$\theta_F = \frac{\theta}{d} = \frac{k_0}{2}(n'_- - n'_+) = \frac{k_0}{2}Re[n_- - n_+] = \frac{k_0}{2}Re[\frac{-2i\varepsilon_{xy}}{\sqrt{\varepsilon^0 - i\varepsilon_{xy}} + \sqrt{\varepsilon^0 + i\varepsilon_{xy}}}], \tag{3.23}$$

where the last relation was obtained using equation (3.19). In the limit of small off-diagonal elements $|\varepsilon_{xy}| \ll |\varepsilon^0|$ in 3.16 and weakly absorbing material ($n'' \ll n'$), θ_F may be written as:

$$\theta_F = \frac{k_0}{2}Re[\frac{-2i\varepsilon_{xy}}{2\sqrt{\varepsilon^0}}] \approx -\frac{k_0\varepsilon''_{xy}}{2\overline{n}'} \approx -\frac{k_0}{2\overline{n}'}K''M, \tag{3.24}$$

where $\sqrt{\varepsilon^0} \approx \overline{n}' + i\overline{n}''$ in this approximation and K'' is the imaginary part of the ε_{xy} component of (3.16) ($K = K' + iK''$). It is clear from (3.24) and (3.16) that θ_F depends on the magnetization of the medium. The proportionality constant between the magnetization and the Faraday rotation is known as the Verdet constant. In the same fashion, the Faraday ellipticity may be defined:

$$\psi_F = \frac{1}{d}\tanh[\frac{k_0}{2}(n''_- - n''_+)d] \approx \frac{k_0}{2\overline{n}'}K'M \tag{3.25}$$

Both the Faraday rotation and the ellipticity are thickness dependent quantities, so that increasing the sample's thickness it is possible to obtain larger signals when working in transmission geometry. The Faraday ellipticity is directly linked to the Magnetic Circular Dichroism (MCD), the physical quantity measured in most of our experiments, in order to indirectly determine the magnetization of ensembles of nanoparticles and molecular magnets dispersed in transparent media in which sometimes traditional measurement techniques such as SQUID or VSM will not be sensitive enough. In order to link the ellipticity to the magnetic circular dichroism, we introduce in (3.25) the absorption coefficients for left- and right-circularly polarized light, α_- and α_+, and the circular dichroism $\Delta\alpha = \alpha_- - \alpha_+$. we can write the intensity of the transmitted beam for each polarization state as:

$$I_{\pm} = I_0 e^{-2k_0 n''_{\pm} d} = I_0 e^{-\alpha_{\pm} d} \tag{3.26}$$

From both (3.25) and (3.26) we get:

$$\psi_F = \frac{1}{d}\tanh(\frac{\Delta\alpha d}{4}) \tag{3.27}$$

It is thus demonstrated that the magnetization of a transparent magnetized medium is accessible through its magnetic circular dichroism.

A similar approach may be employed when the measurement in performed in reflection, when it is generally known as Kerr effect. In this case we must consider the Fresnel relations ([65],[62],[66]) connecting the reflected and the incident light beams:

$$\frac{E_{refl}}{E_{inc}} = \frac{n-1}{n+1} = r \tag{3.28}$$

where n is a complex quantity. The eigenmodes in this geometry are the same as in the Faraday geometry we have just discussed, but with the following eigenvalues:

$$r_+ = \frac{(n_+)-1}{(n_+)+1} \text{ and } r_- = \frac{(n_-)-1}{(n_-)+1} \tag{3.29}$$

Using the Jones formalism and considering an incident plane-polarized wave (polarization parallel to x), the reflected wave is:

$$E_{refl} = E_{inc}\left[\frac{r_+}{2}\begin{pmatrix}1\\ i\end{pmatrix} + \frac{r_-}{2}\begin{pmatrix}1\\ -i\end{pmatrix}\right] = \frac{E_{inc}}{2}\begin{pmatrix}r_+ + r_-\\ i(r_+ - r_-)\end{pmatrix} \tag{3.30}$$

This represents an elliptically polarized reflected wave. Defining $r_{\pm} = e^{R_{\pm}+i\phi_{\pm}}$, $\Delta\phi = \frac{\phi_- - \phi_+}{2}$ and $\Delta R = \frac{r_- - r_+}{2}$ we can write 3.30 as:

$$\begin{aligned}\begin{pmatrix}r_+ + r_-\\ i(r_+ - r_-)\end{pmatrix} &= \begin{pmatrix}\cos\Delta\phi - (-i\tanh\Delta R)\sin\phi\\ \sin\Delta\phi + (-i\tanh\Delta R)\cos\phi\end{pmatrix} = \\ &= \begin{pmatrix}\cos\Delta\phi - \sin\Delta\phi\\ \sin\Delta\phi + \cos\Delta\phi\end{pmatrix}\begin{pmatrix}1\\ -i\tanh\Delta R\end{pmatrix}\end{aligned} \tag{3.31}$$

The Kerr rotation θ_K is given by $\Delta\phi$ and the Kerr ellipticity ψ_K is $-\tanh\Delta R$. These quantities may be approximated (using the same conditions we used to derive (3.24) and (3.25)) by:

$$\begin{aligned}\theta_K &= -Im[\frac{n_+ - n_-}{n_+ n_- - 1}] \approx -\frac{-K^{'}}{(\varepsilon^0 - 1)\sqrt{\varepsilon^0}} M \\ \psi_K &= -Re[\frac{n_+ - n_-}{n_+ n_- - 1}] \approx \frac{K^{''}}{(\varepsilon^0 - 1)\sqrt{\varepsilon^0}} M\end{aligned} \tag{3.32}$$

where (3.16) and (3.19) were also employed. It is again evident that the resultant rotation and ellipticity are proportional to the applied magnetic field. But comparing (3.32), (3.24) and (3.25) we see that the dependence with the off-diagonal components of the dielectric tensor (3.16) is interchanged. Furthermore, the Kerr effect does not depend on the quantity of material investigated, as long as its thickness is much larger than the wavelength used (for small thicknesses the rotation and ellipticity have slightly different expressions, and the technique is known as SMOKE, see [25]). As a consequence the Faraday effect will be larger than the Kerr effect by a factor equal to the ratio between the sample thickness and the wavelength of the light used in the measurement.

It must also be pointed out that in reflection there are 3 possible measurement geometries (depicted in figure 3.2), that depend on the relative orientation of the magnetization vector with respect to the sample's surface and the plane of incidence. In the polar geometry, the magnetization is perpendicular to the sample's surface; in the longitudinal Kerr effect, the magnetization lies on the sample plane and is parallel to the plane of incidence; in the transverse geometry, the magnetization is on the plane, but perpendicular to the plane of incidence (in this geometry the quantity measured is known as reflectivity). The equations derived above are valid for the polar geometry, which is the most convenient way of measuring the Kerr effect with our experimental setup (see section 4.1.3, chapter 4). The generalization of (3.32) for any incidence angle is obtained by solving (3.11) for the particular geometry and imposing the appropriate boundary conditions at the surface. This way a generalized reflection matrix (the magneto-optical Fresnel matrix), is obtained:

$$\begin{pmatrix} E_p^r \\ E_s^r \end{pmatrix} = \mathbf{R} \begin{pmatrix} E_p^i \\ E_s^i \end{pmatrix} = \begin{pmatrix} r_{pp} & r_{ps} \\ r_{sp} & r_{ss} \end{pmatrix} \begin{pmatrix} E_p^i \\ E_s^i \end{pmatrix} \tag{3.33}$$

where E^iandE^r are the incident and the reflected fields, respectively. The element r_{ij} is equal to the ratio between the incident j polarized field and the reflected i polarized field, where i and j denote the p and s polarization states. p means the polarization is parallel to the plane of incidence, and s means polarization perpendicular to this plane. The diagonal elements r_{pp} and

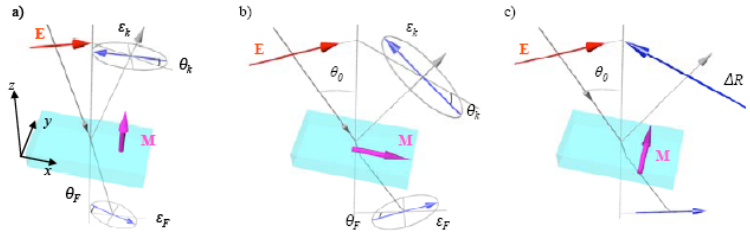

Figure 3.2: The three possible Kerr geometries: **a)** Polar geometry; **b)** longitudinal geometry; and **c)** transverse geometry; θ_k denotes the Kerr rotation angle, ε_k the ellipticity, θ_F is the Faraday rotation angle and ε_F is the Faraday ellipticity.

r_{ss} are the usual Fresnel coefficients for p and s polarized waves, respectively [66], while the off-diagonal elements r_{ps} and r_{sp} will give rise to the magneto-optical Kerr effect [61].

Explicit expressions for the coefficients r_{ij} were calculated for a cubic crystal magnetized along the z axis, with xz being the plane of incidence, in reference [61]. These coefficients are:

$$\begin{aligned} r_{pp} &= \frac{n_0\cos(\theta_i)-\cos(\theta_r)}{n_0\cos(\theta_i)+\cos(\theta_r)}, \; ; r_{ss} = \frac{\cos(\theta_i)-n_0\cos(\theta_r)}{\cos(\theta_i)+n_0\cos(\theta_r)} \\ r_{ps} &= r_{sp} = \frac{KM}{n_0(\cos(\theta_i)+n_0\cos(\theta_r))(n_0\cos(\theta_i)+\cos(\theta_r))} \end{aligned} \tag{3.34}$$

with θ_i being the angle of incidence and θ_r the angle of refraction defined by $\sin(\theta_r) = \frac{1}{n_0}\sin(\theta_i)$.

The application of these expressions to real magneto-optical measurements will be presented in chapter 4. The next section will be dedicated to a quantum mechanical approach to magnetic circular dichroism.

3.3 Magnetic Circular Dichroism - a quantum mechanical approach

In the previous section magneto-optical phenomena were given a phenomenological treatment based on the macroscopic dielectric tensor. While this is sufficient to explain the observed variations in polarization of the transmitted light beam (in this section only the Faraday geometry will be taken into consideration), a quantum treatment is necessary in order to explain the spectroscopic character of MCD measurements, beyond the simple relations introduced by (3.26) and (3.27). In fact, it is an important experimental technique for the study of the geometric and electronic structure of transition metal complexes ([67],[55]), metalloproteins ([55],[54]), diluted

magnetic semiconductors ([57]) and also complexes with exchange coupled radicals ([56]). We must add that its usage could also be extended to magnetic nanoparticles ([48]) and thin-film systems ([68]), something that is already in the X-ray range (XMCD) but is still not very widespread in the UV-visible-NIR range. It is evident that in this last case the instrumentation is much simpler, and the measurements can be performed in a small scale laboratory (in opposition to a large-scale synchrotron facility, necessary for XMCD measurements). The application of this technique to the investigation of magnetic properties of single-molecule magnets is also not very widespread, being it mostly used as a probe of magnetization as explained in the previous section, and shown in [2], [69], [70], [71], [30], [48] and [72].

The MCD spectrum, contrary to the absorption spectrum, is a signed quantity and thus provides much higher resolution than absorption spectroscopy (UV-vis), particularly in regions of overlapping absorption bands; it permits the investigation of even-electron non-Kramers systems that are frequently difficult to study with EPR. It simultaneously provides information about the ground and excited states of the system under study, and is therefore a link between EPR, which primarily probes the electronic ground state, and absorption or resonance Raman spectroscopy, which primarily probe electronically excited states. And MCD provides orientational selectivity even for frozen solution or disordered ensembles of molecules. Due to the sensitivity of the MCD intensity to the transition polarizations, only a subset of randomly oriented molecules will contribute to a given MCD signal. The theory of MCD spectroscopy was pioneered by Stephens (see [73],[74]) and very well summarized by Piepho and Schatz in [75]. Mason ([76]) presents it in a more compact fashion, and, together with Solomon and Neese ([67]), will be the basis to the following presentation of the theory.

As introduced in the previous section, MCD is based upon the measurement of the difference in absorption between left- and right-circularly polarized light induced in a sample by a strong magnetic field oriented parallel to the direction of light propagation. The difference in absorption is given by $\Delta\alpha = \alpha_- - \alpha_+$ introduced in 3.26 and 3.27 [2]. MCD results from the combined effect of the lower symmetry induced in the material by a non-zero magnetization and the spin-orbit coupling. It is an universal property of light absorption for all matter placed in a magnetic field, and as such is analogous to conventional light absorption, obeying the Beer-Lambert law $I(d) = I_0 e^{-\kappa d}$ where κ is the absorption coefficient (dependent on the molar concentration of the absorbing species) and d, the length of the path through the absorbing medium. Furthermore, the magnetically induced $\Delta\alpha$ is proportional to the applied magnetic field $\Delta\alpha \propto \Delta\varepsilon_M c d \mathbf{B}$ (c is

[2] The measured $\Delta\alpha$ is the same quantity measured for natural circular dichroism (CD) which is observed for chiral molecules. The origin of both effects is, however, quite different.

the molar concentration of absorbers and $\Delta\varepsilon_M$ is the differential molar absorptivity per unit of applied field).

In the domain where the MCD function is a linear function of the applied magnetic field, the signal for an ensemble of randomly oriented molecules is given by:

$$\begin{aligned}\frac{\Delta\varepsilon}{E} &= \frac{\varepsilon_- - \varepsilon_+}{E} = \frac{1}{dc}\frac{\alpha_- - \alpha_+}{E} = \\ &= \gamma\mu_B B\left[\left(-\frac{\partial f(E)}{\partial E}\right)\overline{A}_1 + \left(\overline{B}_0 + \frac{\overline{C}_0}{kT}\right)f(E)\right]\end{aligned} \tag{3.35}$$

where γ is a collection of constants [67], μ_B is the Bohr magneton, k is the Boltzmann constant, T is the temperature, B is the magnetic flux density, $f(E)$ is a line shape function, d is the path length through the medium, c is the concentration of absorbers and $E = \hbar\omega$ is the energy of the incident radiation. $\overline{A}_1$, $\overline{B}_0$ and $\overline{C}_0$ are called "MCD-terms"and are characteristic numbers that depend on the electronic and geometric structure of the molecule under investigation. $\overline{C}_0$ is present only in paramagnetic molecules, while $\overline{A}_1$ and $\overline{B}_0$ also exist in molecules with a spin-singlet ground state ($\overline{A}_1$ is present only in case the molecule has orbital degeneracy). For paramagnetic transition metal complexes at very low temperatures the temperature-dependent $\overline{C}_0$ term (henceforth called the C-term) dominates the spectrum. In this regime it is no longer linear with respect to B, with saturation being reached for high B/T ratios. Further in this section a method to calculate MCD in function of magnetic field and temperature, based on the calculation of the C-term, will be introduced, but I feel that a small qualitative explanation of each term is necessary. From (3.35) we can see that the A-term ($\overline{A}_1$) describes a derivative-shaped band that is present in the spectrum only in case the system's electronic energy levels have degeneracies that can be lifted by the Zeeman effect. The B-term arises as a result of field-induced mixing of the zero-field wavefunctions. Finally, the C-term is the result of electronic transitions within a degenerate ground state whose levels are differently populated upon the application of a magnetic field. More details can be found in [76].

The calculation of the terms starts from the Fermi Golden Rule, assuming a pure electric dipole mechanism for the transitions from an initial quantum state $|a\rangle$ with Boltzmann population N_a to a final quantum state $|j\rangle$ with Boltzmann population N_j. The Franck-Condon and the Born-Oppenheimer are used, and $\Delta\varepsilon/E$ is given by:

$$\frac{\Delta\varepsilon}{E} = K\sum_{aj}(N_a - N_j)[|\langle a|m_-|j\rangle|^2 - |\langle a|m_+|j\rangle|^2]f(E) \tag{3.36}$$

where m_- and m_+ are the transition dipole moment operators for left- and right- circularly polarized in a laboratory fixed reference coordinate system, and $f(E)$ is the band-shape function, assumed to be independent of applied magnetic field (the rigid-shift approximation). The initial N_j population is assumed to be zero. It is interesting to point out that in order to obtain the expression for light absorption the minus sign between the transition matrix elements in (3.36) must be changed by a plus sign. The calculation proceeds by expressing (3.36) in a molecule fixed coordinate system and then averaging over all molecular orientations. An orthonormal set of many electron wavefunctions $|\alpha S_\alpha M\rangle_0$ is assumed to diagonalize the Born-Oppenheimer Hamiltonian, where α contains all the necessary quantum numbers except S_α, and M is the projection of the spin state S_α on the z-axis. Spin-orbit coupling is included as a first-order perturbation, using the one-electron approximation of the SO operator:

$$H_{SO} = \sum_{Nj} \xi(r_{iN}) \vec{l}_N(i) \vec{s}(i) = \sum_{m=0,\pm 1} (-1)^m \sum_i h_{-m}(i) s_m(i) \tag{3.37}$$

where $\vec{l}_N(i)$ is the orbital momentum of the ith electron relative to the nucleus N, $\vec{s}(i)$ is the spin angular momentum operator for electron i and $h_{-m}(i)$ is a standard component of the reduced spin-orbit vector operator; and the electric dipole operator (in atomic units)

$$\vec{m} = \sum_N Z_N \vec{R}_N - \sum_i \vec{r}_i \tag{3.38}$$

is used in order to evaluate the transition moments.between the perturbed states (Z_N is the charge of the Nth nucleus, $\vec{R}_N$ its position and $\vec{r}_i$ the position vector of the ith electron). The effect of an applied magnetic field is assumed to (a) induce a mixing between the M-components of the initial states $|ASM\rangle$ and of the final states $|JSM\rangle$; (b) change the relative energies (and so the relative Boltzmann populations N_a) of the ground state sublevels. The A-term contribution (arising from transitions between Zeeman split sublevels) is neglected and only mixing between initial state components is considered (so out of state B-terms are neglected). Furthermore, we neglect the excited state ZFS, so that all $|JSM_i\rangle$ are effectively degenerate. Considering all these approximations, as well as the spin-orbit interaction and the appropriate transformation from molecular to laboratory reference frame, (3.36) becomes:

$$\frac{\Delta E}{E} = -\gamma \sum_i \frac{e^{-E_i^{(A)}/kT}}{Z} \left(\sum_{uvw} t_{uvw} l_u \sum_{M,M'} \Im\{ U_{Mi}^* U_{M'i} \sum_{M'} \langle ASM|m_v|JSM''\rangle \langle JSM''|m_w|ASM'\rangle \} \right) \tag{3.39}$$

where **U** is a complex unitary matrix that describes the transformation from the states $|ASM\rangle$ to the magnetic field dependent states, $\gamma = 4K$, $t_{uvw} = 1$ for $uvw = xyz, zxy, yzx$ and 0 otherwise and $l_u, u = x, y, z$ is given by $\vec{l} = (\sin\theta\sin\phi, \sin\theta\cos\phi, \cos\theta)$. The coefficients **U** can be obtained from the diagonalization of an appropriate spin Hamiltonian. Introducing in (3.39) the perturbative expansions for the matrix elements $\langle ASM|\vec{m}|JSM''\rangle$, some algebra yields three terms that contribute to the MCD, each one depending on the spin-orbit coupling between different sets of levels:

$$\begin{aligned}
\frac{\Delta\varepsilon^{(1)}}{E} &= \frac{\gamma}{S}\vec{l}(\vec{D}^{AJ}\times\Delta\vec{D}^{JA})\Delta_{JA}^{-1}\sum_i \frac{e^{-E_i^{(A)}/kT}}{Z}(\overline{L}_{AJ}^x\langle S_x\rangle_i + \overline{L}_{AJ}^y\langle S_y\rangle_i + \overline{L}_{AJ}^z\langle S_z\rangle_i) \\
\frac{\Delta\varepsilon^{(2)}}{E} &= \frac{\gamma}{S}\sum_{K\neq A,J}\vec{l}(\vec{D}^{KA}\times\vec{D}^{AJ})\Delta_{KJ}^{-1}\sum_i \frac{e^{-E_i^{(A)}/kT}}{Z}(\overline{L}_{KJ}^x\langle S_x\rangle_i + \overline{L}_{KJ}^y\langle S_y\rangle_i + \overline{L}_{KJ}^z\langle S_z\rangle_i) \\
\frac{\Delta\varepsilon^{(3)}}{E} &= \frac{\gamma}{S}\sum_{K\neq A,J}\vec{l}(\vec{D}^{AJ}\times\vec{D}^{JK})\Delta_{KA}^{-1}\sum_i \frac{e^{-E_i^{(A)}/kT}}{Z}(\overline{L}_{KA}^x\langle S_x\rangle_i + \overline{L}_{KA}^y\langle S_y\rangle_i + \overline{L}_{KA}^z\langle S_z\rangle_i)
\end{aligned} \tag{3.40}$$

Equations (3.40) predict the sign and magnitude of an MCD transition between spatially non-degenerate states A and J as a function of temperature, magnetic field and orientation. The temperature dependence arises from the Boltzmann population factors and the orientation dependence arises from $\vec{l}$ and the spin expectation values $\langle\vec{S}\rangle_i$. It is evident that some SO coupling must be present in order for MCD to occur. This coupling will be more efficient the smaller the energy gap between the two states involved and the larger the SOC matrix elements. Orientation-averaged MCD spectra or MCD vs. H curves may be obtained by integrating (3.40) over all magnetic field orientations:

$$MCD_{av}(E) = \frac{1}{4\pi}\int_0^{\pi}\int_0^{2\pi}\frac{\Delta\varepsilon^{(1)} + \Delta\varepsilon^{(2)} + \Delta\varepsilon^{(3)}}{E}\sin\theta d\theta d\phi \tag{3.41}$$

Equations (3.40) may be straightforwardly interpreted if group theoretical arguments are used to calculate the SOC matrix elements. In this work, a computer program that implements the model previously outlined was used in order to obtain transition moments and polarizations from the MCD x H curves of paramagnetic molecules [67]. It is based on the use of the following spin Hamiltonian:

$$\hat{H}_{spin} = \mu_B\vec{B}\mathbf{g}\vec{S} + D[S_z^2 - (\frac{1}{3})S(S+1)] + E[S_x^2 - S_y^2] \tag{3.42}$$

For each magnetic field point and orientation (3.42) is diagonalized, spin expectation values are

calculated from the resulting eigenvectors[3] and the Boltzmann populations are evaluated from the eigenvalues. The experimental curves are analyzed by fitting the effective transition moment products M_{xy}^{eff}, M_{xz}^{eff} and M_{yz}^{eff} and/or the spin Hamiltonian parameters together with a scaling parameter. The fits are done with a Simplex algorithm.

[3] $\langle S_p \rangle_i = \sum_{M,M'} U_{Mi}^* U_{M'i} \langle SM|s_p|SM' \rangle$

4 The experimental techniques

In order to address and measure the magnetic properties of diluted samples of nanoparticles and SMMs, I have mainly employed the MCD/MOKE magnetometer owned by LENS (European Laboratory for Non-Linear Spectroscopy) of the University of Florence, adding to its setup the capability of performing ac susceptibility measurements in a totally optical way. In this chapter I am going to introduce these magneto-optic experimental techniques, giving a brief description of the MCD/MOKE magnetometer, but describing in more details the development of the ac susceptometer. A brief section at the end of the chapter will be dedicated to the traditional experimental techniques used in the magnetic characterization of these materials.

4.1 The MCD/MOKE magnetometer

The magneto-optical measurements presented in this work have been performed using a home-made MCD/MOKE magnetometer that was built by Dr. Lucia Cavigli and Dr. Lapo Bogani [3, 7, 48]. During my thesis period the instrument was upgraded in order to perform magnetic ac susceptibility measurements exclusively by magneto-optical means. This will be the subject of section 4.2.2.

4.1.1 Light sources

Different lasers are employed as light sources, which allows us to cover a wide range of wavelengths (discretely). This is very important, as we have previously demonstrated that the magneto-optical response of a material may be strongly wavelength dependent. We use a stabilized Helium-Neon (He:Ne) laser for measurements at 632.8 nm. This is also our first choice light source, as it is the most stable available and yields the best signal-to-noise ratios.

For wavelengths in the blue-green region of the spectrum we use an Argon ion (Ar:ion) laser rated at 5W. The lines are separated by an external prism, as this laser in currently used as a pump source to other laser systems. This way it is possible to obtain light with 476.5 nm, 488 nm, 496,5 nm and 514 nm wavelength and with powers at the order of 100mW. This is the

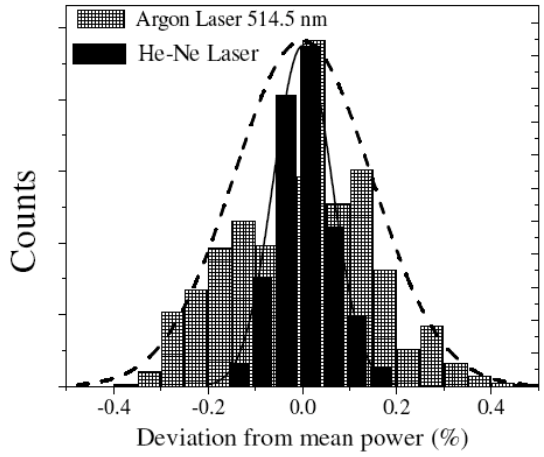

Figure 4.1: Deviation from the mean power, He:Ne and Ar:ion lasers. The acquisition time was of 1 hour. From [3]

noisiest laser system we have employed. A comparison between the stabilities of it and the He:Ne laser may be seen at figure 4.1.

Finally, we have also employed several laser diodes. These worked very well, sometimes with surprisingly large SNR's, similar to those obtained with the He:Ne laser. The diodes are mounted inside a small package that also contains the collimating optics and the electrical connections to the dedicated power supply (and to the temperature controller in one case). The following wavelengths are available: 405 nm, 534 nm, 658 nm, 690 nm, 785 nm and 904 nm. They are very convenient, and were extensively used, for measurements at 405 nm as well as at the Near Infrared (NIR).

4.1.2 Superconducting magnet cryostat

A superconducting magnet cryostat with windows that allow optical access to the sample (Oxford Spectromag® SM4000-11.5), optimized for magneto-optical measurements, is used for mounting the sample holder rod and performing all the experiments. The superconducting magnet is a split coil type, that produces horizontal magnetic fields up to 10 Tesla (11.5 T if the lambda refrigerator is used). Field sweep rates up to 1Tesla/minute are possible. In figure 4.2 the cryostat is shown, together with a detail of its "tail"containing the magnet and the windows. These are made from a synthetic vitreous silica (SPECTROSIL B) that is not birefringent. This

fact, together with the strain-relieved low temperature mounts on which they are glued, assures that they will not affect polarized light. The geometry allows for light propagating both parallel and perpendicularly to the magnetic field direction.

The sample zone is a variable temperature insert (VTI) capable of operating in temperatures between 1.5 and 300 K. The temperature control is achieved by establishing a helium flux between the VTI and the helium bath. This flux is controlled by a needle valve and a pump, and the gas temperature is regulated by an electric heater in thermal contact with the capillary that brings the cold He gas from the bath to the VTI.

The arrangement of the windows allows measurements to be made in both Faraday/MCD (transmitted beam, figure 3.1) and MOKE (reflected beam, figure 3.2) configurations. The possibility to rotate the sample holder rod 360° along the vertical axis allows the user to fine-tune the direction of the reflected beam, when working in Kerr configuration. This creates the possibility of working both with small reflection angles (polar Kerr effect) with the beam entering and exiting the cryostat through the same window, as well as with angles around 45°, when one of the lateral windows must be used to collect the beam. These geometries are limited by the window's acceptance angles, which can be seen in figure 4.3. Performing polar MOKE measurements is quite straightforward, because of the rather large (15°) acceptance angle of the corresponding windows (those along the magnet's bore, and so along the field direction). Longitudinal MOKE, however, is a bit harder, because the MOKE signal approaches 0 for small incidence angles with this geometry. The maximum acceptance angle for the lateral windows (those that must be used with the longitudinal MOKE geometry) is only 7°, small enough to compromise the SNR in this case. The solution is to adopt a "mixed"geometry, in which the sample is positioned at 45° with both the field direction and the incident beam direction. In this case the incidence beam enters through an *fa* window, and exits through one of the *fb* windows (see figure 4.3). These latter geometries were avoided due to problems with vibrations and small displacements of the sample holder rod (especially at high fields), which cause the reflected beam to move out of the detector and so compromises the data acquisition.

The sample holder rod is a long thin-walled tube made of non-magnetic stainless steel. Brass radiation shields shaped like semi-circles are positioned along the rod in order to minimize heat entering the sample space. At the end of this rod, there is a copper cylinder containing a heater, a temperature sensor, and a calibrated Hall probe. At the end of this assembly, there is also a "u-shaped" brass structure, onto which the thin teflon slab employed as sample holder is screwed. These slabs are perforated and generally have 7 holes (with about 4 – 5 mm diameter each) in order to hold up to 7 samples. The sample holder rod's extremity, with the teflon sample holder

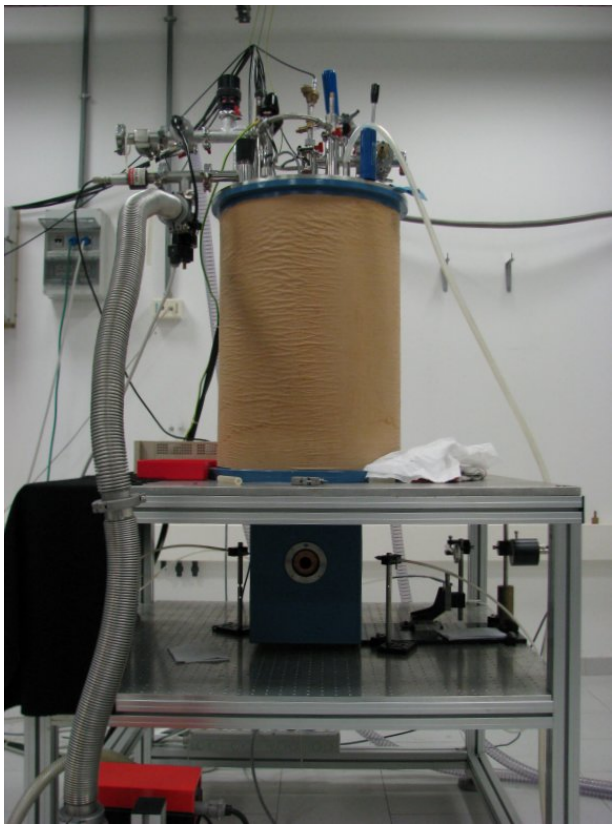

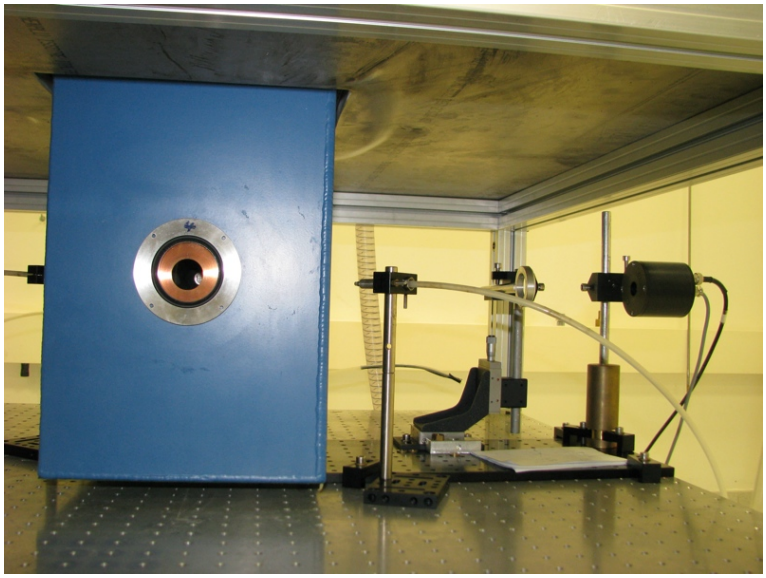

Figure 4.2: The superconducting magnet cryostat (in the upper picture) and a detail of its "tail" with the optical windows and the photodiode detector at the left side.

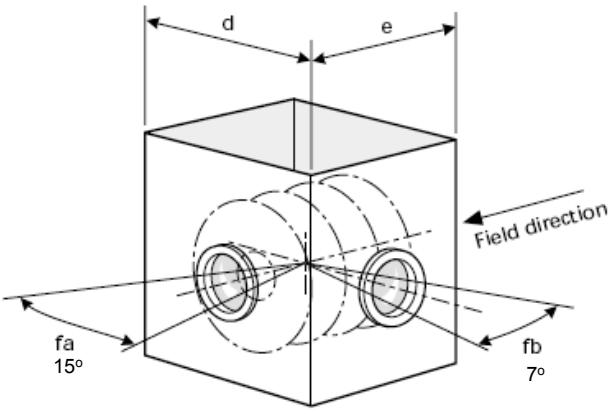

Figure 4.3: The acceptance angles of the cryostat windows.

and the copper cylinder may be seen in figure 4.4.

The Hall probe is used in order to precisely determine the magnetic field intensity in the sample space during MOKE/MCD versus applied field measurements (sensitivity $> 10\mathrm{mV/T}$ with a bias current of 100 mA). It is important to use the Hall probe to measure the magnetic field because the value provided by the power supply (nominal field) does not, in general, correspond to the value measured by the Hall probe. This effect is particularly strong below 0.8 T, where the deviation is greater than 1% and gets larger for fields near zero. This may be the effect of the magnet's remanent field. Another problem is the vertical separation between the sample and the Hall probe. Distances of the order of the window diameter (2cm) showed a deviation within 2% of the central value, but it is not always possible to keep the separation between sample and Hall probe within this limit. The procedure adopted in general is to measure the magnetic field intensity at the sample position by the Hall voltage, rescaled with the nominal value (from the power supply) for fields greater than 1 Tesla. The estimated error of these magnetic field measurements is lower than 0.5%.

4.1.3 Measurement techniques

In both MOKE and MCD setups, in order to maximize the SNR and increase the system's sensitivity, a polarization modulation technique associated to synchronous detection (lock-in amplifier) was employed [77]. The polarization modulator is a photoelastic modulator (PEM)

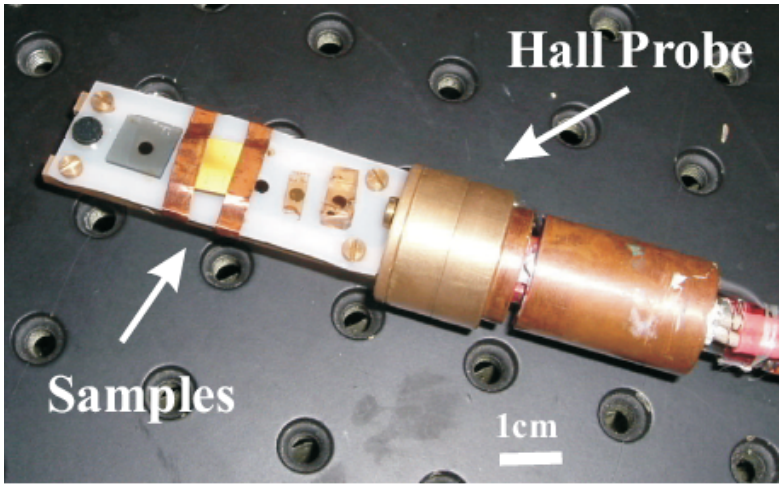

Figure 4.4: The sample holder, with 5 mounted samples. Notice how the golden colored sample is held in place with two pieces of copper adhesive tape. [3]

model PEM-90 made by Hinds Instruments Inc.

The PEM works as a variable retardation waveplate that modulates the beam's polarization periodically at a frequency of 50 kHz. The degree of polarization change may be controlled, as well as the wavelength of operation. The principle of operation is the photoelastic effect: a mechanically stressed material exhibits birefringence (different propagation velocities for different linear polarization components of a light beam) proportional to the applied stress. Our modulator consists in a rectangular bar of fused silica driven into resonant oscillation by a quartz piezoelectric transducer attached to one end of the bar. Exciting it in this way causes a periodic birefringence to develop at the center of it. This birefringence induces a time-dependent phase shift $\delta = A_0 sin(2\pi ft)$ between the polarization components of the incoming light beam that are parallel and perpendicular to the PEM optical axis. Adjusting the peak retardation magnitude A_0, the operator can then choose different peak polarization states for the resulting beam. For example, in order to obtain an output beam whose polarization state oscillates between right and left-circularly polarized, we must set the PEM for quarter-wave retardation (for a particular wavelength) and the incoming beam must be linearly polarized in a plane at 45° with the optical axis of the PEM. In the same way, an output beam whose polarization oscillates between two perpendicular linear states may be generated, setting the PEM to half-wave retardation (figure

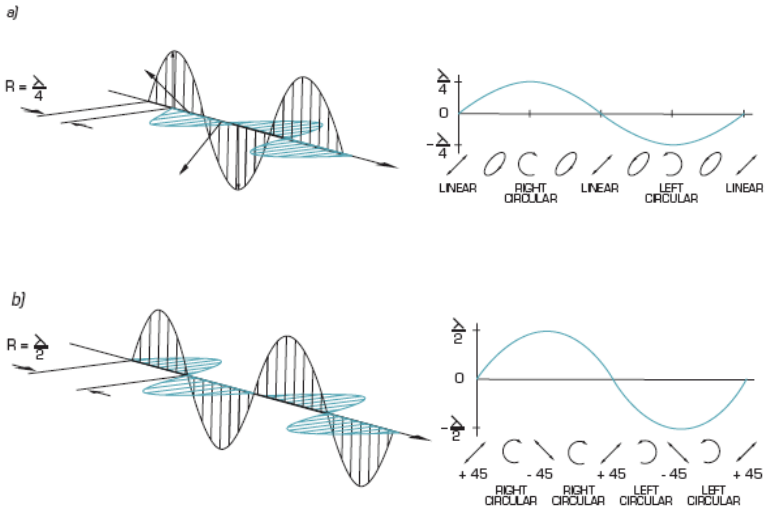

Figure 4.5: PEM operation, with a) quarter-wave retardation, and b) half-wave retardation. (From a Hinds Instruments Inc. brochure)

4.5). The PEM may be used also as a polarization state analyzer.

As light detector we used a pre-amplified silicon photodiode (Hinds Instruments Model DET-100-001) with 5 mm^2 active area, 1 ns rise time, DC - 500kHz frequency response and a spectral range between 350 and 950 nm.

The detector is connected to a signal conditioning unit, that plays a double role. It amplifies the signal, and separates it in two components: a DC component proportional to the average intensity of the transmitted (or reflected) light beam; and an AC component at the same frequency of the polarization modulation. This separation is needed in order to calculate the rotations (Faraday, Kerr) or ellipticities (dichroism) caused by magneto-optical phenomena (see chapter 3). The DC component is measured by a digital multimeter and the AC by a lock-in amplifier (with reference signal provided by the PEM control electronics). All these instruments (including the magnetic field controller and the temperature controller) are connected to a PC through a GPIB bus, and a LabView ® program controls the measurement runs and the data acquisition and storage in an ASCII text file.

In the following subsections I will describe in detail the optical experimental schemes.

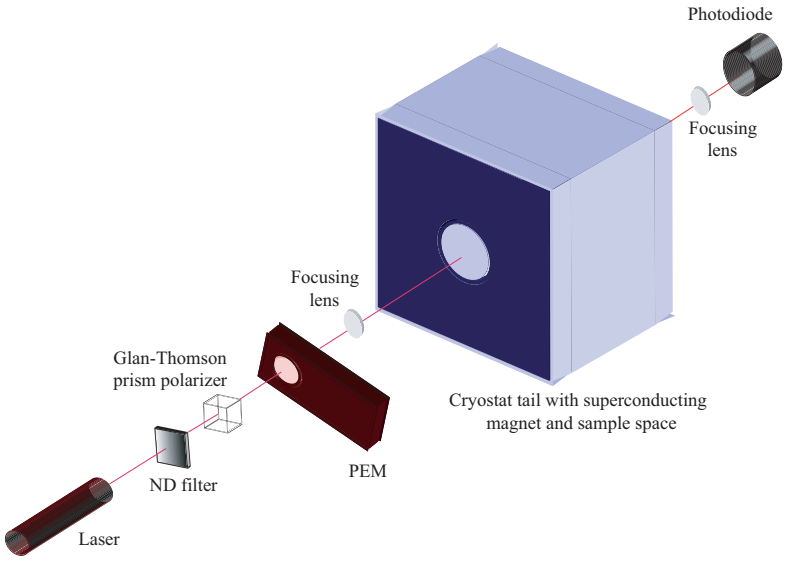

Figure 4.6: The MCD setup.

4.1.4 The MCD setup

The MCD magnetometer setup is used in order to measure the sample's Magnetic Circular Dichroism (MCD) as a function of the applied magnetic field. It consists of a light source (different lasers), the polarization optics (a Glan-Thompson prism polarizer), the photoelastic modulator (PEM), lenses (focusing optics) and the photodiode detector. The schematics are shown in figure 4.6. As we can see, the measurement in this case is carried out in a transmission geometry, that calls for transparent samples, or at least samples that transmit some of the light incident upon it.

As was demonstrated in section 3.2, in materials that produce MCD or Faraday rotation the eigenmodes of light propagation are states with left and right circular polarizations. They propagate in the medium with different refraction indexes denoted by n_+ and n_-, respectively. Assuming these states as a basis (the circular basis, see section 3.1), the Jones matrix that describes the magneto-optical response of this medium is given by (see also [78] and [63]):

$$\mathbf{S} = \begin{pmatrix} e^{i\phi_+} & 0 \\ 0 & e^{i\phi_-} \end{pmatrix} \tag{4.1}$$

where $\phi_\pm = \frac{\omega}{c} d n_\pm$. Always working in this basis, the matrices describing the initial horizontally

polarized beam and the PEM are given by:

$$\mathbf{E_0} = \frac{E_0}{\sqrt{2}} \begin{pmatrix} 1 \\ 1 \end{pmatrix}, \mathbf{M} = \begin{pmatrix} \cos(\frac{\delta}{2}) & -\sin(\frac{\delta}{2}) \\ \sin(\frac{\delta}{2}) & \cos(\frac{\delta}{2}) \end{pmatrix} \tag{4.2}$$

where $\delta = A_0 \sin(2\pi f t) = A_0 \sin(\omega t)$ is the time-dependent retardation induced by the PEM. The transmitted beam, that will be detected by the photodiode, is then given by:

$$\begin{aligned} \mathbf{E_t} &= \begin{pmatrix} E_t^+ \\ E_t^- \end{pmatrix} = \mathbf{SME_0} = \\ &= \frac{E_0}{2\sqrt{2}} \begin{pmatrix} e^{i\phi_+} & 0 \\ 0 & e^{i\phi_-} \end{pmatrix} \begin{pmatrix} \cos(\frac{\delta}{2}) & -\sin(\frac{\delta}{2}) \\ \sin(\frac{\delta}{2}) & \cos(\frac{\delta}{2}) \end{pmatrix} \begin{pmatrix} 1 \\ 1 \end{pmatrix} = \\ &= \frac{E_0}{\sqrt{2}} e^{i\phi_-} \begin{pmatrix} e^{i(R+iD)}[\cos(\frac{\delta}{2}) - \sin(\frac{\delta}{2})] \\ \cos(\frac{\delta}{2}) + \sin(\frac{\delta}{2}) \end{pmatrix} \end{aligned} \tag{4.3}$$

where $R + iD = \phi_+ - \phi_-$ is the difference between the refraction indexes for the two circular polarizations, and the coefficients R and D are related to the Faraday rotation and ellipticity (MCD) (section 3.2):

$$R = 2\theta_F d \, , D = \frac{\Delta\alpha d}{2} \tag{4.4}$$

The intensity of the measured signal, I_T, is proportional to $|\mathbf{E_t}|^2$:

$$I_t \propto I_0 e^{-D}[\cosh(D) + \sinh(D)\sin(\delta)] \tag{4.5}$$

The $\sin(\delta)$ term may be expanded in a Fourier-Bessel series, yielding:

$$\sin(\delta) = \sin(A_0 \sin(\omega t)) = 2\sum_{n=0}^{\infty} J_{2n+1}(A_0)\sin[(2n+1)\omega t] \tag{4.6}$$

Substituting (4.6) in (4.5) and truncating the series at second order, we obtain the following expression for the intensity at the photodiode:

$$I_t \propto I_0 e^{-D}[\cosh(D) + \sinh(D)\big(2J_1(A_0)\sin(\omega t) + 2J_3(A_0)\sin(3\omega t)\big)] \tag{4.7}$$

Taking the $1f$ component (the first harmonic, proportional to $\sin(\omega t)$, synchronously detected by the lock-in amplifier), and normalizing it with respect to the DC component (measured by the digital multimeter, see subsection 4.1.3), we obtain:

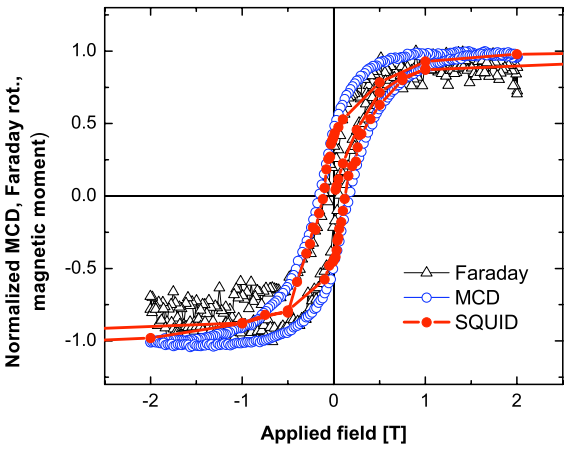

Figure 4.7: Comparison between two measurements performed with the Faraday rotation scheme (black triangles) and the MCD scheme (blue circles). It is evident that the MCD output is cleaner and provides a better curve.

$$\frac{V_{1f}}{V_{DC}} = K_T \tanh(D) 2J_1(A_0) \tag{4.8}$$

where K_T is an instrumental constant independent, in principle, of the light intensity, and A_0 is the PEM peak retardation. Setting it at quarter-wave retardation ($\pi/2$ radians), $2J_1(A_0) = 1.133646$. We can see from (4.8) that the measured first harmonic signal depends only on the circular dichroism D, when this setup (figure 4.6) is used. In case the analyzer is included in the setup, after the sample, and before the photodiode, the expression is slightly different (4.1.5), with the possibility to measure a 2nd harmonic signal that also depends on the Faraday rotation. As this setup was proven to be noisier [3],(see figure 4.7), besides showing other problems related to the proximity between the analyzer and the magnet, it was not employed in this thesis.

In order to obtain absolute values of the dichroism from the measured V_{1f}/V_{DC}, we need to determine the K_T constant. The procedure is straightforward, needing only an extra optical component, the Babinet-Soleil compensator. This is just a continuously adjustable retardation plate, which plays the role of a sample of know birefringence. The setup is the following:

The transmitted intensity for this setup is given by:

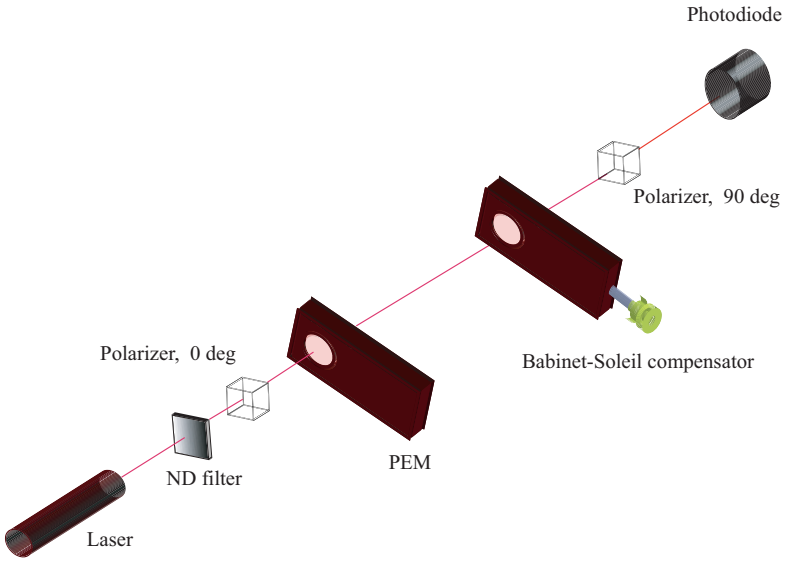

Figure 4.8: The setup used for calculating the K_T constant.

$$I_t \propto |ACME_0|^2 \tag{4.9}$$

where A is the Jones matrix for the analyzer, C represents the Babinet-Soleil compensator, M the PEM and E_0 the incident field. In this case, it is more convenient to work in the linear basis, with the following matrices representing these optical components:

$$\begin{aligned} \mathbf{E_0} &= E_0 \begin{pmatrix} 1 \\ 0 \end{pmatrix}, \mathbf{C} = \begin{pmatrix} \cos(\frac{B}{2}) & i\sin(\frac{B}{2}) \\ i\sin(\frac{B}{2}) & \cos(\frac{B}{2}) \end{pmatrix}, \\ \mathbf{M} &= \begin{pmatrix} \cos(\frac{\delta}{2}) & i\sin(\frac{\delta}{2}) \\ i\sin(\frac{\delta}{2}) & \cos(\frac{\delta}{2}) \end{pmatrix}, \mathbf{A} = \frac{1}{2}\begin{pmatrix} 0 & 0 \\ 0 & 1 \end{pmatrix} \end{aligned} \tag{4.10}$$

Solving equation (4.9) for the matrices in (4.10) we obtain the following expression for the transmitted intensity:

$$I_t \propto [1 - \cos(B)\cos(\delta) + \sin(B)\sin(\delta)] \tag{4.11}$$

which yields the following V_{1f}/V_{DC} upon substitution of $\sin(\delta)$ for the expansion in (4.6) (the $\cos(\delta)$ term depends on the 2nd harmonic):

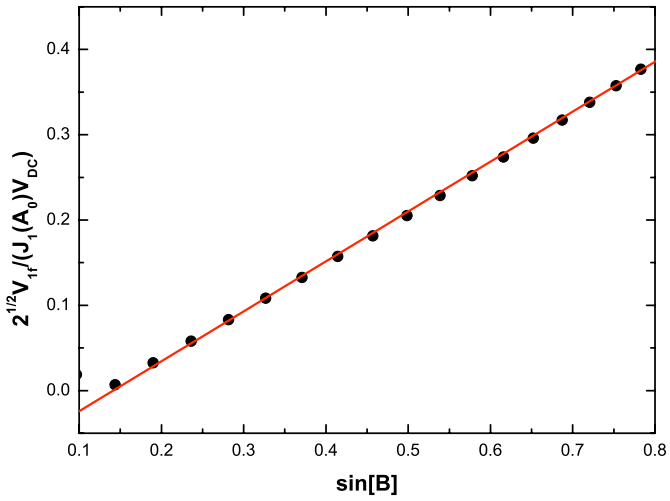

Figure 4.9: The measured peak V_{1f}/V_{DC}, that is equal to the value read by the lock-in multiplied by $\sqrt{2}$, versus the sine of the Babinet-Soleil compensator peak retardation. The angular coefficient yields the K_T constant.

$$\frac{V_{1f}}{V_{DC}} = K_T J_1(A_0)\sin(B) \tag{4.12}$$

The relation between $\sin(B)$ and the measured V_{1f}/V_{DC} is then plotted, and the K_T constant is obtained from the line's angular coefficient. The plot is shown in figure 4.9.

The linear fit yields $K_T = 0.58549 \pm 0.0062$.

With this MCD experimental setup, it is possible to reach a sensitivity of about 50 μrad (50x10^{-6} rad) in a single acquisition. Performing multiple acquisitions for the same sample and averaging the data may increase the sensitivity, but the drift effects associated to the longer measurement run may compromise the final result. The experimenter in this case must carefully consider this trade-off between sensitivity and drift. Up to now, the experimental limit of sensitivity achieved is of the order of 10 μrad.

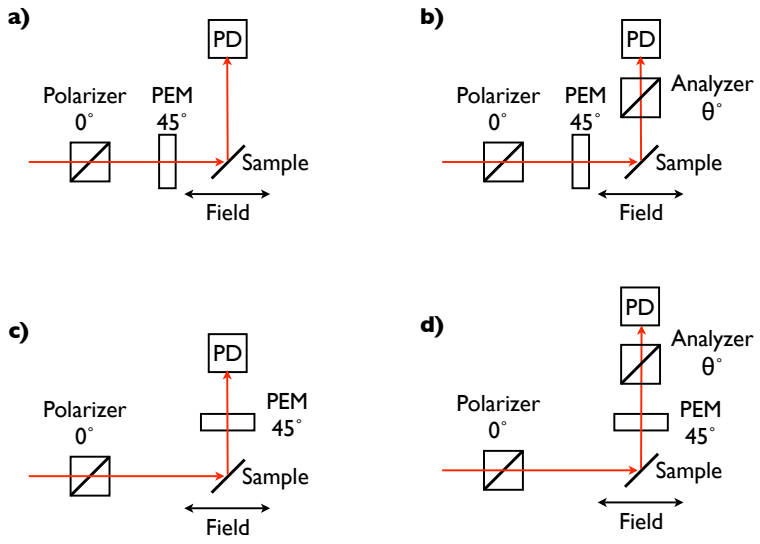

Figure 4.10: 4 possible schemes for MOKE measurements in the .

4.1.5 The MOKE setup

In section 3.2 we showed that when the Magneto-Optical Kerr Effect (MOKE) is measured, there are 3 possible geometries: polar, longitudinal and transverse, each one with its advantages and difficulties. It is the experimenter's job to find the most suitable for the particular needs of a specific measurement.

The possible schemes for the "mixed"longitudinal MOKE geometry are shown in figure 4.10. These geometries were not used in this work, but are included for the sake of completeness.

The setups used to measure the Polar MO Kerr effect in function of applied field, in the same cryostat and using the same optical components, are shown in figure 4.11. The incidence angle in this geometry is limited by the window's acceptance angle to about 7° (see fig. 4.3), (which suits the low incidence angle condition of this MOKE geometry). The reason for the use of geometries **a** and **b** will be discussed later in this subsection.

Always using the Jones formalism, the reflected light intensity is given by:

$$\begin{aligned} I_r &\propto |ARME_0|^2 \\ I_r &\propto |MRE_0|^2 \end{aligned} \tag{4.13}$$

corresponding, respectively, to schemes **a** and **b** in figure 4.10. The Jones matrices, in the linear basis, are:

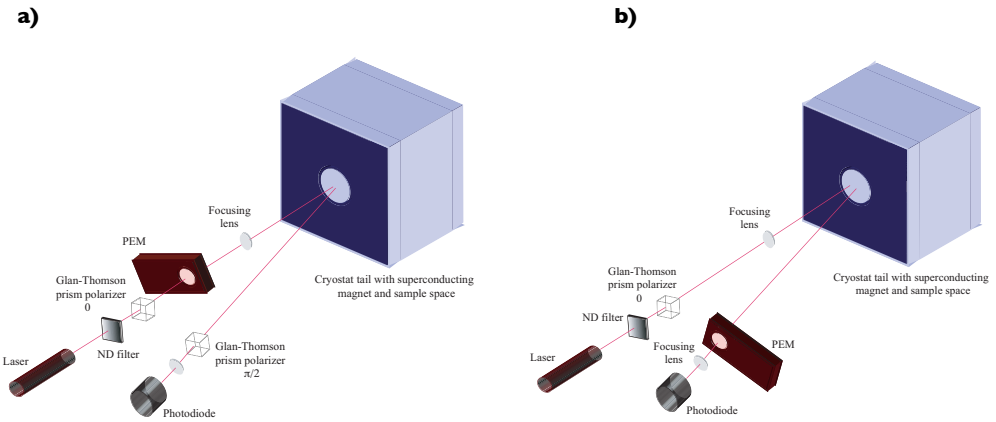

Figure 4.11: The 2 polar MOKE setups.

$$\mathbf{A} = \begin{pmatrix} \cos^2\theta & \cos\theta\sin\theta \\ \cos\theta\sin\theta & \sin^2\theta \end{pmatrix},$$
$$\mathbf{M} = \begin{pmatrix} \cos(\frac{\delta}{2}) & -i\sin(\frac{\delta}{2}) \\ -i\sin(\frac{\delta}{2}) & \cos(\frac{\delta}{2}) \end{pmatrix}, \mathbf{R} = \begin{pmatrix} r_{pp} & r_{ps} \\ r_{sp} & r_{ss} \end{pmatrix} \tag{4.14}$$

During measurement runs in which setup **a** from figure 4.11 was employed, it was seen that the sample holder rod moved during the field sweep (as already mentioned in 4.1.2). The amplitude of the displacement was larger the larger the applied field. For certain samples (the Fe4 and the Mn12 clusters and other molecular magnets, for example) the maximum applied field must be as high as 5 T, causing the reflected spot to move out of the analyzer's entrance cone. Besides, the displacement of the spot over the detector area caused the intensity to fluctuate, compromising the measurement. In order to solve this, we adopted geometry **b** from figure 4.11, in which the PEM is used in place of the analyzer. This substitution was considered because of the high aperture of the PEM. With a high aperture, the beam would not be blocked and the measurement would be possible. That was the case, but the resulting curve was not representative of the sample's magnetic behavior.

For this reason, the MCD measurement scheme (4.1.4) has always been preferred.

4.2 ac susceptibility measurements

In this section the ac susceptibility technique will be presented. In subsection 4.2.1 the "traditional", that is, inductive, ac susceptometry technique will be briefly presented. In subsection 4.2.2 a more detailed description of the magneto-optical ac susceptometer developed during my thesis period will be presented.

4.2.1 The traditional ac susceptometer

The ac susceptibility technique is a very powerful magnetic characterization technique, fundamental in studies of the dynamical behavior of magnetic materials. It allows the determination of anisotropy barriers and relaxation times in a broad range of temperatures and measurement frequencies, making it particularly suited for the characterization of magnetic nanoparticles and single-molecule magnets. As the strength of the magnetic fields used is small, the anisotropy energy barrier is only slightly modified and the magnetization relaxation times may be determined with a very good approximation. Other phenomena may as well be investigated, for example spin-glass behavior, normal-superconducting state transitions, and a variety of critical phenomena [79], [80], [81], [82], [83], [84], [85], [86], [87], [88], [89], [90], [91], [92].

In an ac susceptometer, a small ($\sim 1-5$ Oe) oscillating (AC) magnetic field $H = H_0 + h\cos(\omega t)$, in the general situation in which a DC bias field H_0 is used, is applied on the sample by the primary coils. A set of secondary coils, generally wound as a first-order gradiometer, is used to detect the small changes in the sample magnetization produced by the oscillating field. Without the sample, the secondary should produce no signal, considering the gradiometer coils are wound in a perfectly anti-symmetric way (in opposite directions). If a sample is present inside one of the secondary coils, a signal will be present. Measuring this with a lock-in amplifier, the in-phase and out-of-phase components will give the real and imaginary components of the magnetic susceptibility $\chi = \chi' + i\chi''$. It is important to point out that this technique gives the slope of the sample's magnetization curve, $\chi_{ac} = dM/dH$, in contrast to the DC measurement in which the susceptibility at low fields is derived from the measurement of the magnetic moment m through the relation $\chi_{DC} = m/H$, where H is a small applied field, not necessary in the ac measurement, thus avoiding possible saturation effects in this case. The origin of an out-of-phase component that signals blocking of the magnetization (slow dynamics) and hysteresis may be visualized in figure 4.14. In the upper panel the sinusoidal applied magnetic field is shown. The lower panels show the magnetization as a function of applied field and time. On the left-hand side the behavior above T_B is shown, while on the right-hand side we can see what happens

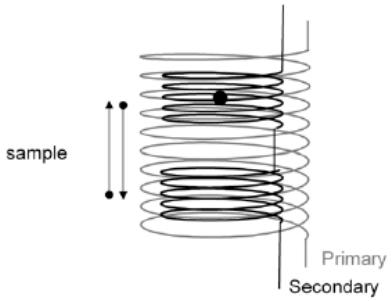

Figure 4.12: The primary and secondary coil configuration of an ac susceptometer. From [4]

when $T \leq T_B$. The points A and C correspond to zero applied field, while B and D to the field extrema. Above T_B, a measurement of the ratio $\frac{M(B)-M(D)}{H(B)-H(D)}$ yields χ', while the 90° out-of-phase measurement will give $\frac{M(C)-M(A)}{H(B)-H(D)} = \chi'' = 0$. Below T_B, blocking effect give rise to hysteresis, and both $M(C)$ and $M(A)$ will not be zero, so $\chi'' \neq 0$ in this case.

The power of this technique resides in the possibility of varying the frequency of the magnetic field in a broad range. If the angular frequency of the applied field, ω, is very low compared to the sample's relaxation time τ ($\omega\tau \ll 1$), the measurement gives the isothermal susceptibility χ_T. In the opposite case, when $\omega\tau \gg 1$, the system does not have time to exchange heat with the external world, and the measured susceptibility is adiabatic, χ_S. Following Casimir and DuPré's work [93], the susceptibility in the intermediate regime is given by:

$$\chi(\omega) = \chi_S + \frac{\chi_T - \chi_S}{1 + i\omega\tau} \tag{4.15}$$

If both χ_S and χ_T are real, the real and imaginary components of the susceptibility, χ' and χ'', are given by:

$$\chi' = \frac{\chi_T - \chi_S}{1 + \omega^2\tau^2} + \chi_S \, , \, \chi'' = \frac{(\chi_T - \chi_S)\omega\tau}{1 + \omega^2\tau^2} \tag{4.16}$$

The frequency dependence of these two quantities is depicted in figure 4.15. The most comprehensive measurement is then a temperature sweep in which the ac susceptibility is measured in a broad range of frequencies (instrument dependent, limited to ~ 0.1 Hz – 1000 Hz in a SQUID-based susceptometer) and temperatures of interest. The analysis of these data may be performed by plotting the characteristic times τ (inverse of the measurement frequency) in function of the temperature at which the maxima of χ'' (at which $\omega\tau = 1$) is observed, taken as the

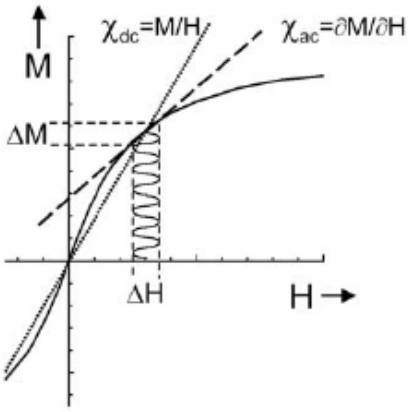

Figure 4.13: The difference between DC and an ac susceptibility measurements. From [4]

blocking temperature for that τ. As was shown in section 2.2, the relaxation times in superparamagnetic materials follow an Arrhenius law, given by $\tau = \tau_0 e^{\frac{\Delta E}{k_B T}}$. From the plot, the values of ΔE, the energy barrier that the spin must overcome in order to relax, and of τ_0, the characteristic relaxation time, may be immediately obtained. Another way of analyzing the susceptibility data is the Argand plot (also know as Cole-Cole plot), obtained by plotting $\chi''(\omega)$ against $\chi'(\omega)$. The expressions 4.16 becomes a semicircle centered on the x axis and with its top satisfying the relation $\omega\tau = 1$. If the relaxation process is characterized by a distribution of relaxation times, the following empirical law [94] is used in place of 4.15:

$$\chi(\omega) = \chi_S + \frac{\chi_T - \chi_S}{1 + (i\omega\tau)^{1-\alpha}} \tag{4.17}$$

with χ' and χ'' given by:

$$\begin{aligned} \chi'(\omega) &= \chi_S + (\chi_T - \chi_S)\frac{1 + (\omega\tau)^{1-\alpha}\sin(\pi\alpha/2)}{1 + 2(\omega\tau)^{1-\alpha}\sin(\pi\alpha/2)}, \\ \chi''(\omega) &= (\chi_T - \chi_S)\frac{\cos(\pi\alpha/2)}{1 + 2(\omega\tau)^{1-\alpha}\sin(\pi\alpha/2)} \end{aligned} \tag{4.18}$$

α is a parameter related to the distribution of relaxation times: the wider the distribution, the larger is α. In this case the Argand plot becomes an arc of circle, with its center displaced into the 4th quadrant, subtended by an angle equal to $\pi(1-\alpha)$.

Our laboratory currently operates 4 of these ac susceptometers: 2 based on commercial SQUID magnetometer systems (see subsection 4.3.1 and two “home-made”systems. These are

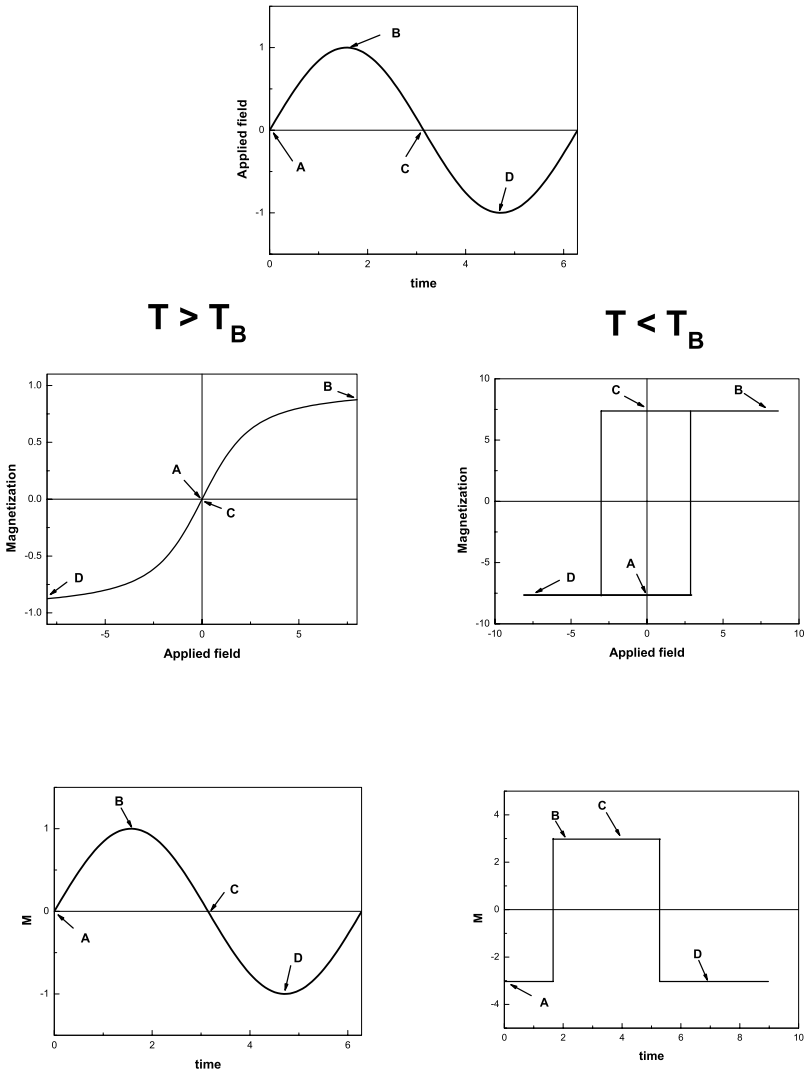

Figure 4.14: The upper graph shows the time dependence of the applied magnetic field. The lower graphs on the left-hand side show the expected magnetization dependence with the applied field, as well as its time-dependence, above the blocking temperature. The graphs on the right-hand side show the response below this temperature, where hysteresis effects give rise to the out-of-phase component of the susceptibility (χ'')

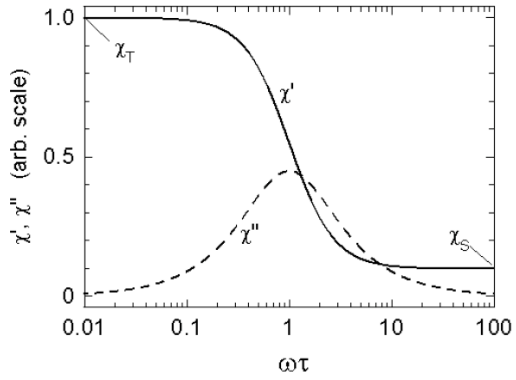

Figure 4.15: The frequency dependence of χ' and χ''. From [4]

capable of operating at frequencies up to 125 kHz, two orders of magnitude higher than the SQUID-based instruments. One of these systems has the further advantage of reaching a minimum temperature of 300 mK employing a ^{3}He refrigerator.

4.2.2 The magneto-optical ac susceptometer

Starting from the basic ideas of a magneto-optical measurements exposed in section 4.1 and of ac susceptibility measurements (subsection 4.2.1), a magneto-optical ac susceptometer was devised [52]. The goal was to reach the sensitivities necessary to measure the susceptibility of highly diluted systems of magnetic molecules and magnetic nanoparticles, ultimately reaching monolayer sensitivity. This last goal has not been reached with the current experimental setup, which is able, though, to determine the susceptibility of small ($\sim$ 3 nm) nanoparticles dispersed in silica, which is to our knowledge the first measurement of this kind performed by magneto-optical means. In fact, magneto-optical ac-susceptometers are not frequently employed, a fact confirmed by the limited bibliography on the subject [95], [96], [97], [98], [99], [100], [101], [102], [103], [104], [105], [106], [107]. Another thing that I would like to highlight is that in all these works an ac/MOKE setup was used to measure the susceptibility of metallic thin films. This puts our instrument in an even more unique position among the available magneto-optical characterization techniques.

The design is much simpler compared to a traditional susceptometer, as the secondary coils are not necessary to detect the susceptibility. This is done magneto-optically. A new sample holder rod was built in order to implement the new measurement technique. The schematics of

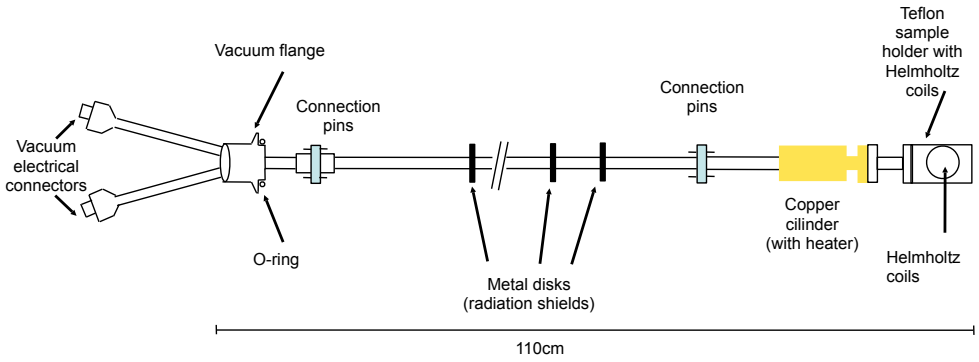

Figure 4.16: The sample holder rod assembled to support the ac susceptibility measurements.

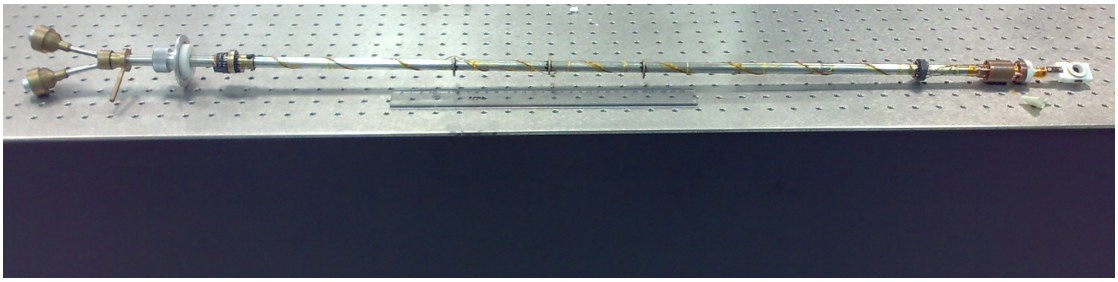

Figure 4.17: A picture of the sample holder rod, ready for insertion into the cryostat.

this rod are shown in figure 4.16, while it may be seen in its final form in figure 4.17.

The rod was made from a thin-walled non-magnetic steel tube, in order to minimize heat transfer to the sample zone. The upper part contains the electric connectors and the vacuum flange necessary to attach it to the upper part of the cryostat variable temperature insert. Metal disks are welded to the intermediate section of the rod in order to minimize heat irradiated from the upper part to the lower, low T section. The lower section contains an electric heater inside a Cu cylinder, and the teflon support to the sample holder and the coils. A calibrated Cernox temperature sensor and a calibrated Hall probe are placed in this teflon support, close to the sample holder. With the Hall probe the real magnetic field on the sample can be measured, and so this rod may also be used for hysteresis measurements.

The excitation coil is a small Helmholtz pair, consisting in two thin coils, wound in the same sense, separated by a distance approximately equal to the coil radius. It has 16 mm of internal

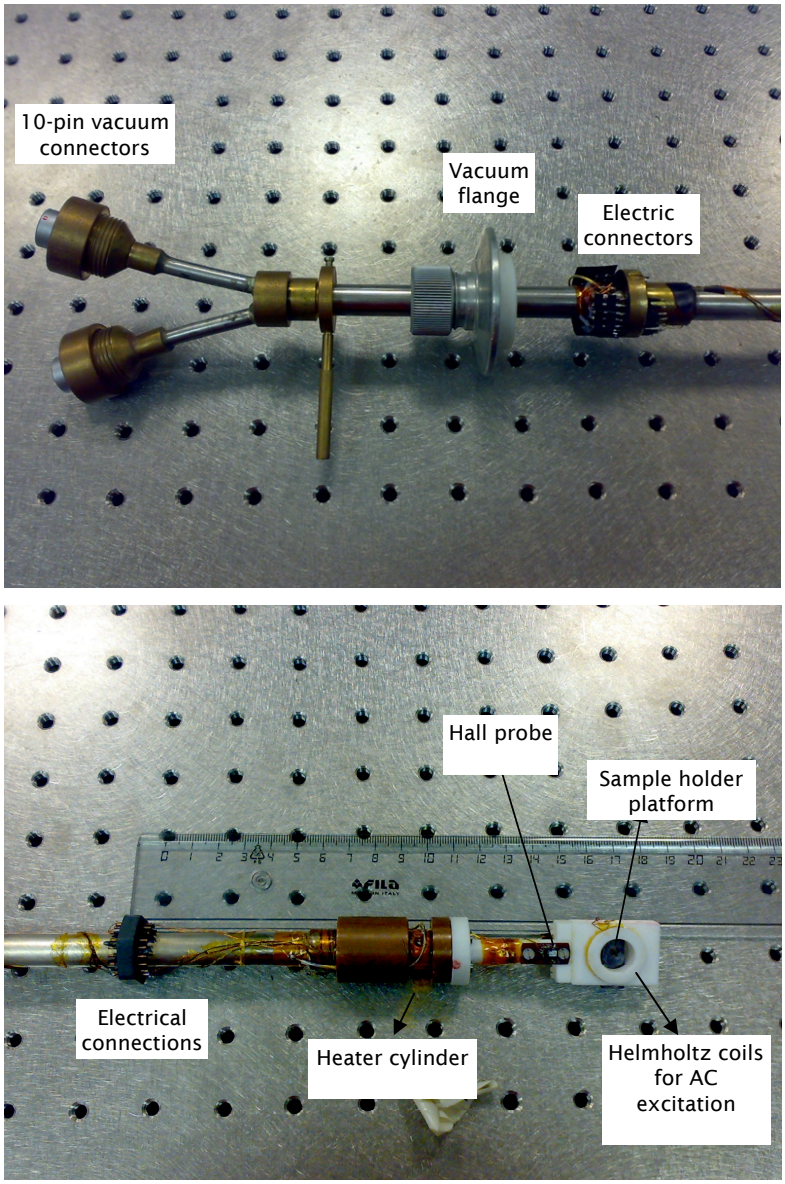

Figure 4.18: Detail of both extremities of the sample holder rod. On the upper picture is its upper part, with two 10 pin vacuum connectors (Fischer connectors model DBEE 1031 A 010 130 and SE 1031 A 010 130 in the cable), and on the lower picture is its lower part, with the teflon piece where the sample holder and the excitation coil are located, the Cu cylinder containing the electrical heater and the Hall probe.

diameter (the bore, where the sample is placed, and an ac magnetic field is generated parallel to the light propagation, as the objective is to measure the ac/MCD) and 18.6 mm of external diameter, corresponding to 4 layers of AWG 32 copper wire (0.2 mm diam.). The distance between the coils is 9.4 mm. The total number of windings is 80 (40 + 40). The Helmholtz geometry was chosen because it produces very homogeneous fields in the geometrical center of the coils, where the sample is placed. The coils were wound in a teflon template, that is attached by means of two teflon screws, to the sample holder rod. Teflon was used because it is non-magnetic and easy to work with. The values of the electrical resistance and the inductance are 2.78 Ω (2.90 Ω considering the thin coaxial that links it to the connector up the sample holder rod) and 0.44 mH (calculated with a finite elements approach [108]). This permits rather high excitation frequencies to be reached without resonance and phase shift problems. A PSpice simulation was used to estimate the resonant frequency during the design of the system. An RLC circuit was used as model, including the parasitic capacitances arising from the coaxial cables and from the windings (estimated in 100 pF and 10 pF, respectively), as well as the resistances of the cables and the coils and the calculated value of the inductance. The resonance frequency measured this way was of the order of 700 kHz, well beyond the necessary operational range (it will be shown further in this chapter that the detection setup limits the upper frequency to about 8 kHz).

The magnetic field produced by the coils was then determined with the aid of a Hall probe Gaussmeter. A magnetic field x current relation equal to 36.55 Gauss/A was obtained from a calibration curve. The typical operational ac fields are in the 3.5 - 4.0 G range.

A function generator is used to power this coil with a sinusoidal excitation of variable amplitude. The same generator provides the reference signal for the lock-in amplifier that determines the ac susceptibility. Recalling the formalism from subsection 4.1.4, the MCD may be measured by a lock-in amplifier synchronized with the PEM frequency. In the ac measurement, however, there is another time-varying polarization modulation due to the ac excitation field. This must also be detected by a lock-in technique, forcing us to employ two of these instruments in the detection scheme, in a configuration know as tandem demodulation [109], [110], [111], [112], [80], [113], [114]. It consists in connecting the photodiode detector output to the first lock-in, and synchronized this with the PEM frequency. If we setup this lock-in with a very short time constant ($\sim$ 50 μs), and if the excitation frequency is much lower than the PEM frequency, its output will display a time dependence that is given by the sample's susceptibility, and that may easily be detected by the second lock-in synchronized to the ac frequency.

This was the only possible way to get a sensible result from this setup. The measurements

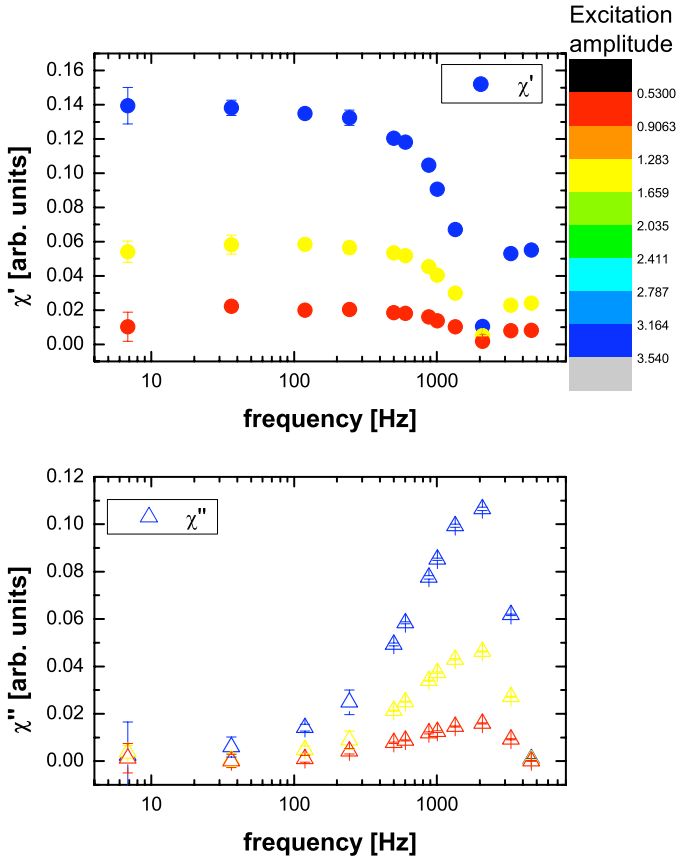

Figure 4.19: The frequency dependence of the ac/MCD signal of the Co nanoparticles at room temperature, for three different amplitudes of the ac field.

without the PEM modulation, with a fixed input beam modulation and only the ac excitation, did not give any results. The drawback is that the first lock-in bandwidth limits the useful ac frequencies to a much lower upper value than the one intended in the beginning of the project. In figure 4.21 the cutoff frequencies (3 dB points) of the first lock-in in the chain are shown for several time constants. We can see that working with $T_C = 50\mu$s implies a cutoff at approximately 6.5 kHz. In fact, data were acquired at frequencies up to 7000 kHz (subsection 5.1.2). A comparison between the normal MCD and the ac/MCD schemes is shown in figure 4.22.

The expressions for the obtained signal may be calculated in the same way shown in subsection 4.1.4, only including a time-dependence in the $\phi_\pm = \frac{\omega}{c} dn_\pm$ parameters of (4.1). This will

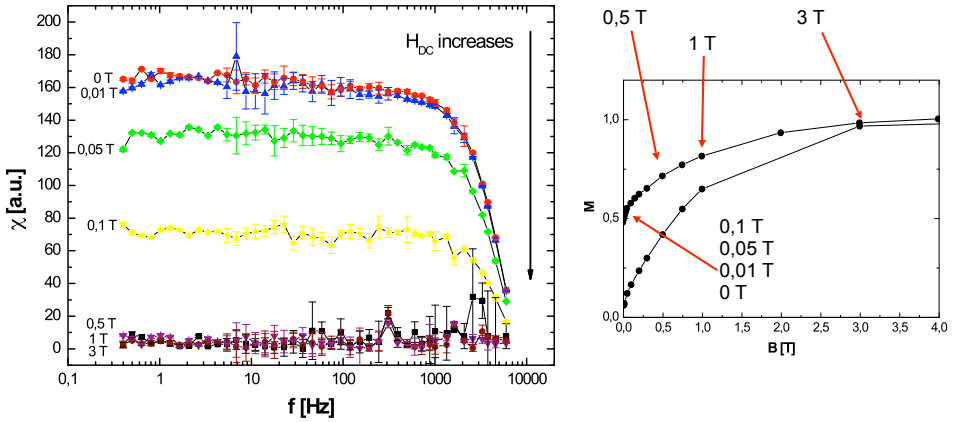

Figure 4.20: The effect of an applied DC bias field on the absolute value of the ac susceptibility. On the right-hand side, the sample's hysteresis curve is shown, and the bias fields are indicated for clarity.

yield an expression like (4.8), with a time-dependent D. This time-dependence arises from the ac excitation, and will generate a signal detected by the second lock-in proportional to the ac susceptibility. In figure 4.19 the first χ' and χ'' x f measurement is shown. It was performed in a sample of Co nanoparticles dispersed in a silica matrix, used due to its strong signal at room temperature. We can see that it reproduces well the expected behavior for the frequency dependence of these parameters (see figure 4.15). In the same figure we can see the variation of the ac susceptibility with the amplitude of the excitation field, for 3 values (4.8, 2.1 and 0.7 Oe[1]). The signal is significantly reduced, as the amplitude of the MCD induced by the excitation field is also reduced. Another test performed in order to check the functionality of the setup was to measure the ac susceptibility of the Co nanoparticles under several values of a static magnetic field. As the ac susceptibility technique measures the slope of the magnetization curve, it is expected that at saturation the signal will be significantly suppressed. This is clearly depicted in figure 4.20, where the suppression of the signal is achieved for static field values greater than 0.5 T.

As a test of the instrument's functionality, the ac-susceptibility curves of a sample of $Co_{33}Ni_{66}$, measured with a SQUID and with the magneto-optical setup, are shown in figure 4.23. The MO measurement was carried out at 405 nm in this case. The first noticeable thing is the large noise

[1] 1 Oe = 0.1 mT

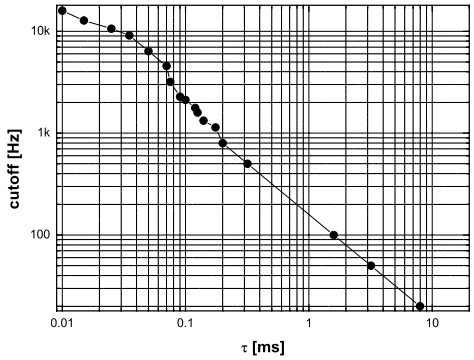

Figure 4.21: Measured cutoff frequencies for several lock-in time constants in the tandem demodulation scheme.

level in the SQUID measurement, compared to the MO one. The analysis of the SQUID data is in this case much harder due to this fact. This is the result of the reduced SNR due to the small concentration of nanoparticles present in the sample. Furthermore, the MO setup gives a much cleaner imaginary part (4.23(b)) of the susceptibility, and the frequency dependence is clearly visible, both in the imaginary (4.23(b)) and the real part (4.23(a)). Looking closely, though, we can see that the maxima of the susceptibility curves are shifted towards higher temperatures in the MO data. In fact, this sample's magnetism depends significantly on the light used to measure it. This phenomenon will be discussed in more details in chapter 5, together with a more detailed account of these measurements.

4.3 Magnetic measurements and other techniques

Traditional magnetic measurements are generally based on inductive methods to measure the magnetic moment. The induction law, due to M. Faraday, states that a time-varying magnetic flux causes a current to flow in a closed circuit, with electromotive force proportional to $-d\Phi/dt$. So, if a magnetized sample is moved in a controlled way in the vicinity of a pick-up coil, a voltage proportional to the flux and to the number of windings may be measured. The pick-up coils will, of course, be also sensitive to the magnetic field used to magnetized the sample. This contribution may be eliminated through the correct design of the pick-up coils. They are generally wound as a first-order gradiometer (just like the traditional ac susceptometer introduced

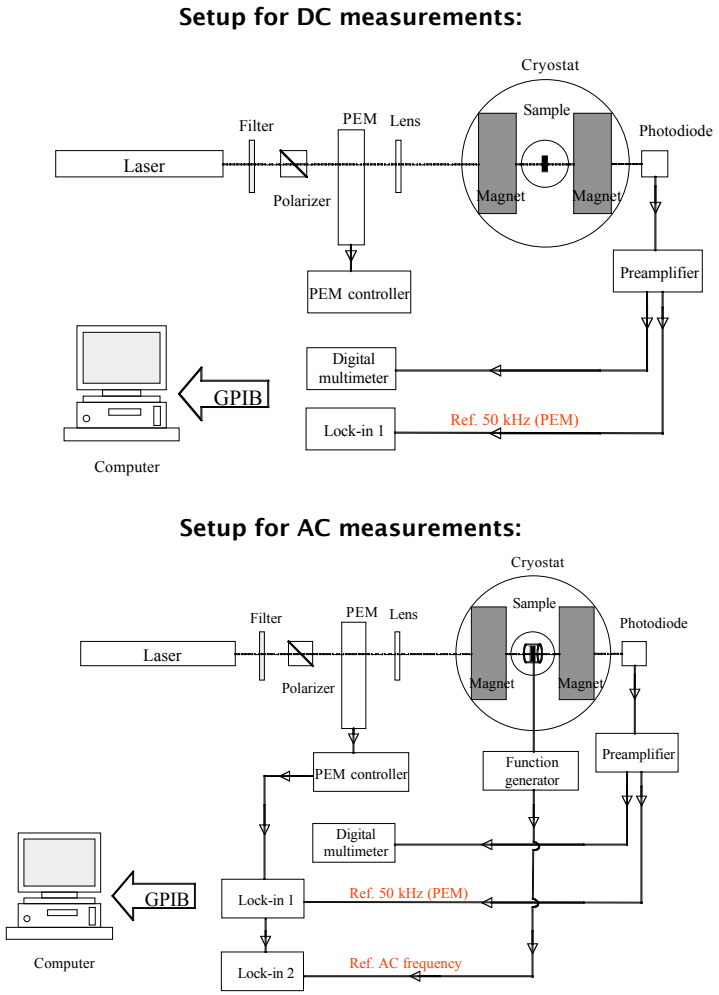

Figure 4.22: Comparison between the DC/MCD and the ac/MCD schemes.

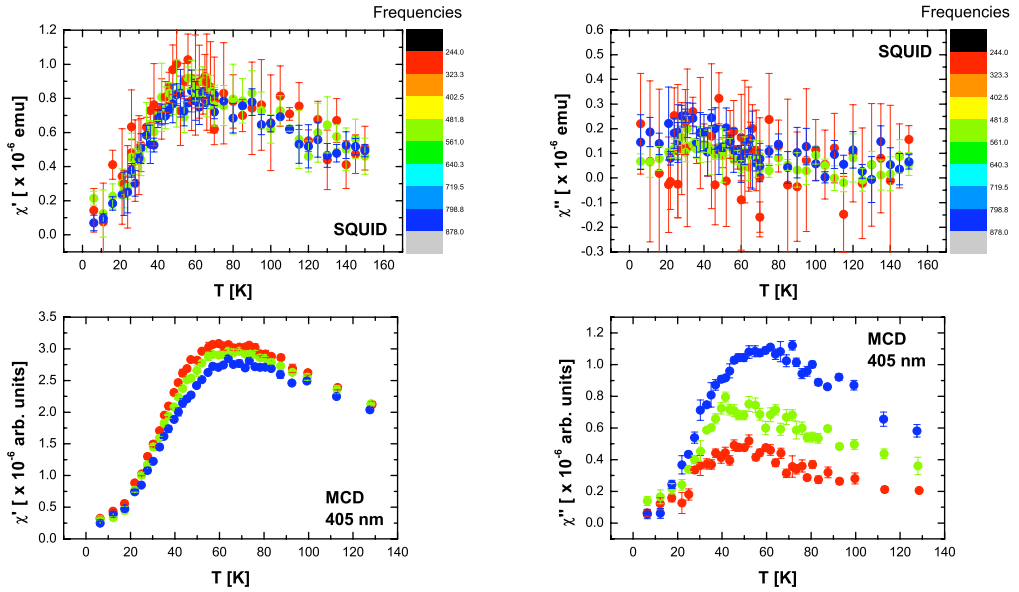

(a) Real part

(b) Imaginary part

Figure 4.23: Comparison between an ac/MCD and a SQUID measurement. The sample is an ensemble of $CoNi_2$ nanoparticles embedded in silica

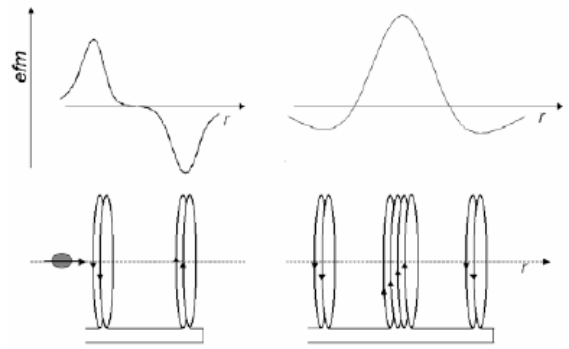

Figure 4.24: The two main pick-up coil geometries used in magnetometer design. On the left-hand side, a first-order gradiometer, and on the right-hand side a second order gradiometer. In both cases the characteristic Voltage x sample position is depicted

in subsection 4.2.1) or a second-order gradiometer (both geometries are shown in figure 4.24). To these basic principles, more complex detection methods are added in order to reach higher sensitivities. Two of these methods, routinely used in magnetic studies of molecular magnets and nanoparticles, will be introduced in the next subsections.

4.3.1 SQUID and VSM magnetometers

In a SQUID (Superconducting Quantum Interference Device) magnetometer, the pick-up coils (generally a second-order gradiometer) are inductively coupled to a SQUID, a ring made of superconducting material interrupted by a Josephson junction, in the case of an RF SQUID, or two Josephson junctions in parallel, in case of a DC SQUID. The device exploits two physical phenomena, the quantization of magnetic flux and Josephson tunneling, to measure magnetic moments with a very high sensitivity (10^{-9} emu). The DC SQUID exploits the interference between a superconducting current that passes through the two branches of the SQUID ring (paths 1 and 2, see figure 4.25). This interference is caused by the phase difference δ that appears when a magnetic flux crosses the ring. The resulting voltage may be measured, and is periodic in the number of flux quanta ($\Phi_0 = h/2e = 2.07$ x10^{-15} Wb) crossing the ring. A more practical way of measuring the magnetic flux, though, is to use a feedback coil to compensate the flux changes sensed by the SQUID when the sample is moved inside the pick-up coil. The feedback voltage

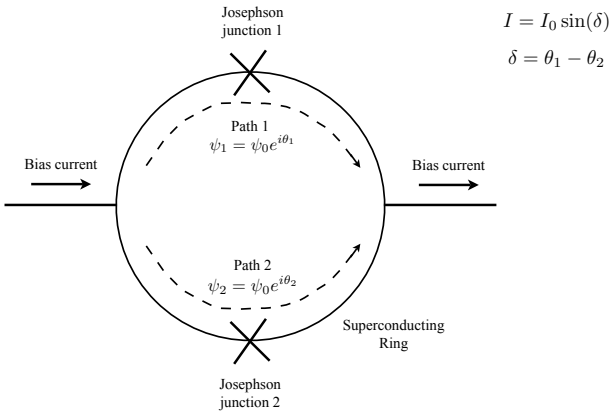

Figure 4.25: The DC SQUID.

will then be proportional to the magnetization of the sample, which can be know absolutely after the system is calibrated with a standard paramagnetic sample (a gadolinium salt, for example). SQUIDs are the ideal instruments for the characterization of molecular magnets, due to their high sensitivity, but this high sensitivity limits the operational magnetic field range to about 8T.

For magnetic measurements at higher fields, the VSM (Vibrating Sample Magnetometer) technique is more suitable. In this case the sample is made to oscillate at frequencies in the 50 – 100 Hz range inside a first order gradiometer. The oscillation is achieved mechanically, coupling the sample holder rod to a magnetic driver similar to that of a loudspeaker. The resulting signal is detected by a lock-in amplifier synchronized to the oscillation frequency. The sensitivity is lower than that of the SQUID, generally by 3 orders of magnitude, but the acquisition is fast and can be done while ramping the magnetic field.

The SQUID magnetometers available can operate from 1.5K up to room temperature (RT) and produce magnetic fields up to 6.5T. They may also perform ac susceptibility measurements with a frequencies ranging from 0.1 Hz to 1000 Hz.

4.3.2 Electron Paramagnetic Resonance - EPR

EPR is an important magnetic resonance technique that provides unique information about the chemical environment of paramagnetic centers, not only for isolated ions but also in systems in which dipolar and exchange interactions between the magnetic centers are present,

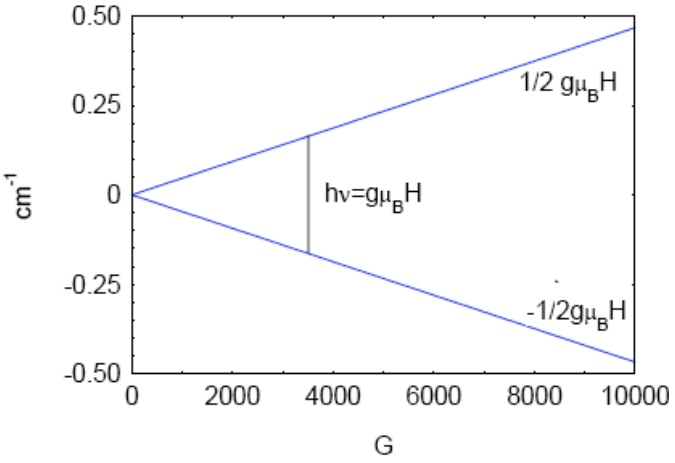

Figure 4.26: Zeeman splitting of a $S = 1/2$ level.

not to mention the potential applications of pulsed EPR in studies of the spin dynamics [4], [115],[116],[117]. EPR spectroscopy measures the absorption of electromagnetic radiation by a paramagnetic system placed in a static magnetic field. While magnetic measurements are able to determine properties that result from thermal averages of energy levels of a given multiplet, EPR gives access to the levels individually. Furthermore, the anisotropy of the **g**, **D**, and **A** tensors (see Section2.1) may be evaluated from the spectra.

As an elementary example, an applied magnetic field (parallel to the z axis) removes the degeneracy of a spin 1/2 energy level. The resulting two energy levels will have energies given by $\pm 1/2 g_z \mu_B H_z$. The energy difference between these two levels is then $\Delta E = g_z \mu_B H_z$ (see figure 4.26), and an electromagnetic field of frequency ν so that $h\nu = \Delta E$ will be absorbed inducing a transition between these energy levels. The frequencies ν lie in the microwave range, and the most commonly used bands, available commercially are: X band - 9GHz; Q band - 35GHz; W band - 95 GHz. Higher frequency spectrometers are "home-made", and may operate with frequencies up to 500 GHz. Due to the technical difficulties involved in the sweeping of frequencies in this range, the basic experiment then consists in measuring the absorption at a fixed frequency while the magnetic field is swept. A small modulation is added to this field, so that the recorded spectrum will show the derivative of the absorption line. In the traditional setup the static magnetic field and the oscillating magnetic field that induces the transitions are

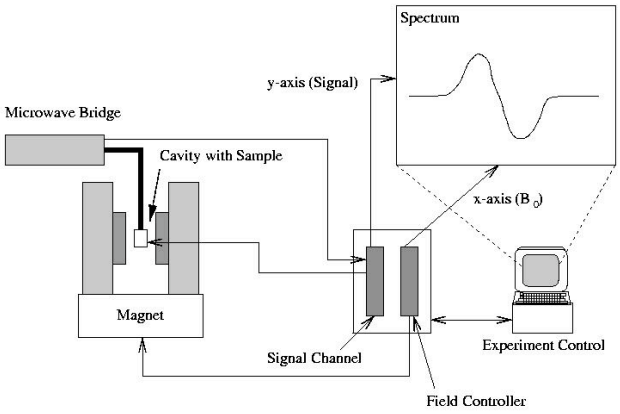

Figure 4.27: Schematics of a typical X-band spectrometer.

orthogonal so that the absorptions follow the selection rule $\Delta m_s = \pm 1$. The simple condition

$$h\nu = \Delta E = g_z \mu_B H_z \tag{4.19}$$

holds and the values of g_x, g_y and g_z are readily obtained from the spectrum, even though the determination of their orientations with respect to the molecular frame needs a single-crystal measurement. In figure 4.27 the schematics of a typical X-band is presented, while in figure 4.28 a theoretical spectrum of a $S = 1/2$ system with anisotropic g is shown.

For systems with $S > 1/2$ the M components can be split even in zero field (zero-field splitting), as was already introduced in chapter 2, section 2.1 with a ZFS Hamiltonian given by 2.13. In this case the spectra become much more complicated. In the simplest case, of an axial ZFS small compared to the Zeeman energy, the energy levels will be quantized along the magnetic field and the resonance fields for the various $m \rightarrow m+1$ levels are given in a perturbational approach by:

$$B(M \rightarrow M+1) = \frac{g_e}{g} B_0 - D' \frac{2M+1}{2} (3\cos^2\theta - 1) \tag{4.20}$$

where H_0 is the resonant field of the free electron, $D' = D/(g\mu_B)$ (D was introduced in 2.12) and θ is the angle between the anisotropy axis and the external magnetic field. For a given orientation each Zeeman line will be split into $2S+1$ components, with the neighboring lines separated by $D'(3\cos^2\theta - 1)$. This is called the fine structure. It is clear that the ZFS parameter may be extracted from the spectrum. But in order to know its signal, a very important information in single-molecule magnet studies, it is necessary to record the spectra at high frequencies

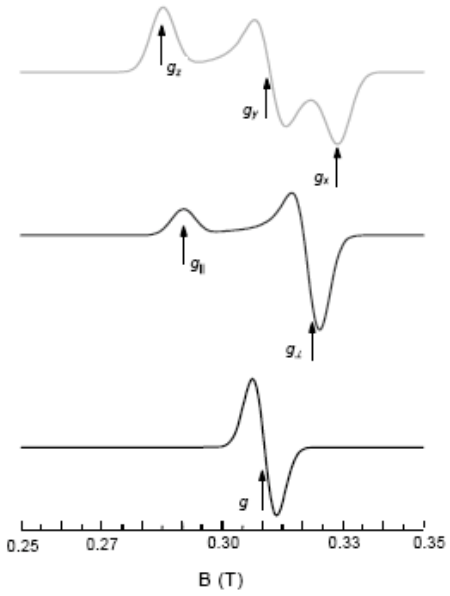

Figure 4.28: Theoretical EPR spectra for a system with $S = 1/2$. On top, $g_x \neq g_y \neq g_z$, in the middle $g_x = g_y = g_\perp, g_z = g_\parallel$, and on the bottom the isotropic g value case.

(high magnetic fields) [118],[119],[120]. Other advantages of HF-EPR are: increased resolution, increased sensitivity, simplification of the spectra (and of the spectral assignments) and observation of transitions in otherwise "silent"species. This last fact is particularly important in SMM studies, because they comprise species with integer S and large separations between neighboring m levels in zero applied field. More details on HF-EPR may be found in the references cited before.

4.3.3 STM – (Scanning Tunneling Microscopy)

Scanning Tunneling Microscopy is a surface characterization technique, part of the wider family of Scanning Probe Microscopies (that include AFM, MFM, EFM, SNOM). It is a very powerful technique for the characterization of surface morphology, local properties and electronic structure with very high spatial resolution. Since 1981, when the first STM was made by G. Binning and H. Rohrer, it has become an essential tool in surface physics, thin-film physics and nanotechnology in general.

The principle of operation is based on the presence of a tunneling current between the conductive surface under study and a very sharp metallic tip very close to this surface when a voltage

difference is established between tip and surface. The typical tip-surface distance is of the order of several Angstroms, and the bias voltage is of the order of 1 V. In this case, the current density is given by the following formula (in which a 1D current flow is considered) [5],[121],[122]:

$$j_t = j_0(V)e^{-\frac{4\pi}{h}\sqrt{2m\phi^*}\Delta Z} \tag{4.21}$$

where j_t is the tunneling current density, $j_0 = e/2\pi h(\Delta Z)^2$, ΔZ is the tip - surface separation, e is the electron electrical charge, m is the electron mass, h is Planck's constant and ϕ^* is the average energy barrier height. Because of the exponential dependence of (4.21) with ΔZ, the tunneling current is very sensitive to small variations in the surface topography. STM's high sensitivity at the atomic scale is a consequence of this fact.

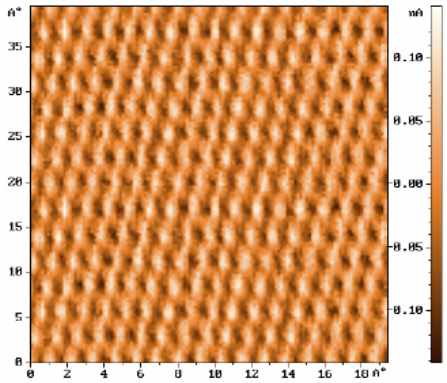

Figure 4.29: STM image of a pyrolitic graphite surface, evidencing the atomic structure of this surface. From [5]

In order to obtain an image, the tip must perform a raster scan of the sample surface (and the surface must be conductive), a line-by-line scanning process analogous to the that of the electron beam in a television cathode ray tube. Obviously, the tip displacements during a scan must be performed with Angstrom resolution in order to obtain a high resolution image. This is achieved by using piezoelectric ceramic drivers to perform the tip translations in the XY plane. Another critical parameter for achieving high lateral resolution is the quality of the tip, that must be correctly prepared if one has to obtain images with atomic spatial resolution. During the scan of a line, the surface height profile will change ΔZ, thus modulating the tunneling current. In the constant current operation mode, then, a negative feedback circuit drives a piezoelectric

translator that vertically displaces the tip in order to keep the tunneling current constant. The voltage applied to this vertical piezoelectric translator will then reproduce the surface topography along the line. This is recorded for each line in the scan, and at the end a computer graphic is generated, reproducing the height profile of the surface with a color map. In figure 4.29 the STM image of a surface of pyrolitic graphite is shown, as an example of the atomic resolution achievable with this technique.

In this work, STM was employed, in collaboration with Dr. Matteo Mannini and Francesco Pineider, from the Laboratory of Molecular Magnetism, in order to characterize Self-Assembled Monolayers of Mn12 and Fe4 SMM clusters on Au surfaces (6.2.1), check the surface density of clusters and the success of the deposition process, as well of the roughness of some of the substrates, as will be discussed in more details in chapter 6, subsection 6.2.1. More details about STM, and SPMs in general, may be found in [5].

5 Magneto-optical studies of nanocomposites containing magnetic nanoparticles

In this chapter, the magnetic and magneto-optical investigations made on nanocomposite samples of $Co_{100-x}Ni_x$ and Au-Fe nanoparticles embedded in SiO_2 will be presented and discussed. Nanocomposites of this kind have been drawing much attention due to the possible uses in ultra-high density data storage and Tunnel Magnetoresistance (TMR) devices. Moreover, they offer the possibility of studying the behavior of magnetic nanoparticles in high dilutions, a situation in which the interparticle interactions should be minimized. The transparent matrix offers the further possibility of optically probing the magnetization, allowing the study of the interplay between optical properties and magnetism. Two sample preparation strategies, sol-gel synthesis and ion implantation, will be briefly introduced, followed by the results of magneto-optical and magnetic measurements. The comparison between these two methodologies will be presented and the eventual disagreements between data obtained in both cases will discussed.

5.1 $Co_{100-x}Ni_x$ nanoparticles

The $Co_{100-x}Ni_x$ series of nanoparticles embedded in Silica were prepared by the Sol-Gel method (by G. De from the Central Glass and Ceramic Research Institute, Kolkata, India [6]). This is a powerful nanocomposite preparation technique because both cluster and matrix composition may be controlled at the synthesis level. Many other transition metal alloys of magnetic interest may be produced by this method, for example Nd-Fe, Fe-Cr, Fe-Ni, Cu-Ni and Fe-Co ([6] and references therein).

The synthesis starts with the preparation of the sols, from $Si(OC_2H_5)_4$(TEOS), $Co(NO_3)_3{\cdot}6H_2O$, $Ni(NO_3)_3{\cdot}6H_2O$, HNO_3, H_2O, n-propanol and isobutanol (TEOS = tetraethyl orthosilicate). The molar ratio of total metal (pure or mixed Co + Ni) is kept constant in all the films at 10 equiv mol % metal/90% $Si)_2$. The details of this synthesis are presented in [6]. The films containing the nanoparticles are prepared by dip-coating of silica slabs (type II, Heraeus) in the sols and

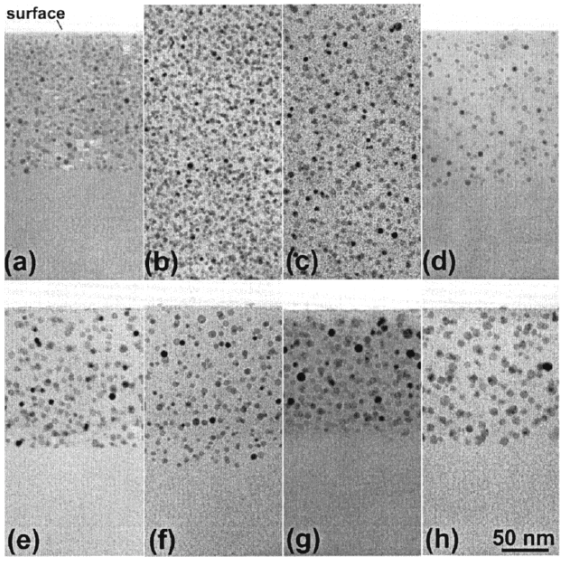

Figure 5.1: Cross-sectional TEM bright-field images of the samples Co_xNi_{100-x}: (a)$x = 0$ (pure Ni), (b)$x = 33$ (planar view), (c)$x = 50$ (planar view), (d)$x = 66$, (e)$x = 70$, (f)$x = 75$, (g)$x = 80$, (h)$x = 100$ (pure Co). From [6]

subsequent thermal treatment (annealing) under controlled atmosphere. It is during this stage of the preparation process that the alloy nanoparticles are formed. These film's thicknesses were measured by TEM and lie between 120 and 150 nm from the surface of the slab. The nanoparticles are randomly distributed and there is no preferred orientation of any kind. The morphology and structure of these nanoparticles are also known from Transmission Electron Microscopy (TEM) characterization [6]. In all the compositions, well-defined spherical particles with diameters ranging from about 3 nm in the pure Ni sample to about 6 nm in the pure Co sample were found (figure 5.1, table 5.1). SAED (selected area electron diffraction) analysis indicates that the particles have an fcc structure in all cases, regardless of the Co fraction. (Co nanoparticles may have fcc or hcp structures, which is highly dependent on the preparation technique. More details may be found in [123]). It is believed that this fact causes an enhancement of the magnetic moment per atom in the pure Co, besides the already verified increase in the Ni particles, in certain cases superior to 30%, as demonstrated by magnetic measurements performed by G. Mattei et al. in [6].

Sample	Cluster Diameter (mm)
Co_{100}	6.5 ± 1.7
$Co_{80}Ni_{20}$	6.1 ± 1.7
$Co_{75}Ni_{25}$	4.7 ± 1.3
$Co_{70}Ni_{30}$	4.7 ± 1.2
$Co_{66}Ni_{33}$	4.1 ± 1.3
$Co_{50}Ni_{50}$	3.5 ± 1.0
$Co_{33}Ni_{66}$	3.3 ± 1.2
Ni_{100}	3.1 ± 1.0

Table 5.1: Particle diameters determined by TEM for the entire family of Co_xNi_{100-x} nanoparticles prepared by the Sol-Gel technique. From [6]

5.1.1 MCD measurements

The MCD hysteresis loops measured at 1.5K for the entire family of Co_xNi_{100-x} nanoparticles are shown in figure 5.2. The measured curves are in principle in good agreement with the SQUID magnetic measurements for this family of clusters, shown in figure 5.3.

But the similarities are only qualitative. The saturation values of the magnetic moment per atom and of MCD do not display the same dependence on the cobalt fraction, as seen in figure 5.4. When the composition changes from Ni_{100} to $Co_{33}Ni_{67}$ there is a small reduction of 12% in the saturation magnetic moment, while the saturation MCD displays an increase of 130%. Further increase in the cobalt fraction causes both the saturation MCD and the magnetic moment to increase by 67% and 70% respectively. But while the magnetic moment keeps increasing up to the maximum value for the pure cobalt samples, the MCD does not follow the same trend, with an abrupt drop at a cobalt fraction of 80%, suggesting that, the correspondence of the hysteresis cycles measured by MCD is only qualitative. The relation between the maximum MCD and the magnetization is not a simple proportion as would be initially expected from the theory presented in chapter 3. Looking at equation 3.25 in that chapter, we can see that these changes must arise from light-induced modifications in the off-diagonal dielectric tensor component K' (K' is its real part, but both real and imaginary parts are influenced by the incident light as will be shown in (5.1)). The exact value of the refractive index of alloy nanoparticles is not know a priori, so an average, weighted according to the fractions of Co and Ni, of the bulk values

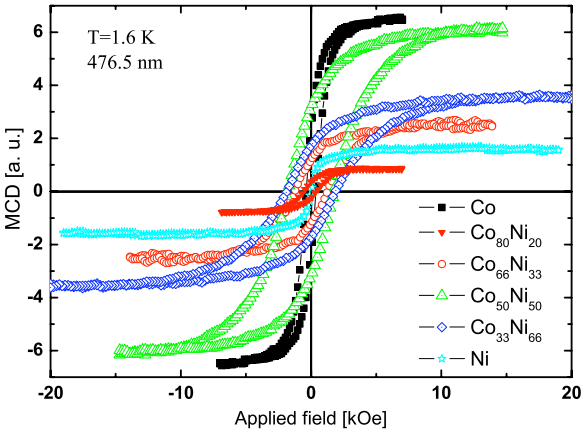

Figure 5.2: MCD hysteresis loops (at 1.8K) of the following samples: pure Ni, $Co_{33}Ni_{66}$, $Co_{50}Ni_{50}$, $Co_{66}Ni_{33}$ and pure Co. Notice the reduction in the net saturation MCD as the Ni fraction increases. From [7]

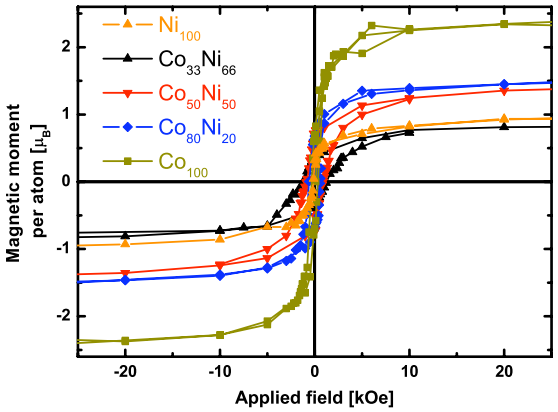

Figure 5.3: Hysteresis loops (at 3.0K) of the following samples: pure Ni, $Co_{33}Ni_{67}$, $Co_{50}Ni_{50}$, $Co_{80}Ni_{20}$ and pure Co, measured in a SQUID magnetometer.

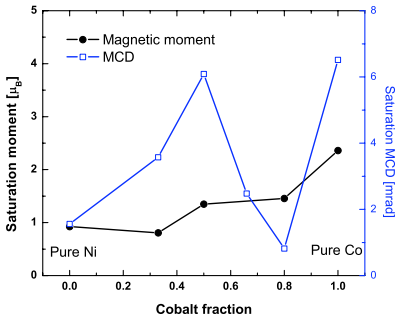

(a) The saturation values of the MCD and of the magnetic moment per atom of the Co_xNi_{100-x} samples in function of the cobalt fraction x. These values were taken from data in figures 5.2 and 5.3

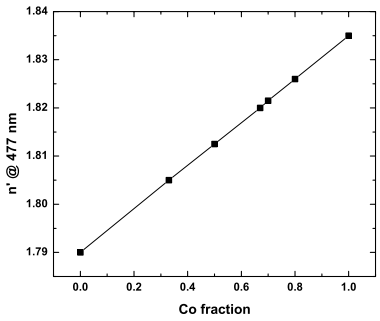

(b) The average between the real parts (n') of the refractive indexes of Co and Ni, weighted according to the relative fractions of these elements in a nanoparticle.

Figure 5.4: Saturation MCD, saturation magnetic moment and the approximated real part of the refractive index of some of the Co_xNi_{100-x} nanoparticles.

for Co and Ni, as reported in [124][1], was considered in order to have a rough estimate of the refractive indexes of these nanoparticles and their effects on the Faraday ellipticity as given by (3.25). This relation between $\overline{n}'$ and the Co fraction is shown in figure 5.4. Because of 3.25 this contribution alone should only cause a monotonic decrease in the MCD as the Co fraction increases. On the other hand, the components of the dielectric tensor are intrinsically dependent on the wavelength of the light incident on the material, its polarization as well as on the electronic structure of the material. This dependence is generally very complicated, and different from the bulk case. Quantum size effects [125], [126] cause the electronic energy bands in nanoparticles to be narrower with respect to the bulk, forming discrete energy bands, which causes the depart of nanoparticle properties related to their electronic structure from the bulk equivalents. The investigation of phenomena connected nanoparticle electronic properties could in principle give insight in several phenomena observed in these systems, including the magneto-optical effects studied here. This dependence on electronic structure, however, is still a matter of discussion as the investigations of the electronic structure of magnetic nanoparticles is subject of current research efforts. So most results found in the literature consider the free-electron contribution to the optical constants as given by the Drude model, but for 3d metals interband transitions, due

[1] Values tabulated at: http://www.luxpop.com/

to unfilled d-bands, must be considered. Solid state theory of a screened and interacting electron gas yield the following general expressions for the real and imaginary parts of the dielectric constant ε [127]:

$$\begin{aligned}\varepsilon'(\mathbf{q},\omega) &= 1 - \frac{e^2}{V_g \varepsilon_0 q^2} \sum_{\mathbf{k}} P\Big[\frac{f_0(\mathbf{k}+\mathbf{q}) - f_0(\mathbf{k})}{E(\mathbf{k}+\mathbf{q}) - E(\mathbf{k}) - \hbar\omega}\Big] \\ \varepsilon''(\mathbf{q},\omega) &= \frac{\pi e^2}{V_g \varepsilon_0 q^2} \sum_{\mathbf{k}} [f_0(\mathbf{k}+\mathbf{q}) - f_0(\mathbf{k})]\delta(E(\mathbf{k}+\mathbf{q}) - E(\mathbf{k}) - \hbar\omega)\end{aligned} \tag{5.1}$$

where $f_0(\mathbf{k})$ is the Fermi distribution function, V_g is the volume of the electron gas and $P(z)$ refers to the principal value of z. The imaginary part of the dielectric constant is connected with the absorption constant of the electron gas. We see from the δ-function in 5.1 that absorption always occurs when the energy of the incident wave $\hbar\omega$ is equal to the difference in energy between two states $\mathbf{k}$ and $\mathbf{k}+\mathbf{q}$. It is possible to approximate ε' of 5.1 as:

$$\varepsilon'(\omega) = 1 - \frac{\omega_p^2}{\omega^2} \tag{5.2}$$

demonstrating that the real part of the dielectric constant, ε', goes to zero if the frequency of the excitation wave, ω, corresponds to the plasma resonance frequency ω_p. This frequency is related to the frequency of the surface plasmon resonance (SPR), the collective oscillation of the surface electrons in nanoparticles, through the following expression [128]:

$$\omega_{sp} = \frac{\omega_p}{\sqrt{1+2\varepsilon_m}} \tag{5.3}$$

where ω_m is the dielectric constant of the medium (SiO_2 in our case), assumed to be wavelength-independent. For small particles, in which most atoms are located on or near the surface, this is the dominant plasma oscillation phenomenon. This fact suggests that the presence of this collective oscillation of the electronic density is strongly affecting the magnetism of the $Co_{33}Ni_{67}$ alloy nanoparticles, as can be seen from the magneto-optical response. The mechanism behind this phenomenon is still not well understood. It is evident that, as mentioned in the previous paragraph, the Faraday ellipticity (and so the MCD) depend on the real part of a component of the dielectric tensor, so the presence of plasma oscillations of the electrons that are also responsible for the system's magnetism will influence its magnetic behavior.

The strong influence of the probe light in the magnetism of these nanoparticles may be further appreciated in figure 5.5, where the MCD hysteresis cycles for the $Co_{33}Ni_{67}$ sample are shown for measurements made with several probe light wavelengths. It is clear that the coercive field

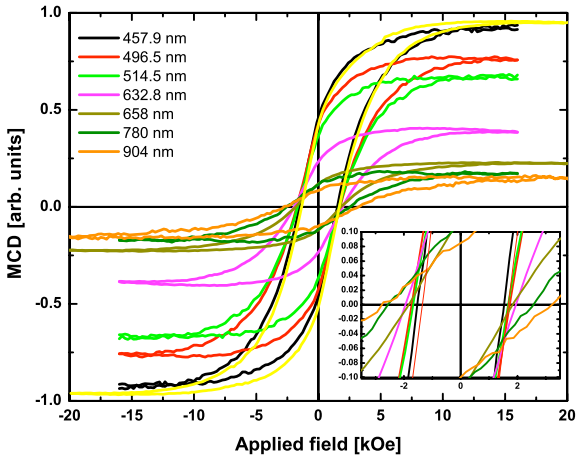

Figure 5.5: MCD hysteresis loops of the $Co_{33}Ni_{67}$ sample with several wavelengths, at 1.5K. Notice the increase in coercivity as the wavelength increases. In the inset the coercivity region on the Applied field axis is enlarged.

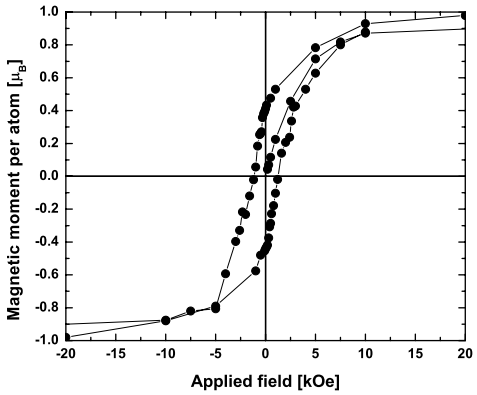

Figure 5.6: Hysteresis loop of the $Co_{33}Ni_{67}$ sample measured at 3K in the SQUID magnetometer.

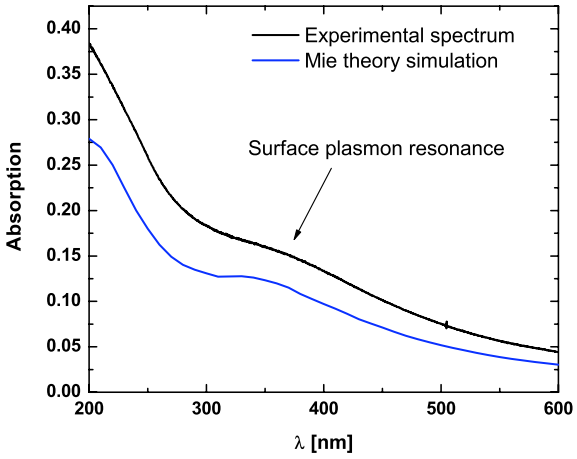

Figure 5.7: UV-Vis absorption spectrum of the $Co_{33}Ni_{67}$ sample, and simulation based on Mie Theory for comparison. The broad absorption band centered around 350 nm corresponds to the surface plasmon resonance of these nanoparticles. The spectrum was acquired at room temperature.

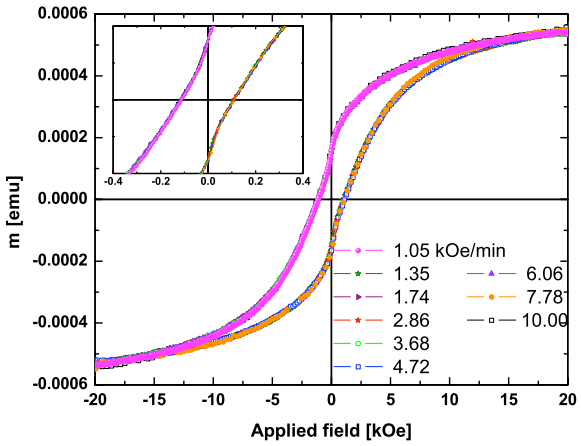

Figure 5.8: Hysteresis loops of the $Co_{33}Ni_{67}$ sample measured at 1.5 K with several different magnetic field sweep rates between 0.1 and 1 T/min. The inset shows the coercivities.

significantly increases as we go from shorter to longer wavelengths, from values around 2200 Oe with 405 nm to 3500 Oe with 904 nm light. This dependence, which appears to be linear, is shown in figure 5.9. Moreover, the observed coercivities are always larger than the values obtained from SQUID measurements, always around 1200 Oe (figure 5.6). In order to rule out the possibility that the long waiting time of SQUID measurements was causing the observed reduction in coercivity (the reader must remember that the measurement time plays a significant role in the characterization of superparamagnetic systems, as explained in chapter 2), hysteresis cycles were also measured with a VSM in which the field can be swept at 10 kOe/min, the same rate used in the MCD measurements. The results are shown in figure 5.8 for the $Co_{33}Ni_{67}$ sample at 1.5K. It is evident that sweep rates from 1 up to 10 kOe/minute do not have a significant influence on the value of the coercivity.

The temperature dependence of the H_c from MCD measurements, for 3 wavelengths, is shown in figure 5.10. It is seen that in all cases (magneto-optical, magnetometric) the coercivities converge to the same value of temperature, vanishing around 28 K. The MCD hysteresis cycles of $Co_{33}Ni_{67}$ were then measured with several incident laser powers and 4 wavelengths in order to check the possibility of sample heating caused by the laser bring back the coercivity values obtained from magnetometric (SQUID/VSM) characterization. As seen in figure 5.10, the

use of very high powers leads to a decrease of H_c, but for the most intense probe beams the coercivity remained slightly above the 1200 Oe value. The obtained H_c's display an exponential dependence on the incident optical power, reaching values no lower than 1300 kOe for the highest incident optical powers. On the other hand, for very low incident powers the coercivity increases significantly, yielding different values for different probe-light wavelengths for the lowest achieved probe powers. This demonstrates that, even if the sample is being heated by an intense optical field, the resulting temperature change is not enough to accelerate the dynamics to the same rates as observed when the sample is not irradiated, as in magnetometric measurements. This fact could suggest that the electronic oscillations induced by light are increasing the anisotropy energy barrier of the system. The amplification of the effect for very low light powers gives support to our belief that the excitation of a plasma resonance (see equation (5.2)) is intimately linked to the observed effect, as even very small external perturbations (the electric field of the probe light in this case) will produce strong internal fields in the electron gas of the nanoparticles if the frequency of the perturbation is in the vicinity of the plasma resonance frequency.

Observing the optical absorption spectra of $Co_{33}Ni_{67}$, in figure 5.7, we an see the presence of a resonance at around 350 nm. This corresponds to the surface plasmon resonance of these nanoparticles, as confirmed by the Mie theory-based [129] simulation presented in 5.7 (the simulation was made employing a MATLAB code based on the following works: [130], [131]). Observing the data in figure 5.9 we can see that the coercivity decreases as the probe light wavelength gets closer to the plasmon resonance wavelength, suggesting that it might be playing a major role in the observed phenomenon.

Besides the plasmonic resonance-induced effect, the occurrence of a photomagnetic effect in these nanoparticles could also be present. The wavelength dependence of H_c was observed only in the alloy nanoparticles, and was stronger in the case of $Co_{33}Ni_{67}$. In order to demonstrate this, the MCD hysteresis cycles of the Co_{100} sample measured at two different wavelengths are shown in figure 5.11. Both measurement essentially yield the same values for H_c. Photomagnetic effects, especially photoinduced magnetic anisotropy, have been observed and studied for a long time especially in yttrium iron garnets (YIG) [132], [133], [134] and ferrites [135]. In these materials, the photoinduced magnetic anisotropy process may be understood as resulting from the charge transfer between dopant ions (Co, Si, Pb, to mention some examples) in inequivalent lattice sites (tetrahedral or octahedral) with different valences. The different contribution to the magnetocrystalline anisotropy arising from these inequivalent sites then changes the overall anisotropy of the material. In our case, however, the structure is fcc (the ferrites studied in [135]

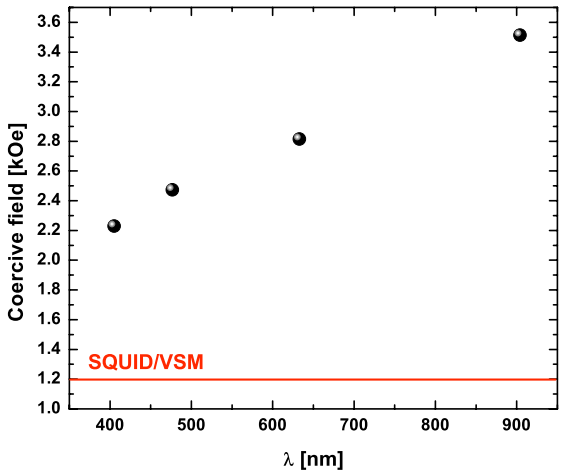

Figure 5.9: The wavelength dependence of $Co_{33}Ni_{67}$'s coercivity. The wavelength monotonically decreases as the measurement wavelength gets closer to the surface plasmon resonance wavelength.

have a inverse spinel structure, and YIG has a structure with magnetic ions occupying tetrahedral and octahedral sites) as has been demonstrated in [6]. $Co_{33}Ni_{67}$ particles have delocalized electrons, so there can be no charge transfer effects. Furthermore, we observe a continuous change in H_c, in contrast to the discrete wavelengths at which photomagnetic effects are observed. So, the possibility of photomagnetism contributing to the observed effect can be ruled out.

5.1.2 AC/MCD measurements

In order to gain further insight in this interesting phenomenon, the ac susceptibility of the $Co_{33}Ni_{67}$ sample was measured in a traditional, SQUID-based, ac susceptometer, and in our original ac/MCD susceptometer. Up to now, the only reference found about such magneto-optical measurements is del Real et al. [136], in which a MO ac susceptibility measurement was performed in γ-Fe_2O_3 nanoparticles dispersed in a silica matrix. The results are shown in figure 5.12, where the temperature dependence of the ac susceptibility was measured with two wavelengths (405 and 632.8 nm). The SQUID measurement is shown in figure 5.13, for comparison.

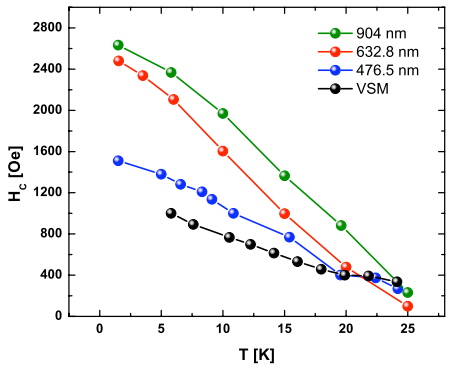

(a) Temperature dependence of the coercivity of the $Co_{33}Ni_{67}$ sample for 3 different measurement wavelengths and for a VSM measurement.

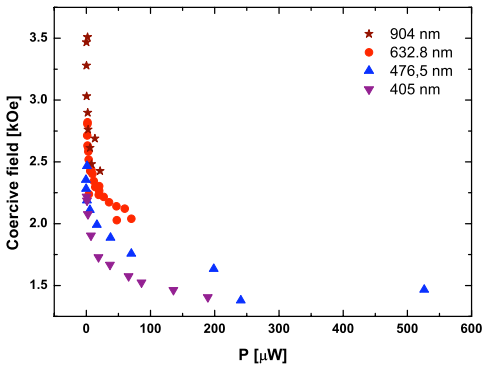

(b) The dependence of the observed coercivity with the incident laser power.

Figure 5.10: Temperature and incident optical power dependence of the coercive field of $Co_{33}Ni_{67}$.

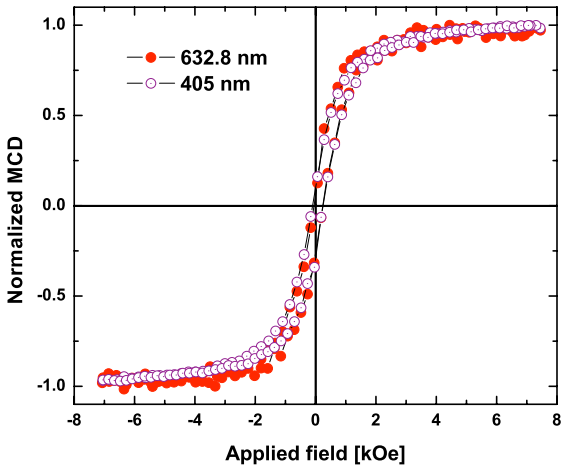

Figure 5.11: MCD hysteresis cycles of Co nanoparticles measured at 1.5 K. The coercivity clearly displays no significant dependence on the light wavelength.

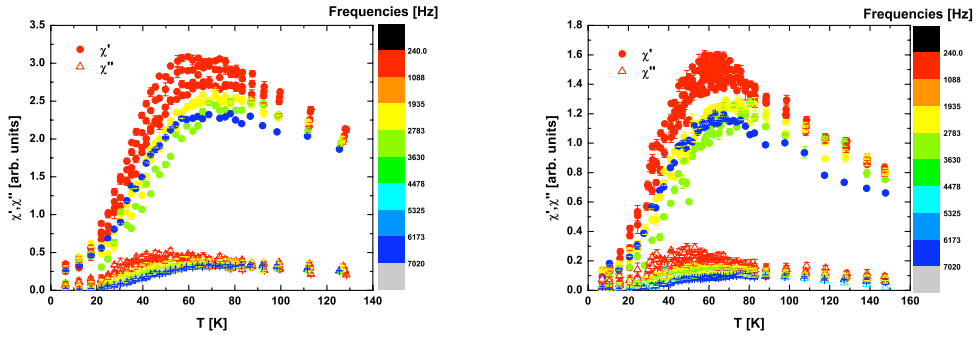

(a) ac/MCD with 405 nm light.

(b) ac/MCD with 632.8 nm light

Figure 5.12: Temperature dependence of the ac-susceptibility of the $Co_{33}Ni_{67}$ sample, performed with the magneto-optical ac susceptometer. χ' is the real part and χ'' is the imaginary part of the susceptibility.

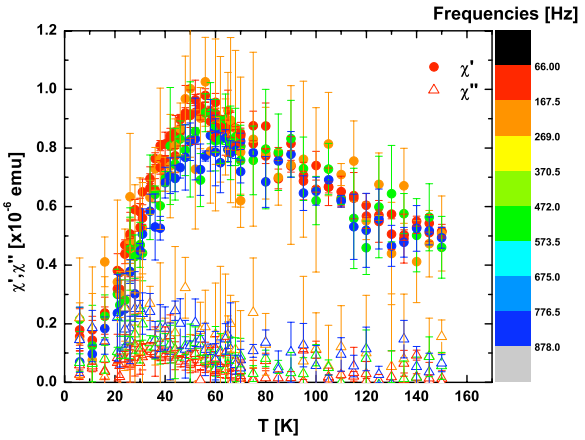

Figure 5.13: Temperature dependence of the ac susceptibility of $Co_{33}Ni_{67}$ measured in a SQUID susceptometer.

The magneto-optic measurement is clearly less noisy, indicating a better sensitivity of the instrument to this sample compared to the SQUID susceptometer. This is a positive result, demonstrating the successful development of this magneto-optical measurement setup. The curves display the characteristic behavior of a superparamagnetic system, with the appearance of a frequency-dependent out-of-phase component (χ'') of the susceptibility around the average blocking temperature of the system. The maxima of these curves yield the average blocking temperature for the time-scale set by the measurement frequency (see chapters 2, section 2.2 and 4, section 4.2). Considering equation 2.25, the average blocking temperatures thus obtained may be plotted against the natural logarithm of the relaxation time (given by the reciprocal of the frequency). If the magnetization of the system relaxes through a thermally activated process, the relaxation times τ will be given by the Arrhenius law 2.25 and $ln(\tau)$ x $1/T$ will produce a straight line. The equation is:

$$ln(\tau) = ln(\tau_0) + \frac{KV}{k}\langle T_B \rangle \tag{5.4}$$

where KV/k is the average anisotropy energy barrier and $\langle T_B \rangle$ is the average blocking temperature. From a linear fit to the data the value of the pre-exponential factor ($\tau_0 = 1/f_0$ where f_0 is the attempt frequency) and of the average anisotropy barrier may be inferred. These Arrhenius plots for both magneto-optic measurements as well as for the SQUID measurement are shown

	KV/k (K)	τ_0 (s)
405 nm	407 ± 25	1x10^{-6}
632.8 nm	408 ± 20	8x10^{-7}
SQUID	420 ± 68	1x10^{-8}

Table 5.2: The best fit values for the average anisotropy energy barrier and the pre-exponential factor of the $Co_{33}Ni_{67}$ sample.

in figure 5.14. The best fit values for τ_0 and KV/k are presented in table 5.2:

The magneto-optic and the SQUID measurements yield roughly the same values, within the error bars, to the average anisotropy barrier, while there is a change of two orders of magnitude in the pre-exponential factor τ_0 when we change the measurement method. This result suggests that the interaction with light is in principle not inducing major changes in the anisotropy barrier of the clusters but rather in their characteristic attempt frequency $f_0 = 1/\tau_0$. According to the Néel-Brown model, τ_0 is given by [137]:

$$1/\tau_0 = f_0 = 2\alpha\gamma H_k \sqrt{\frac{4KV}{\pi k_B T}}(1 - H/H_k)^2 \tag{5.5}$$

where γ is the gyromagnetic ratio, α is the spin precession damping factor (from the Landau-Lifshitz-Gilbert equation) and H_k is the switching field. It is important to stress that τ_0 is also dependent on the anisotropy barrier energy KV. The plasma oscillations present in these nanoparticles may stimulate or hamper the magnetization reversal process. The fact that the coercivity obtained from MCD measurements is always larger than the magnetometric values indicates that in principle electronic collective oscillations hamper the magnetization reversal process yielding high coercivities. As the oscillation gets stronger (measurement wavelength closer to the surface plasmon resonance, see figure 5.7), the reversal process is stimulated and the coercivity decreases (see figure 5.9). The mechanism involved must still be understood, but the results of ac susceptibility measurements presented above suggest that factors introduced by the precessional spin dynamics given by the Landau-Lifshitz-Gilbert equation $\frac{d\vec{M}}{dt} = -\gamma_0 \vec{M} \times \vec{H_{eff}} - \frac{\gamma_0 \alpha}{M_S} \vec{M} \times (\vec{M} \times \vec{H_{eff}})$, that lies on the heart of the Néel-Brown model for magnetization reversal of nanoparticles, are strongly influenced by the surface plasmon resonance and strongly affect the system's attempt frequency τ_0. The measurement of hysteresis cycles by means of MCD in principle suggested a modification of the effective anisotropy barrier height, but the ac susceptibility results indicate that a more subtle and complex process is

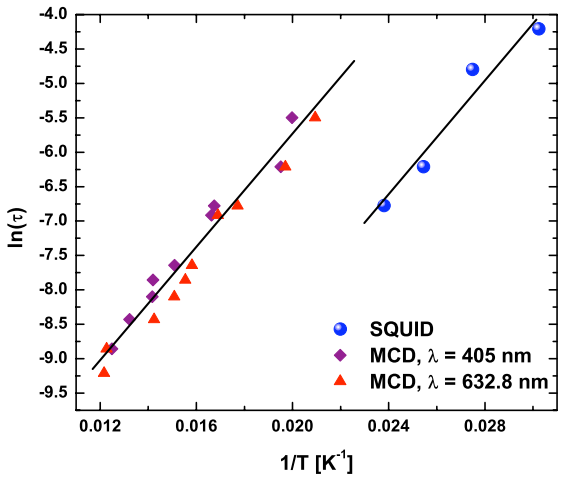

Figure 5.14: Arrhenius plots for the magneto-optical and SQUID ac susceptibility measurements, $Co_{33}Ni_{67}$. The lines are only a guide to the eyes.

responsible for the observed phenomenon.

5.2 Ion-implanted Au-Fe nanoparticles

5.2.1 Preparation and measurements

The influence of the surface plasmon resonance in the magnetic and magneto-optical properties of nanoparticles may be further observed in a series of Au-Fe samples embedded in a silica matrix. This is a new system in which the combination of a magnetic 3d metal (Fe) with a noble metal (Au) may lead to novel phenomena arising from the interaction of optical (plasmonic) and magnetic properties of the elements of the alloy. In particular enhancements of the anisotropy and of magneto-optical response could be achieved, considering that gold has large spin-orbit coupling.

These samples were prepared by sequential ion implantation at the Physics Department of the University of Padova, by the group of G. Mattei, P. Mazzoldi and C. de Julián Fernández [9],[53]. Ion implantation is a method to prepare metal nanoparticles/insulating matrix composites with good control of the composition and a great flexibility offered by subsequent thermal treat-

ments. Structures that are not thermodynamically stable in the bulk may be achieved through this out-of-equilibrium technique. Moreover, the high surface-to-volume ratio contributes to the stabilization of out-of-equilibrium structures, as found in interfaces and surfaces. The mixing of immiscible species is possible due to the very fast ($\sim$ ps) intermixing process induced in the diffusion/scattering of the cascade of high-energy ions, with local peak temperatures at the target reaching very high values and the subsequent release of this energy to the silica matrix leading to the quenching of the structure [138]. Subsequent thermal treatments relax the obtained sample structurally in a way that the bulk structure may then be achieved.

The technique is based on generating, by sputtering, a plasma with the ions to be implanted. The ions are extracted from the plasma and pre-accelerated so that they can be separated according to their masses by means of a magnetic field. The resulting beam is then accelerated up to the desired energy and directed to the substrate, with penetration depths forming a profile that strongly depends on the beam energy (a schematic representation of the apparatus is shown in figure 5.15) [138]. The dose and energy of the implanted ion will determine the final concentration profile of the implanted species into the solid. If the dose is large enough, NPs can nucleate inside the substrate. Even if the doses are low, subsequent annealing can promote the diffusion of the ions and, therefore, the nucleation of NPs. The main advantage of the technique is that by controlling the implantation parameters (dose and energy) and the subsequent annealing process (temperature, time, and atmosphere), it is possible to tailor the NP composition, size, and spatial distribution. The technique is particularly suitable for the development of alloy nanoparticles, in which case more than one ion must be implanted sequentially. This implantation order can completely change the structure of the resulting nanoparticles, with alloys[9] as well as core-shell structures being achieved [139]. It is also possible to achieve alloys of otherwise immiscible metals, as for example Fe and Au.

The samples studied are labeled Au9Fe9, Au3Fe9, Au3Fe3, Fe9 and Au3. The Au9Fe9 sample was obtained via the implantation of 9 x 10^9 Au^+ ions/cm^2 at an energy of 90 keV on pure silica slabs (Herasil 1 by Heraeus) and the sequential implantation of the same dose of Fe^+ ions at 110 keV. These energies are chosen as to cause the penetration depth profiles of both ions to overlap. The Au3Fe3 sample was prepared by implanting the same ratio of Au and Fe ions with a dose of 3 x 10^6 ions/cm^2 for each species, and a Au3Fe9 sample was prepared with doses equivalent to the Fe9 for Fe ions and Au3 for Au ions. The samples of single ions, Fe9 and Au3, were prepared with doses equal to 9 x 10^9 ions/cm^2. Cross sectional TEM (figure 5.16, [9]) of the obtained nanoparticles indicate a broad size distribution, with average diameters between 2 and 4 nm, with larger particles with up to 20 nm also present. Most of the particles are concen-

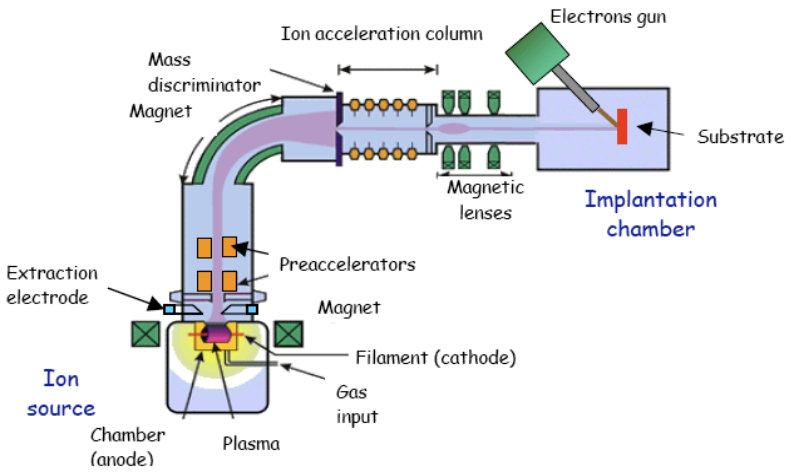

Figure 5.15: Schematic drawing of the apparatus used to prepare ion implanted samples. From [8]

trated in depths between 60 and 70 nm, in good agreement with the nominal value of 70 nm, given by the implantation beam energies.

Structural characterization[2] by means of Grazing Incidence X-Ray Diffraction (GIXRD) of the samples (Au3, Fe9, Au9Fe9, Au3Fe3 and Au3Fe9) gives further support to this nanostructure. GIXRD spectra of the Au3 sample exhibit broad peaks centered at the 2θ angles corresponding to fcc Au. On the other hand, iron implants give rise to more complex nanostructures [53] in which free ions, oxides and nanoparticles can be present, whose dimensions increase for larger doses [53]. The GIXRD spectrum of the Fe9 sample exhibits only a broad peak centered around 45.0° that can be related to the presence of more Fe than Fe oxides. Scherrer's formula yields grain sizes around 3 nm. As in the case of Fe9 and Au3, the GIXRD spectrum of the Au3Fe3 and Au3Fe9 present very broad peaks whose positions are nearer those of fcc Au than those of bcc Fe. On the other hand, the spectrum of the Au9Fe9 clearly presents narrow peaks with angular positions that correspond to an fcc structure with a lattice parameter of $0.3951(1)$ nm, a value smaller than that corresponding to fcc Au (0.4082 nm) but larger than that corresponding to fcc Fe ($0.34 - 0.388$ nm) [140], [141]. Compositional analysis by means of SAED (Selected Area Electron Diffraction) indicates the presence of a single fcc crystalline structure corresponding to the one obtained by GIXRD data. EDS (Energy Dispersive Spectroscopy) compositional analysis with an electron probe size of 1 nm FWHM focused on

[2]Done by G. Mattei, P. Mazzoldi, C. de Julián Fernández and V. Bello, University of Padova

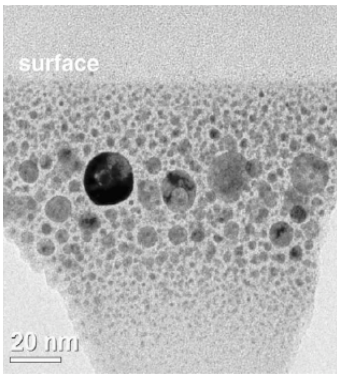

Figure 5.16: Cross sectional TEM of a . From [9]

isolated clusters shows that Au and Fe signals are present together in the spectrum of Au9Fe9. The measured Au/Fe atomic ratio on the largest clusters is about 1.6 ± 0.2, indicating in this case an Au-enriched alloy of composition around $Au_{60}Fe_{40}$.

The optical absorption spectra of these samples are shown in figure 5.17. The Au3 sample exhibits the classical broad peak around 535 nm that corresponds to the excitation of the surface plasmon resonance in nanometric Au particles embedded in SiO_2 matrix [53]. The Fe9 sample does not exhibit SPR structure as expected, considering that the frequency of the resonance is located in the UV region [142], and that the resonance is strongly damped in interband excitations involving 3d electrons [143], [144]. Neither the spectrum of the as-implanted Au9Fe9 presents the SPR peak even if these nanoparticles are richer in Au. In principle the attenuation of the plasmon may be understood as arising from the 3d-4s (Fe) -5s (Au) hybridization as result of the alloying of both metals. In Au3Fe3, however, a broad peak (inset in figure 5.17) around 500 nm is observed, indicating that in this case clusters of Au and Fe are growing separated in the silica matrix, instead of Au-Fe nanoparticles. This is a clear indication that the the nanostructure in the low dose sample is quite different from the one found in the high dose sample (Au9Fe9) as evidenced in the previous paragraph.

The magnetic measurements (figure 5.18) made in the Fe9, Au9Fe9 and two Au3Fe3 samples (one as-implanted and the other thermally annealed at 600 °) indicate a reduction of the magnetic moment of the samples containing gold with respect to the pure iron nanoparticles: $0.3\mu_B$/Fe atom in Au3Fe3 and $1.5\mu_B$/Fe atom in Au9Fe9 compared to $1.8\mu_B$/Fe atom in the Fe9 sample. Furthermore, this moment per atom is much smaller than the bulk value of $2.2\mu_B$/Fe atom. This last fact gives support to the previous compositional analysis pointing to the presence of

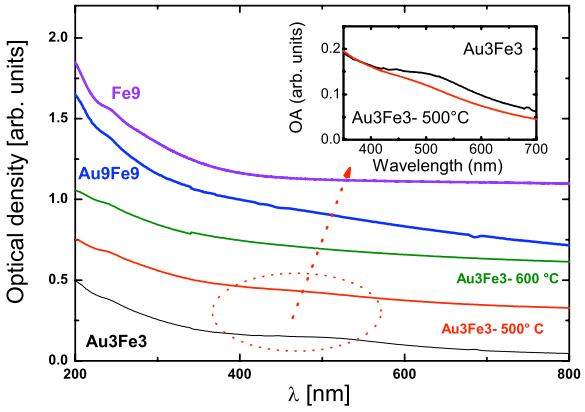

(a) UV-Vis optical absorption spectra of the Au9Fe9, Fe9 and Au3Fe3 (as-implanted and thermally annealed at 500° and 600° C). The inset shows the suppression of the plasmonic resonance after thermal treatment of the Au3Fe3 sample evidencing the formation of a AuFe alloy. The spectra were taken at room temperature.

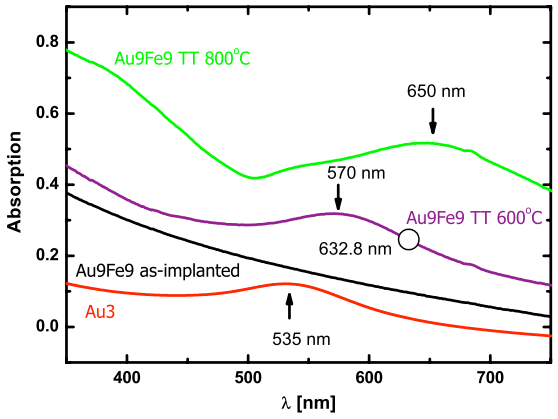

(b) Detail of the UV-Vis optical absorption spectra of the Au9Fe9 samples, as-implanted and thermally annealed at 600° and 800° C). The spectrum of Au3 is shown for comparison. The spectra were taken at room temperature.

Figure 5.17: UV-Vis optical absorption spectra of the Au-Fe series of samples.

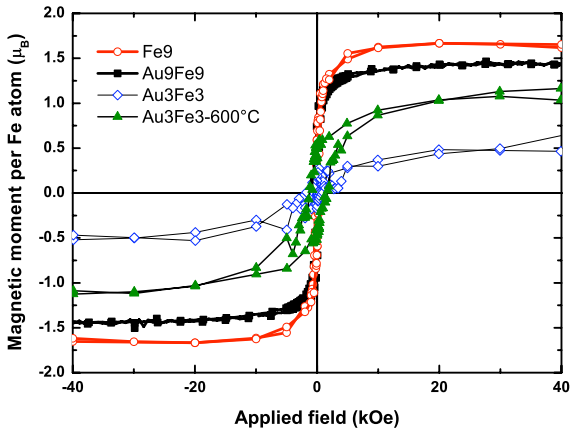

Figure 5.18: Hysteresis loops of the ion implanted AuFe samples measured in a SQUID magnetometer at 3K.

iron oxides in the samples. X-Ray Circular Magnetic Dichroism (XMCD) measurements give further support to this observation [53]. This high sensitivity technique has the advantage of element-specific selectivity, allowing in this case the determination of the XMCD of one of the components of the solid solution. The measurements were done with X-rays with energies around L2-L3 edges of gold (13.75 and 11.92 keV, respectively). XMCD of the Au9Fe9 sample at the L3 edge displayed a strong polarization of the gold, which is ferromagnetically coupled to the iron magnetic moments. Similar effects of magnetic polarization of otherwise non-magnetic metals have been reported before, for interfaces [145] and nanoparticles [140]. On the other hand, the Au3Fe3 sample displayed XMCD at the L3 edge 1 order of magnitude smaller than the Au9Fe9 sample, indicating a small degree of mixing between these two elements in this low dose sample, besides the already mentioned presence of separated Au and Fe nanoparticles. The small magnetic moment per Fe atom measured in this case could be related to the oxidation of the Fe nanoparticles. On the other hand, the Au3Fe3 sample annealed in reducing atmosphere at 500° displays an increase in magnetic moment with respect to its as-implanted counterpart. The fact that the band corresponding to the surface plasmon resonance disappears from the optical absorption spectrum of this sample (figure 5.17) suggests that the annealing process in this case is leading to an enhanced mixing of Au and Fe, just like in the Au9Fe9 case.

The presence of this magnetic polarization of gold in the alloys could be expected to give rise to interesting effects, such as enhanced MO response and enhanced magnetic anisotropy. The

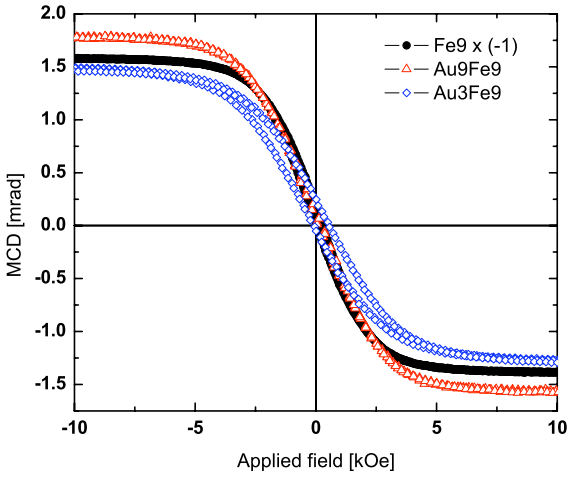

Figure 5.19: MCD hysteresis loops of the as-implanted Fe9, Au3Fe9 and Au9Fe9 samples. The measurements were performed with 632.8 nm light and at 1.5K. The Fe9 curve is represented with an inverted sign for better comparison.

magnetic measurements (figure 5.18) do not give support to the later case. They roughly yield the same coercive field for both Fe9 and Au9Fe9. Furthermore, the effective anisotropy constant $K_{eff}(\langle T_B \rangle)$ at the average blocking temperature, that may be derived from the temperature dependence of the zero-field cooled and the field-cooled magnetization, decreases from 6.1x10^5 J/m^3 in Fe9 to 1.3x10^5 J/m^3 in Au9Fe9. This is calculated substituting the average particle volume $\langle V \rangle = \pi/6\langle D_{XRD} \rangle^3$ ($\langle D_{XRD} \rangle$ is the average particle diameter from the XRD data) in the equation for the blocking temperature $T_B = K_{eff}V/25k$ (for SQUID measurement timescales). A drawback in this interpretation of the data is the broad size distribution in the Au9Fe9 sample. The presence of large ($D \sim 20nm$) particles with smaller effective anisotropy constants could cause the decrease in the value of $\langle K_{eff} \rangle$.

In order to verify the first possibility, namely enhanced MO response, MCD measurements were performed in the Fe9, Au3Fe9 and Au9Fe9 samples (this last one as-implanted, and annealed at 600 and 800 degrees), employing several wavelengths and at 1.5K. The results are shown in figure 5.20 for Au9Fe9 and Fe9 with 632.8 nm. The data present much better SNR compared to the magnetic measurements of figure 5.18. The increase in saturation MCD of 22% that results from the presence of gold in Au9Fe9, with respect to Fe9, is evident, while the coercive field does not suffer major changes. Furthermore, the presence of Au induces a sign

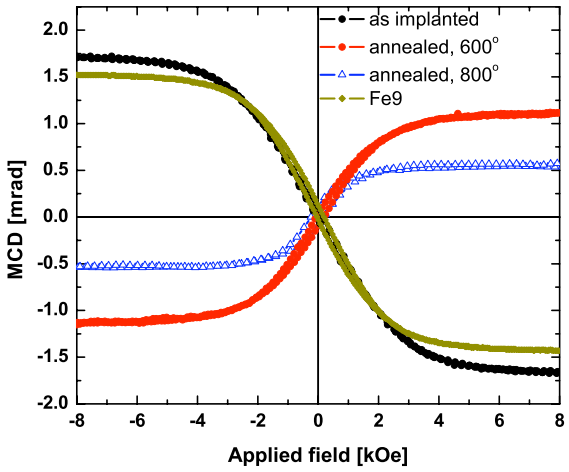

Figure 5.20: MCD hysteresis loops of the Au9Fe9 as-implanted and annealed (at 600 and 800 degrees during 1 hour) samples. The Fe9 curve is also shown, with inverted sign for better comparison. The measurements were performed with 632.8 nm light and at 1.5K.

change in the MCD at this wavelength (the Fe9 curve has been inverted in this figure to make the comparison with the Au9Fe9 curves easier). Such sign changes have already been reported for YIG samples doped with Au nanoparticles ([146]) and the proposed hypothesis is that they might be connected to local electric field enhancements due to the surface plasmon resonance of the Au particles, as well as to modifications in the effective spin-orbit coupling induced by these strong optical near-fields. Further comparison of these measurements with the Au3Fe9 result (figure 5.19) indicates that this last sample displays a significant increase in coercivity, while its dichroism is slightly reduced with respect to Fe9. The coercivity goes from around 150 Oe in the pure Fe sample (Fe9) to 310 Oe in the Au3Fe9 and down to 90 Oe in the Au9Fe9. So, a small amount of gold in the alloy can increase the anisotropy, as seen from the increase in coercivity of the Au3Fe9, while producing a small decrease in dichroism. On the other hand, larger amounts of gold will only produce a small enhancement in saturation dichroism for these samples. But as seen in the previous section, MCD measurements of hysteresis cycles of alloy nanoparticles yield wavelength-dependent coercivity values that do not correspond to the ones determined by magnetometric methods.

In order to verify if this effect is present in the Au-Fe nanoparticles, MCD hysteresis loops

of these samples were measured at several available wavelengths at 1.5 K. The MCD hysteresis cycles of the as-implanted Au9Fe9 are shown in Figure 5.21, Fe9 is shown in Figure 5.22, and the annealed Au9Fe9 are in Figures 5.23 and 5.24 for 600° and 800°, respectively. Figure 5.25 shows the absolute values of saturation MCD (MCD at 2 T) plotted against the measurement wavelength for all these curves. We can see that the gold-containing samples present sign changes for some wavelengths while the Fe9 MCD curves always have the same sign, as pointed out in the previous paragraph. Furthermore, while the as-implanted Au9Fe9 and the Fe9 samples have very small and virtually wavelength independent coercivities, the annealed samples display increased and wavelength dependent coercivities. This last fact is in contrast with the absence of the effect in the as-implanted Au9Fe9, pointing out to subtle modifications in the structure of this alloy during thermal annealing that give rise to an increased magnetic anisotropy (larger H_c) and to the surface plasmon resonance (see figure 5.17). The presence of a wavelength dependent coercivity in samples in which the plasmonic resonance is present is in complete agreement with the conclusions drawn from the analysis of the magneto-optical measurements on the $Co_{33}Ni_{67}$ presented in the previous section. Further agreement is found in the behavior of the coercivity in function of wavelength. For $Co_{33}Ni_{67}$, with a surface plasmon resonance at around 350 nm, H_c decreases monotonically as the measurement wavelength gets closer to this value, but as it is located in the UV region and our available light sources did not allow measurements to be done in this part of the spectrum, the hypothesis of a minimum in H_c vs λ when $\lambda \sim \lambda_p$ could not be verified in that case. Annealed Au9Fe9 samples, however, have surface plasmon resonances located in the visible (570 nm for Au9Fe9 annealed at 600° and 650 nm for the sample annealed at 800°) range. Values of the coercive field can then be determined on both sides of the resonance. The results are shown in figure 5.26. It is clear that, as previously suggested by the wavelength dependence of the coercivity of $Co_{33}Ni_{67}$, the coercivity decreases as the probe light wavelength gets near the plasmon resonance wavelength, increasing in other regions of the spectrum.

5.3 Conclusions

Magneto-optical methods are a very attractive way to study the magnetism of nanostructures, due to their high sensitivity and simplicity of implementation. But care should be taken in certain cases, as the interaction between light and the structure being investigated can produce changes in its electronic structure that may lead to major changes in its magnetic properties. The MCD measurement of hysteresis cycles and ac susceptibility in a family of Co-Ni alloy nanoparticles

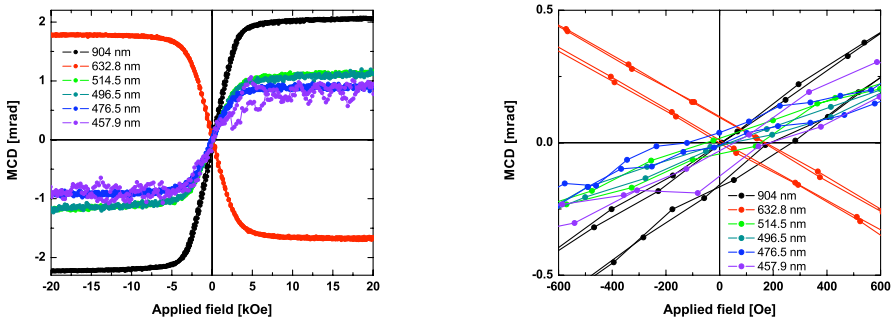

(a) MCD hysteresis cycles of the as-implanted Au9Fe9 sample for several wavelengths.

(b) Enlarged part of the graphics corresponding to the coercive fields.

Figure 5.21: MCD hysteresis cycles of the as-implanted Au9Fe9 sample, with several wavelengths from the NIR to visible.

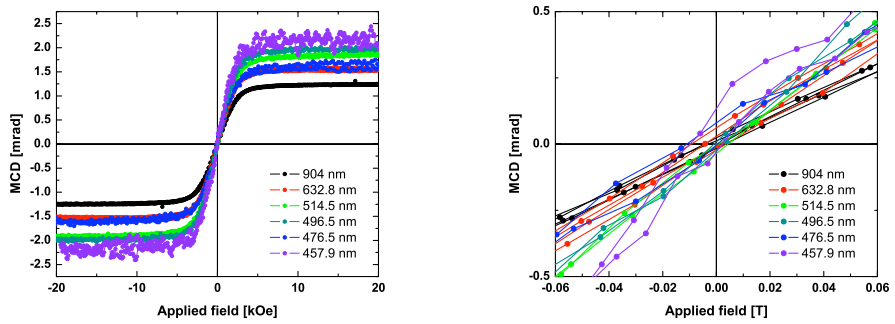

(a) MCD hysteresis cycles of the as-implanted Fe9 sample for several wavelengths.

(b) Enlarged part of the graphics corresponding to the coercive fields.

Figure 5.22: MCD hysteresis cycles of the as-implanted Fe9 sample, with several wavelengths from the NIR to visible.

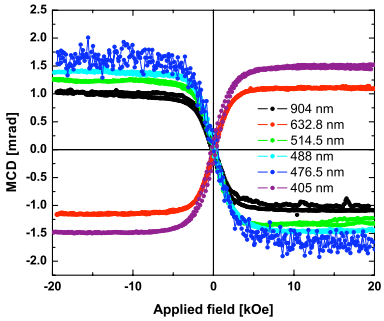

(a) MCD hysteresis cycles of the Au9Fe9 sample thermally annealed at 600° for several wavelengths.

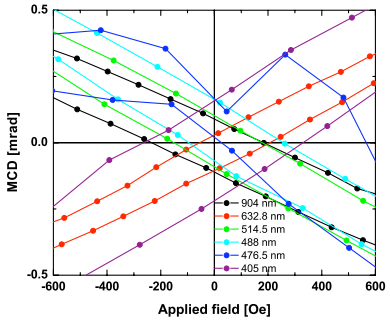

(b) Enlarged part of the graphics corresponding to the coercive fields.

Figure 5.23: MCD hysteresis cycles of the Au9Fe9-600 sample (thermally annealed at 600° in reducing atmosphere during 1 hour), with several wavelengths from the NIR to visible.

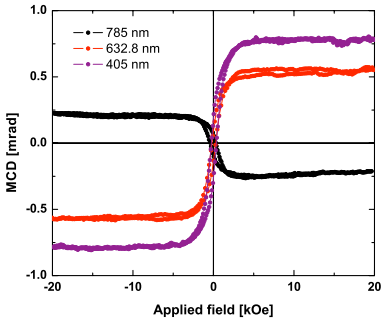

(a) MCD hysteresis cycles of the Au9Fe9 sample thermally annealed at 800° for several wavelengths.

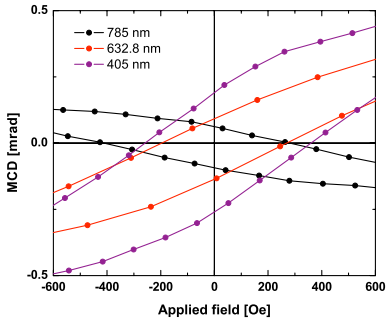

(b) Enlarged part of the graphics corresponding to the coercive fields.

Figure 5.24: MCD hysteresis cycles of the Au9Fe9-800 sample (thermally annealed at 800° in reducing atmosphere during 1 hour), with several wavelengths from the NIR to visible.

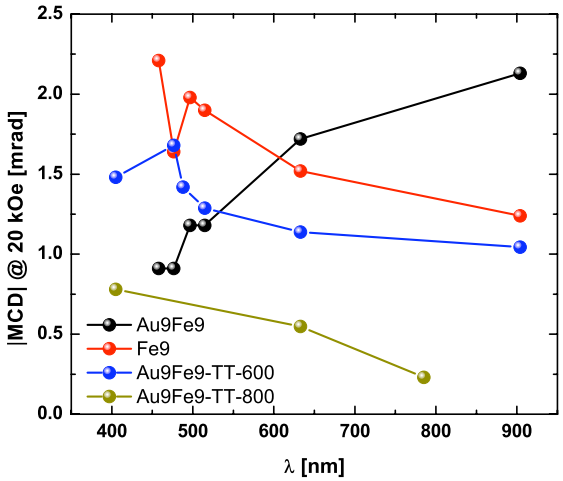

Figure 5.25: Saturation MCD values, taken at 2T, for the as-implanted Fe9 and Au9Fe9 samples, and the Au9Fe9 annealed samples, at several wavelengths. Values taken from 5.21, 5.22, 5.23 and 5.24.

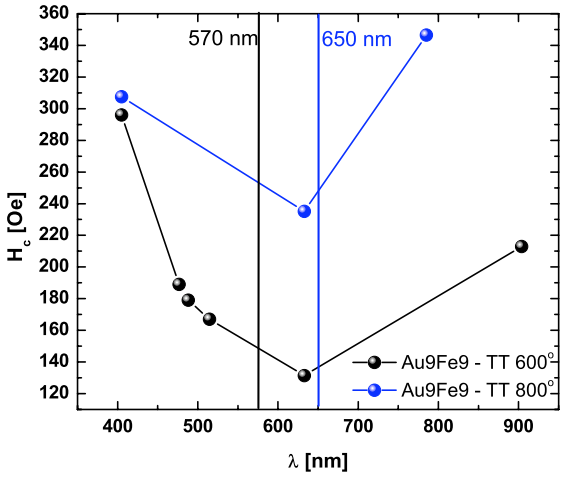

Figure 5.26: The wavelength dependence of the coercivities of the thermally annealed Au9Fe9 samples. The vertical lines indicate the wavelength of the surface plasmon resonances of both samples, taken from the UV-Vis absorption spectra in 5.17.

embedded in a silica matrix demonstrates this fact. The probe light in this case was inducing, through the surface plasmon resonance, major changes in magnetization relaxation of the $Co_{33}Ni_{67}$ samples leading to an enhancement of the magnetic coercivity of this material. The same effect was verified in a series of Au-Fe nanoparticles, in which the degree of mixing of both metals and the percentage of gold in the alloy as controlled by a suitable thermal annealing, determine if the effect is present or not. In contrast to the $Co_{33}Ni_{67}$ case, the effect in AuFe nanoparticles is due to the surface plasmon resonance of the Au atoms, that are non magnetic. Further understanding and control of this process could have interesting applications, for example in magnetic photoswitchable devices or in devices whose magnetic character can be changed from hard (high H_c) to soft (small H_c) by means of light irradiation.

6 Magneto-optical studies of SMM-doped polymers and monolayers

In this chapter the MO measurements of Mn12 and Fe4 embedded in non crystalline environments such as polymers, Langmuir-Blodgett films and self-assembled monolayers on Au surfaces will be presented. Emphasis will be given to the MO study of Langmuir-Blodgett films of the Mn12Bz derivative [10] as part of a greater characterization effort of Mn12 derivatives in different non-crystalline environments that was going on when I started my thesis work [30], and to the studies of Fe4 derivatives doped in transparent polymers and on Au surfaces.

6.1 The Mn12 cluster in non-crystalline environments

The Mn12 cluster, as the archetypal SMM, has been extensively studied in different non-crystalline environments, in order to address its magnetism in conditions closer to the ones found in spintronic devices. The ultimate goal is to achieve the addressing of the magnetization of a very reduced number of clusters using our MCD magnetometer [30], a step necessary to characterize monolayers of Mn12 SMMs on Au surfaces.

The cluster was included in three types of non-crystalline environments: transparent polymers (PDMS - Poly(dimethylsiloxane) and PMMA - Poly(methyl methacrylate)) that are an amorphous 3D host matrix in which the clusters are randomly oriented and far from each other so that intercluster interaction effects may be ignored; Langmuir-Blodgett (LB) films with a number of layers of the order of 60; and self-assembled monolayers (SAMs) on Au surfaces. It is clear that from the first to the last case the dimensionality was reduced from 3 to 2 dimensions, with the LB films representing an intermediate step. The preparation of the three samples will be presented in the following subsection.

6.1.1 The preparation of the samples

Mn12 in polymers

The Mn12 derivative used in this case is the pivalate ($Mn_{12}O_{12}$(t-BuCOO)$_{16}(H_2O)_4$, herein called Mn12piv), due to the ease of inclusion in the polymers offered by this choice of ligand. The Mn12piv polycrystalline powder is diluted in a suitable solvent, dichloromethane in this case, and the resulting solution is mixed with the polymer precursor, in case the PDMS (polydimethylsiloxane, Sylgard Silicone Elastomer) is used, or with the polymer diluted in dichloromethane, in case the PMMA (poly(methyl methacrylate)) is used. During this process the masses of Mn12piv and of the polymer must be carefully determined in order to obtain a final sample of know concentration. After careful mixing of Mn12 solution and polymer, the final solution must be cast in an appropriate template. A small PVC box with very smooth surfaces was used to prepare the PDMS samples, while the PMMA samples were casted on stretched polyethylene films. The PDMS in general solidifies forming a soft transparent thick block, slightly brown in color (this depends on the Mn12 concentration), that can be cut into smaller pieces, more convenient for the MCD measurement. The PMMA solidifies in films approximately 20μm thick. It is important that the solidification process is not conducted at high temperatures (in an oven, for example), because it was observed that in this case the final sample showed no hysteretic behavior, indicating that the high temperatures that accelerate the solidification process also damage the Mn12 clusters. In both cases it is assumed that all the solvent evaporates during the casting process. Several concentrations ranging from 10^{-5} M to 10^{-2} M may be achieved.

Optical absorption measurements (UV-Vis) were made in order to ascertain the presence of Mn12piv in the polymer. The characteristic spectrum of Mn12 is observed in the solution (figure 6.1) as well as in the polymer spectra. Magnetic measurements may also be use in order to verify the successful inclusion of these clusters in the polymers. For the Mn12, a M vs. H measurement performed in a VSM magnetometer at low enough temperatures (1.5K) will show the typical "butterfly" hysteresis curve (explained in subsection 6.1.2), characteristic of this compound. The Fe4, however, is paramagnetic within this temperature range, and the available SQUID or VSM magnetometers cannot go below 1.5K. The solution is to perform an AC-susceptibility measurement in a wide frequency range and observe the presence of the frequency dependent χ'' vs. T peaks at the temperatures characteristic of this compound.

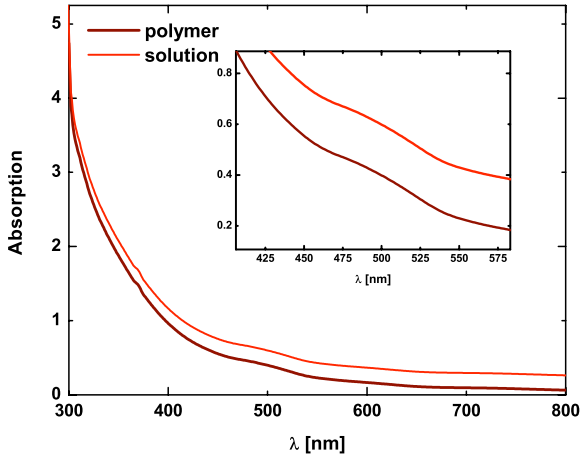

Figure 6.1: Optical absorption spectrum of the Mn12piv derivative in solution and in PMMA polymer. The inset shows the weak absorption band at around 500 nm.

Mn12 Langmuir-Blodgett Films

The Langmuir-Blodgett technique is an elegant approach to arrange organic molecules in well organized monolayers or multilayered films, one layer at a time [147]. The method was first devised by Irvin Langmuir and Katherine B. Blodgett in the 1920's. The idea is to organize amphiphilic molecules, that is, molecules containing both a hydrophilic "head"and a hydrophobic "tail", on a water surface and transfer them layer by layer to a solid substrate by dipping it into this surface. Multiple dippings transfer multiple layers. The process is carried on in a special device, the Langmuir-Blodgett trough.

The film fabrication is a two-step process. The first step is the formation of a monolayer of organic molecules at the gas[1]-water interface (a Langmuir monolayer). The tensioactive molecules dissolved in the organic solution organize along the interface, with the polar parts attracted to the water while their hydrophobic tails limit the dissolution into the aqueous subphase (figure 6.2). At this stage, the molecules are poorly organized (a large area/molecule). Larger organization and an increased molecular density are achieved through the slow compression of the monolayer by means of a barrier mechanism in the LB trough. In figure 6.3 **A** represents the initial state with a low level of molecular organization on the surface; **B** represents the molecu-

[1]May be air, or other gas if the process is carried on in controlled atmosphere

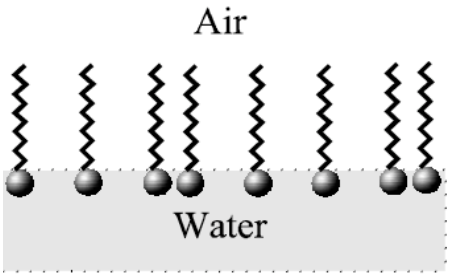

Figure 6.2: Schematic view of a Langmuir-Blodgett monolayer on a water surface. (From KSV Instruments Application Notes #107)

lar organization after the compression, with a greater packing. When this packing is sufficiently dense, the LB film deposition may be attempted by dipping a solid substrate into the gas-liquid interface. This results in the transfer of one monolayer. During the up-stroke, another monolayer is transferred. During this process the feedback mechanism of the LB trough monitors the surface pressure, keeping it constant by moving the barriers. Multilayers can be built-up this way, normally with successive layers oriented in an alternating way ("head-to-head"and "tail-to-tail"bilayers), forming what is called a Y-type film. This is schematized in figure 6.5, together with the other types of films that can be produced with this technique. By using charged molecules to form the monolayer, metal or molecular ions can be incorporated in the transferred film in what is called the "semi-amphiphilic strategy".

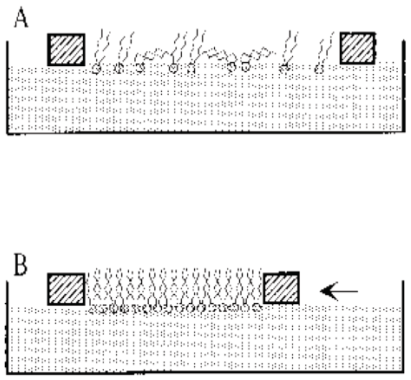

Figure 6.3: The Langmuir film on the air-liquid interface before and after compression.

A similar approach was used to prepare the multilayered LB films containing the Mn12 clus-

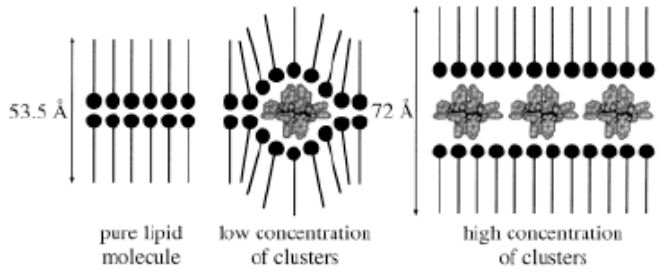

Figure 6.4: Schemes of the Y-type LB films of Mn12Bz and behenic acid for three different ranges of the lipid:cluster ratio. From [10]

ter. But in this case, as the cluster is electrically neutral (and does not form Langmuir monolayers by itself) a mixture of the clusters and a lipid is used to form the Langmuir monolayer prior to the transfer. The lipid used was behenic acid ($CH_3(CH_2)_{20}COOH$), that together with the benzoate derivative of the Mn12 cluster forms a Langmuir monolayer that can be successfully transferred to quartz slabs. The Langmuir film is stable only for high lipid:cluster ratios (5 or higher), and its deposition onto the substrate is achieved at a surface pressure of $30 mNm^{-1}$, forming a Y-type film [10]. The film's structure can be verified with X-ray diffraction, confirming that monolayers of Mn12Bz with periodicity of 72 ± 2 Å are formed for lipid:cluster ratios between 10:1 and 5:1. This periodicity corresponds to the intercalation of a layer on Mn12Bz with their axial directions oriented preferably perpendicular to the film plane, between two layers of behenic acid (figure 6.4). The samples used in this work were prepared by M. Clemente-León, from the University of Valencia [10] and contained 58 layers (29 on each side of the quartz slab, 418 nm total thickness on both sides).

Mn12 Self-Assembled Monolayers

The magnetic behavior of monolayers of the Mn12 cluster was analyzed using our MO magnetometer and samples prepared by the self-assembly method. The sample preparation was carried out by other members of the group ([148], [11]), and will be only briefly outlined in the following paragraphs. It has been known since 1983 [149] that aliphatic thiols have a tendency to spontaneously form ordered bidimensional structures on gold surfaces. This phenomenon can be exploited to prepare ordered monolayers of molecules with minimal previous substrate treatment and no operator intervention during the process, the only requirement being that these

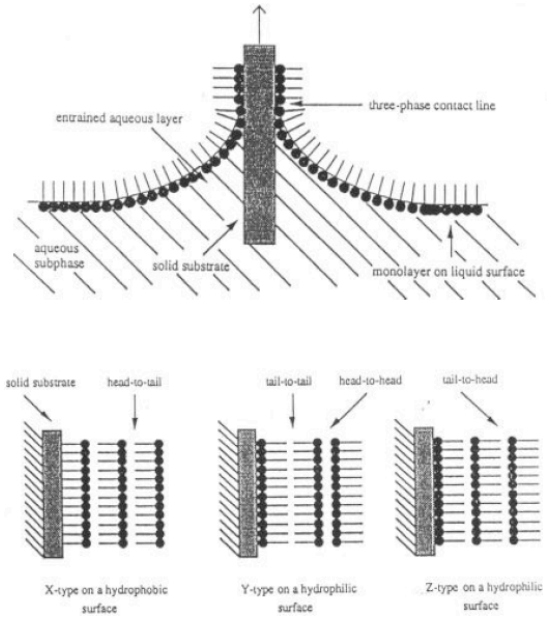

Figure 6.5: The process of preparing a LB film. On the upper part, the transfer of a floating monolayer to a solid substrate is shown. On the lower part, the different kinds of films that can be produced by this process.

molecules must contain a surface binding group. The adsorption of the molecule on the surface is driven by the strong S-Au interaction. This can be achieved, as in our case, by a ligand substitution reaction in which the ligand present in the original cluster (Mn12Ac, but also Mn12Bz and Mn12piv) is replaced by one containing the necessary binding group.

In this case, the ligand employed is the 4-(methylthio)benzoic acid, containing a protected thiol and an aromatic group (herein denoted by PhSMe, the structure of this derivative may be seen in figure 2.7, subsection 2.3.1). This choice reflects the superior redox stability of the Mn12 with respect to the protected thiol ([148] and references therein). As there are 16 of these ligands surrounding the Mn12 core, the molecules may bind in several orientations, with no preferential direction, resulting in a random distribution of easy-axes (isotropic). The substrates were commercial 200 nm gold films evaporated on mica, treated by flame annealing in order to reduce the otherwise large surface disorder. The deposition is achieved by leaving the substrate (that has been thoroughly cleaned in ultrasound first with a tensioactive, then with methanol and finally with dichloromethane) in a solution of the Mn12PhSMe derivative in dichloromethane during 30 minutes after which it must be rinsed in fresh dichloromethane in order to remove

non-bound molecules. The process must be carried out in a glove box in order to minimize atmospheric contamination. The presence of the Mn12 derivative is confirmed by XPS analysis and STM scans show a uniform coverage of non-aggregated objects with diameters of the order of 2.7 ± 0.5 nm (figure 6.6), a number in good agreement with the crystallographic dimensions of the complex (2.8 x 2.1 nm), and surface density of 0.2 units/nm^2.

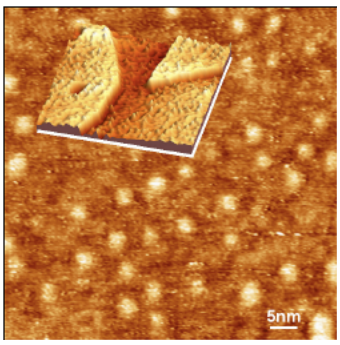

Figure 6.6: Constant current STM image of Mn12PhSMe on a Au(111) surface (The inset shows a 200 x 200 nm^2 constant current STM image of this sample, showing the triangular terrace features of these substrates after flame annealing). From [11].

6.1.2 Magnetic and Magneto-Optical Measurements

The investigation of Mn12 SMMs in non-crystalline environments were conducted with derivatives of the Mn12Ac cluster included in PDMS, a Langmuir-Blodgett film and monolayers prepared according to the methods explained in the previous section. These studies were important as they led to a deeper understanding of the magnetic behavior of this molecular magnet in environments more similar to the ones that may possibly be found in spintronic devices, magnetic data storage devices, and other applications in which these molecules are not found in a crystalline form. As the concentrations of clusters in these cases are very small, frequently the lower detection limit of SQUID magnetometers is reached and so very high sensitive alternative methods are needed. The MCD measurement setup schematized in chapter 4 proved to be a very useful tool, both because of its sensitivity, enough to detect monolayers of Mn12, and to its relative instrumental simplicity.

It is important to stress that the optical quality of the samples must be very good in order to ensure the that the measurement will be successful. By optical quality I mean a good smooth surface that will not cause light scattering, good transparency and the absence of aggregates

inside the sample. While MO measurements are sensitive to ensembles of isolated molecules, aggregates scatter the light, causing loss of sensitivity. For the preparation of LB films, the benzoate derivative (Mn12Bz) was used, for reasons explained in the previous section. And finally for the preparation of SAMs a derivative containing a protected thiol group (Mn12PhSMe) was used. First of all, in order to rule out possibly different magnetic behaviors arising from the different substituent ligands employed, magnetic measurements were performed in a VSM magnetometer, at a 1T/min[2] sweep rate [3], for samples of the 3 derivatives in PDMS. The results are shown in figure 6.7, and we can see that the three derivatives roughly display the same magnetic behavior regardless of the substituent ligand used. Hysteretic behavior is observed at 1.6K, with the following coercive fields: 2.2 kOe, 2.4 kOe and 2.6 kOe for piv, the bz and the PhSMe respectively.

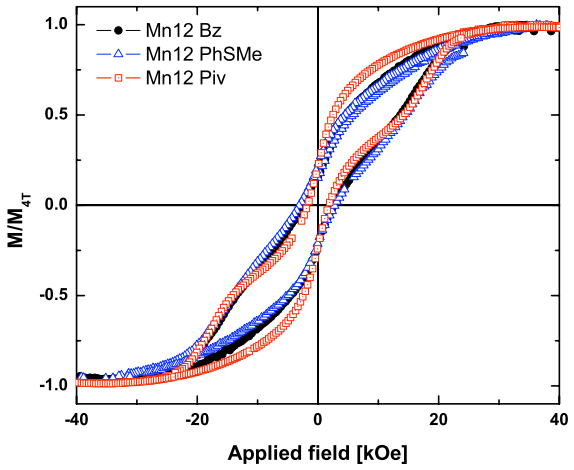

Figure 6.7: Hysteresis cycles of the pivalate, benzoate and PhSMe Mn12 derivatives, measured with a VSM at 1.6K. The sweep rate employed was 1T/min.

These coercive fields are much smaller than in the crystalline phase, but the slow relaxation of the magnetization still persists at these temperatures (1.45 K for the benzoate and the thioether, 1.6 K for the pivalate). The hysteresis curve displays the "butterfly"shape, characteristic of the fast relaxation at zero field due to the quantum tunneling of the magnetization [10],[39] in an ensemble of Mn12 clusters with randomly oriented easy axes. In order to investigate the behav-

[2] 1 T = 10 kOe

[3] The same sweep rate used in the magneto-optical measurements

ior of these clusters in the other samples (LB film and SAM), the MCD magnetometer shown in chapter 4 was employed. Multiple samples can be attached to the sample holder using copper adhesive tape. Low temperatures in the sample space are reached by cooling with a flow of He from the superconducting magnet He bath. In order to reach the lowest measurement temperature (1.5K) the needle valve must be open while the sample space is pumped. The cooling rate may be controlled by means of the needle valve aperture. When liquid He starts to accumulate inside the sample space ($T \sim 4.2K$) the needle valve must be completely closed while still pumping the bath, so that the temperature goes down to 1.5K. For the measurements presented here the samples were cooled in zero-field at a rate of approximately 10K/min. The resultant data are shown in figure 6.9 together with the magnetic measurements for better comparison. All data were taken with 632.8 nm light and a 1T/min sweep rate. The two samples of Mn12piv in PDMS display the same behavior as in the magnetic measurements, a "butterfly"-shaped hysteresis loop and small coercivity compared to the bulk (in this case a crystal powder, with $H_c = 8.5$ kOe at 1.85 K). The coercivities found were 3.2 kOe for the less concentrated sample (1x10^{-5} M) at 1.65 K and 6.2 kOe for the more concentrated sample (1.3x10^{-4} M) at 1.45 K. The same Mn12 derivative was also included in a thin sheet of PMMA (poly-methyl methacrylate) and its hysteresis cycle was measured with 476.5 nm light, yielding a coercivity value of 2.5 kOe, in agreement with the previous results for PDMS. Small differences with respect to the coercivities measured with the VSM technique are ascribed to optical effects characteristic of the MCD measurement process [69]. The electronic dipole transition moments associated to magnetic circular dichroism are highly polarized with respect to the molecular reference frame and the energy of the transition. This results in an inherent capacity of selection of cluster orientations by this technique. In an anisotropic sample where the clusters are randomly oriented this will cause the selection of a subset of the clusters with orientations within the band characteristic of that transition energy (correspondent to the photon energy) while clusters with other orientations not contributing to the MCD.

Going back to the data, the optical path of the light beam through the low concentration sample is about 0.5 mm long, and the beam spot area is 0.03 mm^2 (for a beam diameter of 200μm). Considering the concentration of 1x10^{-5} M the number of clusters probed by the beam in these conditions would be approximately equal to 3.61x10^{11} (2x10^{-11} mol/mm^2 times the beam spot area times the Avogadro number). The saturation MCD (MCD at an applied field of 40 kOe) of this sample (see figure 6.9) is equal to 420 ± 20 μrad which is about 70 times greater than the instrumental sensitivity and yields the MCD value of 1.16x10^{-15} rad/cluster for this molecule.

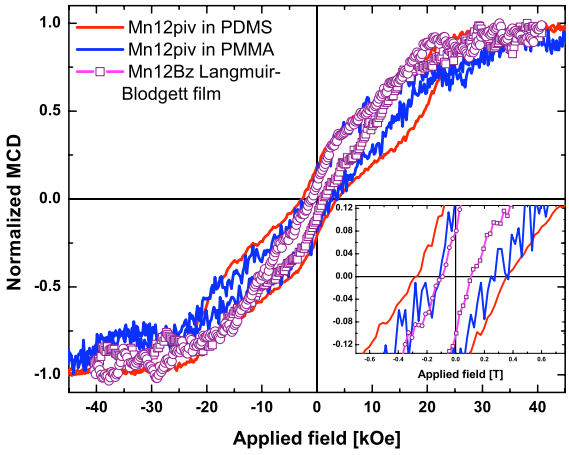

Figure 6.8: MCD hysteresis loops of the Mn12piv derivative embedded in PDMS and PMMA, and in a Langmuir-Blodgett film, measured at 1.5K. The inset is an enlargement of the coercive field zone.

After characterizing the polymeric solutions we measured MCD magnetization curves of the 58 layers Langmuir-Blodgett film of Mn12Bz. The result is shown in figure 6.9 (the blue curve on the lower panel). The cluster still displays hysteretic behavior, with the characteristic shape, but the coercive field is much lower, 1.2 kOe with respect to the polymeric solutions. This value is, however, in very good agreement with previously reported magnetic measurements of a sample with 300 layers [10] [4] that had $H_C = 1.0$ kOe and displayed the same hysteresis loop shape. This leads us to conclude that the 2D environment imposed to the Mn12 cluster in the LB film significantly modifies its magnetization dynamics, while different numbers of layers do not influence it, supporting the fact that there are no inter-layer interactions in these structures (the separation between two layers of Mn12 is of the order of 60 Å, so dipolar interactions are not important in this case, being or the order of 0.6 μeV). For further comparison, these data are plotted in figure 6.8 together with two hysteresis loops of the Mn12piv derivative included in PDMS and PMMA polymers. The saturation MCD value of the LB sample is equal to 450 ± 30 μrad. Given the approximate diameter of the Mn12Bz cluster, 2.3 nm, the density of clusters in a single LB layer is approximately 3.7x10^{-13} mol/mm^2. Crossing 58 layers the beam will "see"a

[4] The small number of layers (58) in our LB sample made magnetization measurements with a SQUID magnetometer impossible.

density of 2.2x10^{-11} mol/mm^2. From the previously obtained saturation MCD per cluster of 1.16x10^{-15} rad, we can then estimate the saturation MCD value for this sample at 460 μrad, in excellent agreement with the measured value.

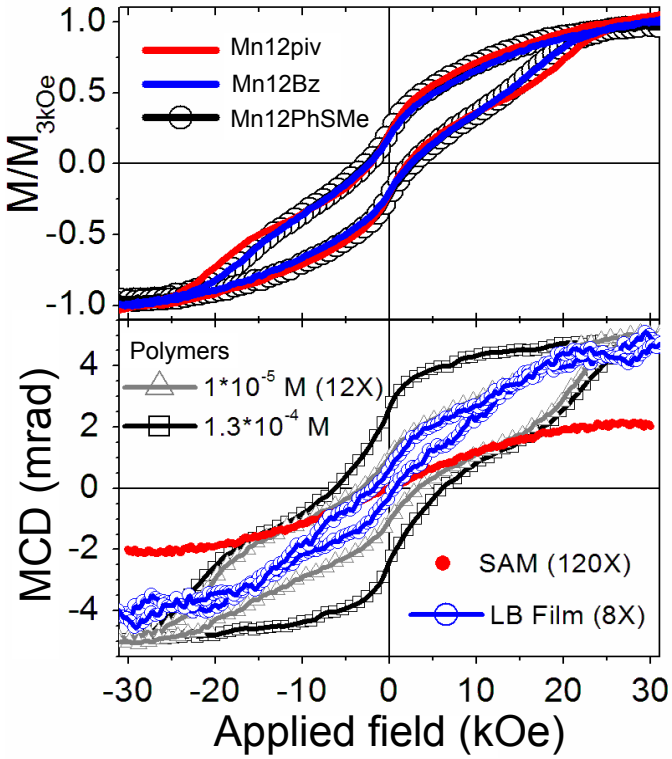

Figure 6.9: Magnetometric and MCD hysteresis cycles of the Mn12 derivatives (benzoate, pivalate and PhSMe) in different environments. The upper panel displays the magnetometric data from figure 6.7 For better comparison. The lower panel shows the MCD measurements of this molecular magnet in polymeric matrices, a Langmuir-Blodgett film and a self-assembled monolayer. The MCD measurements were made with 632.8 nm light. The temperatures are reported in the text.

The last step in our investigation of the magnetic behavior of the Mn12 cluster in different environments involved the MCD measurements of a self-assembled monolayer of Mn12PhSMe. The preparation of this sample was described in subsection 6.1.1. The preparation of addressable monolayers of magnetic clusters constitute a very important research goal, as it is a possible path to a next generation of magnetic storage devices. From the average diameter of the Mn12PhSMe cluster (determined from STM images, [148], [11]), 2.7 nm, the surface density is estimated

to be 2.8x10^{-13} mol/mm^2 corresponding to a saturation signal of 5.9 μrad. This lies at our instrument's sensitivity limit, so in order to make a reasonable measurement possible 5 samples were stacked on each other prior to a measurement, for an expected saturation MCD of 5x5.9 = 29.5 μrad for full monolayer coverage. The resultant curve is shown in figure 6.9. The observed saturation value is 21 μrad, indicating sub-monolayer coverage. This is in agreement with the aforementioned STM studies of these samples. The curve has no hysteresis, indicating that either the cluster has suffered chemical modifications that destroyed its magnetic behavior, or that the magnetization dynamics is greatly accelerated in these non-crystalline conditions. There is a clear trend in the reduction of the coercivity from the bulk polymeric solution to the LB film, ending up in the absence of hysteresis in the monolayer sample. A phenomenon that is believed to be responsible for the observed behavior is the presence of abnormally rotated Jahn-Teller axes in some of the Mn(III) ions of the Mn12 cluster. This has already been associated to the presence of fast relaxing and slow relaxing Mn12 isomers [150] and could be, in this case, the result of distortions of the magnetic core induced by the way the Mn12 interacts with the environment. Recent investigations, in which XAS (X-ray Absorption Spectroscopy) and XMCD (X-ray Circular Magnetic Dichroism) were employed to probe the magnetism and the electronic structure of Mn12PhSMe monolayers [151], however, point in a different direction. They indicate the presence of a high percentage of Mn(II) ions in the monolayers, pointing out a high degree of chemical reduction of the Mn12 cluster on a gold surface. This indicated that the cluster is too redox fragile and accepts extra electrons either from the gold substrate or generated during the grafting process. Furthermore, the XMCD studies confirmed the absence of hysteresis in these samples [151].

We have demonstrated that, for Mn12 derivatives, different ligands do not significantly influence its magnetic behavior, while the environment may induce drastic changes, to the point of making the hysteretic behavior characteristic of this magnetic cluster at low temperatures disappear. This last fact, the absence of hysteresis when the cluster is adsorbed on gold surfaces, drives us to look for another molecular magnet that is more suitable to these applications.

6.2 The Fe4 cluster in non-crystalline environments

The Fe4 cluster presents itself as an alternative to the Mn12 for studies of self-assembled monolayers, as it was demonstrated that this last loses its magnetic hysteresis when included in non-crystalline environments of experimental interest. It is a simpler cluster, and it has been recently demonstrated that it is both chemically and structurally more robust than Mn12, the only draw-

back still being its low blocking temperature, of the order of 500 mK. It is then mandatory the use of dilution refrigerators in order to study the hysteresis of this molecule. The studies presented in this section were performed at temperatures at which the spin relaxation in Fe4 is too fast and so it is paramagnetic, as our minimum working temperature is 1.45K. A computer program based on the model developed in chapter 3, section 3.3 was employed to fit the MCD magnetization curves of this paramagnetic state, in order to gain insight on the electronic transition dipole moments and polarizations of the optical transitions responsible for the magnetic circular dichroism observed in this cluster, that are readily accessible from the fitting procedure. Furthermore, zero-field parameters of the paramagnetic ground state (D, and the g factor of this cluster, normally accessible from EPR measurements) may also be obtained from these fit procedures.

6.2.1 The preparation of the samples

Fe4 in polymers

Essentially, the same methods previously used to prepare samples of Mn12 in polymers were used in this case. It was found out, though, that the stability of the Fe4 cluster in PMMA is poor over long periods of time, with the cluster breaking down into the dimer components. This is clearly seen as the color of the sample changes from yellow to pale orange. In this case polystyrene (PS) was also used, as it offered a stabler support to the Fe4 cluster.

Thin polymer films of Fe4Ph in PS (polystyrene) were also prepared by the dip coating method. This technique is used to produce thin films on substrates, and is in a certain way similar to the Langmuir-Blodgett technique. A substrate is carefully immersed in a solution (in our case polystyrene + Fe4Ph + dichloromethane) and withdrawn at a certain rate, allowing the deposition of a layer of the solution. The substrate must be extracted at constant velocity. The faster it is withdrawn, the thicker will be the resulting film. Ellipsometry characterization of our sample[5] indicates a thickness of 199.7 ± 0.1 nm with 4% unevenness.

Fe4 Self-Assembled Monolayers

The preparation of self-assembled monolayers of Fe4 followed the same method as for Mn12 described in subsection 6.1.1. The main differences are in the ligand used, and the resulting binding geometry of the cluster on the surface. The 6 methoxide bridging groups (OCH_3) of the original $Fe_4(OCH_3)_6(dpm)_6$ cluster were substituted by two tripod ligands C9SAc [44] (see

[5]Performed by Dr. Roberta Costanzo from Dipartimento di Chimica “G. Natta”, Politecnico di Milano

subsection 2.3.2 of chapter 2 for more details). This substitution leads to a Fe4 functionalized derivative with only two functional units (the binding part of the ligand) per molecule, oriented along its easy-axis of magnetization. This could lead in principle to an anisotropic distribution of molecule orientations in the adsorbate. The gold substrates in this case were left in dichloromethane solution during 20 hours and then rinsed in clean solvent. STM images confirm the presence of round objects with average diameter of 2.5 ± 0.1 nm (figure 6.10), in good agreement with the crystallographic figures. STM also suggests that the molecules are adsorbed in a *standing up* conformation, with only one extremity of the ligand binding to the surface and the other free. We do not believe that the observed round shape of the objects on the surface and the tight coverage achieved would be possible if the dominating conformation was a *lying down* one (*standing up* and *lying-down* conformations are depicted in figure 6.11), with both extremities of a molecule bound to the surface. Other techniques such as XPS and ToF-SIMS mass spectrometry gave further confirmation of the successful obtention of self-assembled monolayers of this cluster, this being the first time it has been achieved.

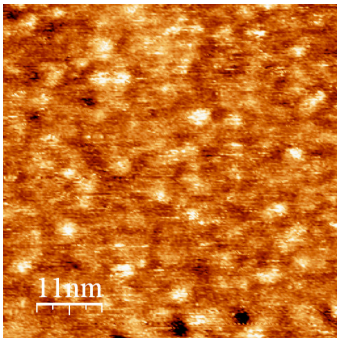

Figure 6.10: Constant current STM image of FeC9SAc on a Au(111) surface.

6.2.2 Magnetic and Magneto-Optical Measurements

The measurements of magnetization and MCD of the Fe4-C9SAc SMM in PMMA and PDMS polymers are shown in figures 6.12 and 6.13. The magneto-optical measurements were carried out with 476.5 nm light provided by an Ar:ion laser, which produces a fairly high saturation magnetic dichroism in this sample. Values as high as 4.5 mrad at 40 kOe were obtained with a high concentration (10^{-2} M) PDMS sample. A comparison between the MCD and the magnetic curves show that the paramagnetic character of the Fe4 cluster at this temperature is well

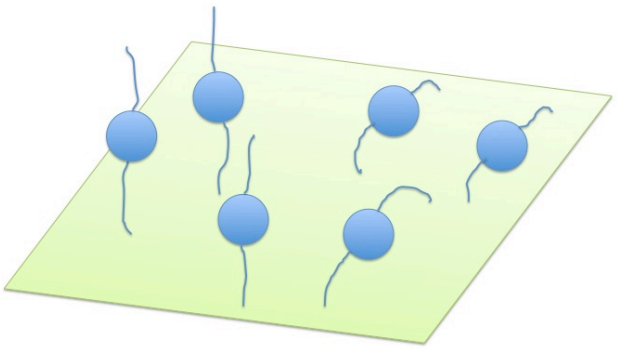

Figure 6.11: The two possible conformations of the Fe4C9SAc cluster on a gold surface, with the *standing-up* represented on the left and the *lying-down* on the right side.

reproduced, indicating a dominant C-term contribution to the dichroism. But there are qualitative differences between results from both methods: the MCD curves always reach saturation at lower fields with respect to the magnetization curves (figure 6.12). This different also present in the magnetometric measurements (figure 6.13). This puzzling observation led us to believe that the cluster orientations are not randomly distributed inside the PMMA polymeric matrix, but there is some kind of anisotropy in the molecular axis directions. Otherwise the PDMS and the PMMA curves would display the same behavior. The fact that the PDMS sample needs higher fields with respect to the PMMA sample in order to saturate suggests that in this last sample the easy axes are partially oriented perpendicular to the sample plane (the sample is a 20 μm thin film) and in consequence parallel to the applied magnetic field direction.

This may be the result of the PMMA casting process. As was explained in subsection 6.2.1 the PMMA sample is a thin transparent film, prepared by letting a drop of the PMMA + Fe4C9SAC + solvent solidify (by solvent evaporation) on a stretched polyethylene film. This partial orientation may then arise from the strain induced in the film by higher rates of solvent evaporation from the face of the film compared with that at the edges during evaporation of the solvent. The same phenomenon has been observed in samples prepared with polystyrene (PS), a polymer in which the Fe4 cluster is more stable over time. In fact, the PMMA sample's color went from yellow (the sample color as the solution of Fe4C9SAC or Fe4Ph) to orange over a few months

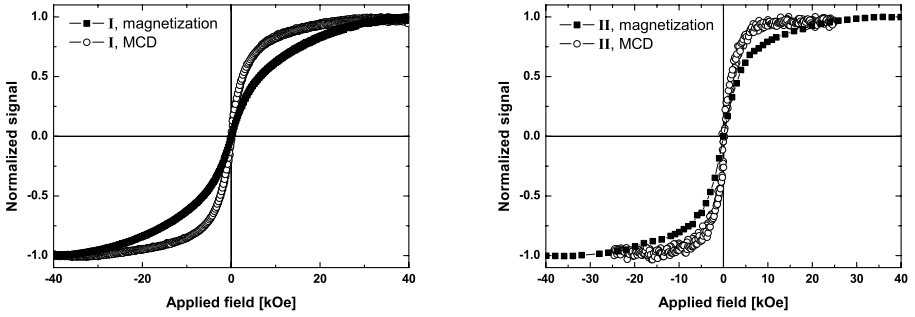

(a) PDMS (b) PMMA

Figure 6.12: Magnetic (M vs. H) and magneto-optical (MCD vs. H) measurements on the Fe4C9SAc cluster in PMMA and PDMS. The left-hand graph shows the PDMS data, and the right-hand graph shows the PMMA data.

time, while the samples prepared with PS showed superior stability. In order to confirm the partial orientation of the clusters in the thin polymeric samples, X-band EPR spectra were recorded for several angles between the magnetic field and the film plane (which we will call α), comprised in the 0 - 180 degrees interval. The initial position (0^o) corresponds to the magnetic field parallel to the sample plane. The spectra, recorded at 5K, are shown in figure 6.14.

The spectra consist of three transitions, two at approximately 330 Oe and 1580 Oe that show no angular dependence and one between 2120 and 2450 Oe showing angular dependence. A spectrum taken from a bulk (powder) sample of Fe4Ph is reported for comparison, as well as a simulated spectrum [6]. A good qualitative agreement between all these spectra is observed, indicating that the lines at the extrema of the spectra taken from the Fe4 in PS sample (the low field and the high field transitions) arise from transitions in the Fe4 $S = 5$ ground state multiplet. This confirms the presence of the intact cluster in these polymeric solutions. Further information regarding the levels involved in these transitions may not be obtained working with X-band EPR, as they correspond to an overlap of many transitions that may not be correctly assigned at this magnetic field range [153]. As the zero-field splitting in this cluster at this magnetic field range ($\sim$ 5000Oe) is much larger than the Zeeman splitting (in this case, the ZFS is about 10 times larger than the Zeeman splitting) these transitions may only be assigned at high frequencies (high field EPR) [119],[153], but the angular dependence strongly supports the partial orientation of

[6] Simulation done with the software package SIM by H. Weihe, [152]

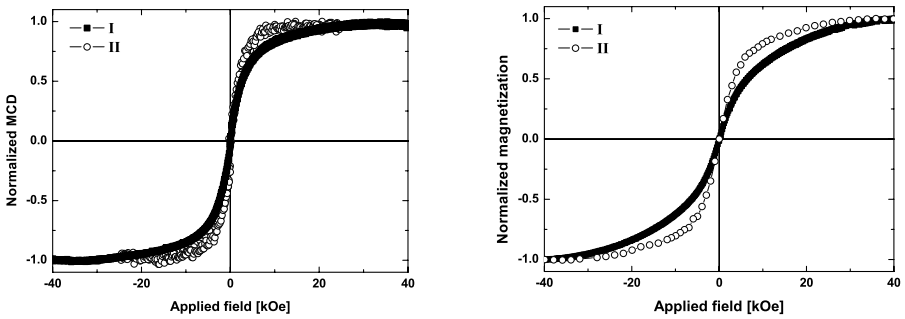

(a) Normalized MCD of the Fe4C9SAc in PMMA and PDMS.

(b) Normalized magnetization of the Fe4C9SAc.

Figure 6.13: Normalized MCD and magnetization versus applied magnetic field for samples of Fe in PMMA and PDMS.

clusters in the thin polymer samples. The transition at 1580 Oe is not present neither in the simulated nor in the bulk spectrum, and is associated to the presence of Fe(III) ions in the polymer. This supports our initial observation that the Fe4 cluster may be dissociated during the polymer casting process, releasing the free ions in the solid solution. In figure 6.15 the transition field of the angle dependent transition is plotted in function of the measurement angle α. A periodicity of the transition field with the angle is observed, and a sum of cosine functions fits the data (red trace). Besides, a transition at slightly higher fields appears at angles approximately between 30^o and 90^o. The presence of this second transition is also evidenced by the simulation results shown in figure 6.16.

In these graphs the transition fields are plotted in function of the angles θ defining the relative orientation between the molecule easy axis and the applied magnetic field. The color and the dimensions of the symbols denote the intensity of the transition. A transition (in green) appears for θ between 30 and 90 degrees and resonant fields between 2900 and 2100 Oe. This could explain the peak in 6.15, considering the arbitrary initial point for the rotations (θ_0) in the simulations. If the sample was made of randomly oriented Fe4Ph molecules, no angular dependence of the spectrum would be expected. Even if the assignment of these transitions is not possible, the presence of a small angular dependence shows that a partial orientation results from the polymer film casting process. Similar results have already been reported before [69] with Mn12 SMMs in PMMA films. These facts suggest that this simple polymer casting process could be used to produce thin transparent films containing oriented molecules. A sample was then prepared with

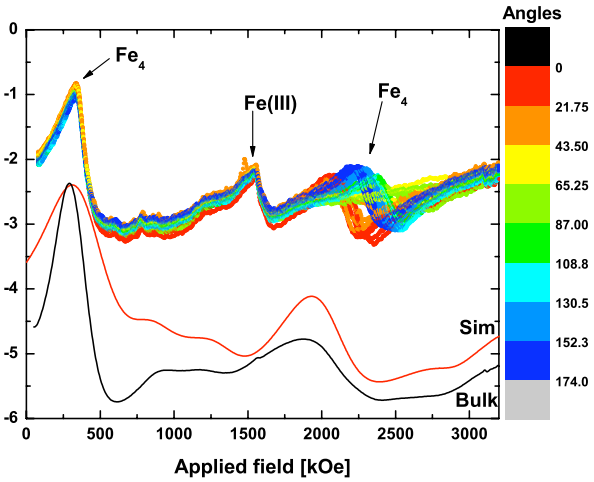

Figure 6.14: Angular dependence of the X-band EPR spectrum of Fe4C9SAc in PMMA at 5K. The lines at 2500 and 2250 Oe arise from transitions in the Fe4 $S = 5$ ground state multiplet. The Fe4 line at approximately 2250 kOe is clearly dependent upon the angle between the sample plane and the magnetic field direction, indicating partial orientation of clusters in this sample. The line at 1500 kOe is related to the presence of Fe(III) ions in the sample. A simulated spectrum (red trace) and a spectrum of a bulk sample (black trace) are shown for comparison.

the Fe4Ph SMM in polystyrene (PS) using the dip coating method (see subsection 6.2.1). The resulting film was approximately 200 nm thick. The behavior of the MCD magnetization curve measured at 1.5 K with 405 nm light is similar to the behavior observed in the much thicker ($\sim 20\mu$m measured with a micrometer) PMMA sample, as shown in figure 6.17. In this thinner sample the saturation is reached at slightly lower fields, indicating a higher degree of orientation.

As mentioned before, MCD is intrinsically orientation-selective, as the electronic transitions involved are polarized along molecular reference frame axes ([67], [69]). This fact may be clearly seen in figure 6.18, in which different wavelengths were employed to measure the MCD of Fe4 in PMMA, at the same temperature (1.5K). The left panel shows the curves obtained with 405, 476.5, 488, 496.5 and 514.5 nm. The curves display the paramagnetic behavior of this molecular cluster at this temperature range, with a clear saturation of the magnetization at fields above 20 kOe. This fact suggests a strong C-term contribution to the MCD at these

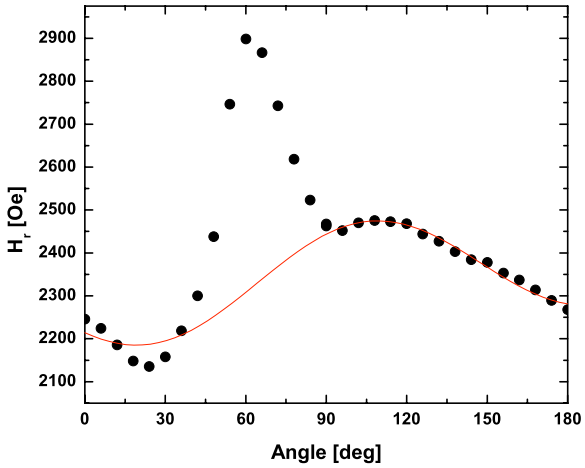

Figure 6.15: Angular dependence of the transition fields observed in the spectra from figure 6.14. The angle reported corresponds to the angle between the plane of the polymer film and the direction of the magnetic field of the EPR spectrometer.

wavelengths. The same measurement was performed at 632.8 nm, but in this case no saturation of the MCD was observed up to 40 kOe (figure 6.18, right panel), indicating the absence of a C-term at this frequency. Further measurements performed at 904 nm displayed no saturation up to 40 kOe. In order to better understand the observed curves, a computer program[7] based on the variable temperature-variable field MCD (VTVH-MCD) model presented in chapter 3, section 3.3 was used to fit these MCD vs. applied field curves. The program considers the C-term contribution to the electronic transitions that give rise to the observed MCD intensity, and yields their polarization and transition moments. It is also possible to obtain values of the g-factor and the D and E zero-field splitting terms. The results of the fits for the curves shown in figure 6.13 are summarized in table 6.1. The values for g and D were kept constant during the procedure, in order to obtain the values of the transition moments and the percentage polarization along x,y and z. If g and D are defined as fit parameters, the obtained values (table 6.2) do not agree very well with results obtained from magnetic susceptibility measurements and EPR spectroscopy ([44]). The source of the discrepancy between the values of these parameters obtained from the MCD fits and the standard values (EPR, magnetic measurements) is thought to be due to the

[7]Program written by Dr. Stergios Piligkos, Chemistry Department, University of Copenhagen

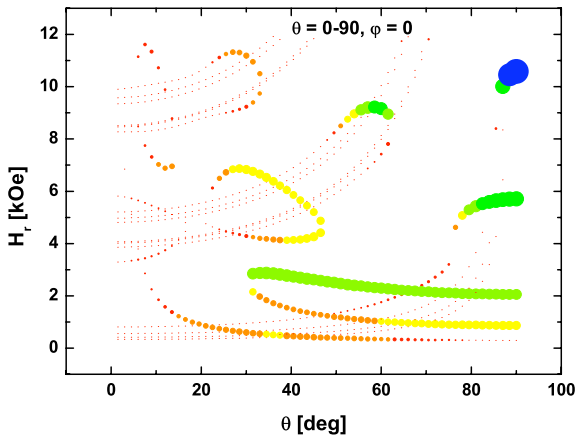

Figure 6.16: Simulated dependence of the EPR transition fields and the transition intensities with the orientation of the sample with respect to the magnetic field, given by the angle θ.

presence of the free (uncoupled) Fe(III) ion in the samples, as evidenced by the EPR spectra in 6.14 that could be contributing to the total measured MCD. The transition polarizations in the compound in PMMA are seen to be slightly less z-polarized than in the compound in PDMS (87% z-polarization in PMMA, 98% in PDMS). As the clusters are the same, as well as the experimental conditions, we are led to believe that the anisotropy in cluster orientations in the PMMA caused this artifact.

The data taken at different wavelengths provided by the Ar:ion laser and also with 632.8 nm light, from the PMMA sample, was then analyzed with the same computer program. The

	Transition moments			**Linear polarizations**		
	yz	**xz**	**xy**	**x**	**y**	**z**
PMMA	-0.00122	0.00066	-0.00108	0.17591	0.60096	0.22313
PDMS	-0.01143	-0.02306	-0.00156	0.01814	0.00446	0.97740

Table 6.1: Effective transition moments and polarizations of the PDMS and the PMMA samples measured with 476.5 nm at 1.5K, from the VTVH MCD fits.

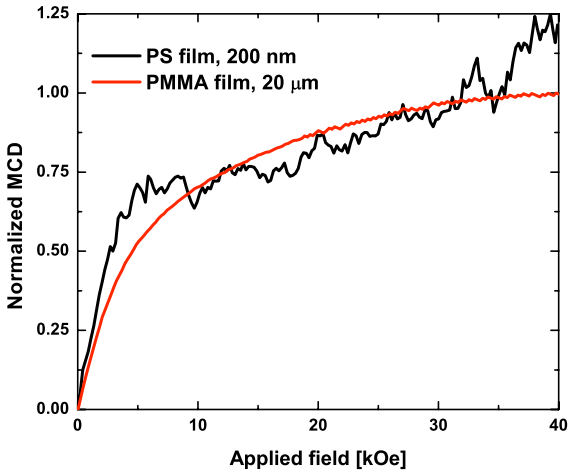

Figure 6.17: MCD curves of the Fe4 embedded in PS, dip-coated on a silica slab. The PMMA curve is shown for comparison.

resulting transition moments and relative linear polarizations are summarized in table 6.3. These values are defined as [67]:

	$\mathbf{g_x}$	$\mathbf{g_y}$	$\mathbf{g_z}$	$\mathbf{D}(\mathrm{cm}^{-1})$
PMMA	2.0025	2.0185	1.9562	-0.3328
PDMS	2.0085	2.0123	1.9315	-0.3591
EPR values	1.956	1.956	1.956	-0.437

Table 6.2: Zero-field splitting D and the components of the g factor, from the VTVH MCD fits of the PDMS and the PMMA samples measured with 476.5 nm at 1.5K. The EPR values are shown for comparison.

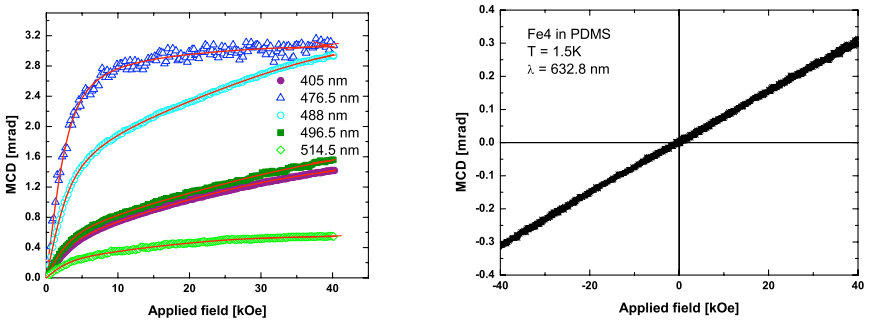

(a) MCD measured with 405, 476.5, 488, 496.5 and 514.5 nm light.

(b) MCD measured with 632.8 nm light

Figure 6.18: The MCD magnetization curves of Fe4C9SAc in PMMA for several wavelengths. While at wavelengths from 405 to 514.5 nm the paramagnetic behavior of the cluster at this temperature is clearly visible, while at 632.8 nm this behavior is not observed. This shows that there should be a C-term contribution to the MCD band in the 405 - 514 nm range, while at 632.8 nm the MCD transitions are not related to a C-term, as the paramagnetic behavior of the cluster is not observed.

$$
\begin{aligned}
M_{xy}^{eff} &= \sum_{K\neq A,J} (\vec{D}_x^{KA}\vec{D}_y^{JK} - \vec{D}_y^{KA}\vec{D}_x^{AJ})\frac{\overline{L}_z^{KJ}}{\Delta_{KJ}} + (\vec{D}_x^{AJ}\vec{D}_y^{JK} - \vec{D}_y^{AJ}\vec{D}_x^{JK})\frac{\overline{L}_z^{KA}}{\Delta_{KA}} \\
\vec{D}^{AB} &= \langle ASS|\vec{m}|BSS\rangle \\
\overline{L}_p^{AJ} &= \Im\{\langle ASS|\sum_i h_p(i)s_0(i)|JSS\langle_0\}
\end{aligned}
\tag{6.1}
$$

and analogously for M_{yz}^{eff} andM_{xz}^{eff}. In the expressions above, $\vec{m}$ is the electric dipole operator, $h_m(i)$ is a standard component of the reduced spin-orbit operator and $\vec{s}(i)$ is the spin-angular momentum operator for spin i. The other terms follow the notation of chapter 3. The relative linear polarizations are given by:

$$
\%x = 100\text{x}\frac{(M_{xy}^{eff}M_{xz}^{eff})^2}{(M_{xy}^{eff}M_{xz}^{eff})^2 + (M_{xy}^{eff}M_{yz}^{eff})^2 + (M_{xz}^{eff}M_{yz}^{eff})^2} \tag{6.2}
$$

and cyclic permutations.

We can see that the relative polarization gradually changes from the z axis towards the xy

	Transition moments			Linear polarizations		
	yz	xz	xy	x	y	z
405 nm	0.00136	-0.00229	-0.00017	0.01493	0.00529	0.97978
476.5 nm	-0.00122	0.00066	-0.00108	0.17591	0.60096	0.22313
488 nm	-0.00831	0.00694	-0.00058	0.00489	0.00700	0.98810
496.5	-0.00530	0.00440	-0.00021	0.00155	0.00225	0.99619
514.5 nm	0.00642	-0.00679	-0.00009	0.00020	0.00018	0.99962
632.8 nm	-0.00483	0.00461	0.00000	0.00000	0.00000	1.0

Table 6.3: VTVH MCD fit results for Fe4 in PMMA at 1.5K measured at several wavelengths (405 nm to 514.5 nm). The results from the 632.8 nm measurement refer to a PDMS sample and are show for comparison.

plane as the wavelength goes from 405 nm to 476.5 nm, and then becomes again strongly z polarized at 514.5 nm. At 632.8 nm the only contribution to the MCD arise from xz and yz transition moments giving a completely z polarized transition, and no saturation. We are then led to believe that some polarization out of the z axis must be present in order to probe this molecule's C-term. The linear contribution superimposed to the MCD curves arising from z-polarized transitions is clearly seen comparing the polarization values of table 6.3 and the curves in figure 6.18. The curve measured with 476.5 nm shows almost no linear dependence with the applied magnetic field at saturation, contrary to the curves measured with the other wavelengths, all of them displaying a saturation field proportional to $\vec{H}$ to some extent. Looking at the values of the effective transition moments M_{xy}^{eff},M_{yz}^{eff}andM_{xz}^{eff} for each wavelength (figure 6.20) we can see that the observation of an MCD C-term is related to the presence of M_{xy}^{eff}. At 632.8 nm, $M_{xy}^{eff} \rightarrow 0$, the transitions are completely z polarized and no C-term is observed. If the fits are done in order to obtain the spin Hamiltonian parameters D and g, the obtained values are shown in table 6.4. The D values are always about 0.1cm^{-1} below the value obtained from EPR and magnetic susceptibility measurements ($D = -0.435$ and $D = -0.437\text{cm}^{-1}$, respectively). The reason may be the presence of the Fe(III) ion as well as impurities in the sample, as seen in the EPR spectra in figure 6.14. This may be the result of the degradation of the Fe4 cluster in the polymer matrix.

Continuing this study of the Fe4 cluster, the MCD was measured in function of applied field at different temperatures. These measurements were performed with a 405 nm laser due to its

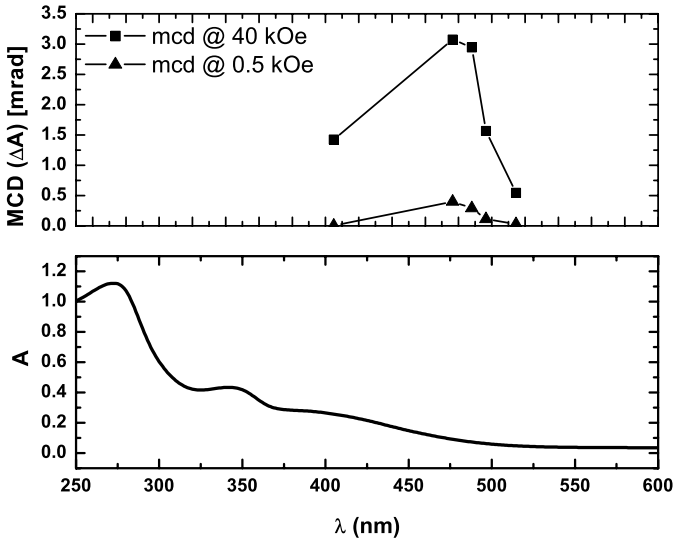

Figure 6.19: The UV-Vis absorption spectrum for Fe4C9SAc in PDMS. The polymer contribution to the spectrum was subtracted. On the upper panel the MCD intensities are plotted in function of wavelength. These data suggests the presence of an MCD broad band between 400 and 520 nm.

superior stability with respect to the Ar:ion laser. The curves are shown on the left panel of figure 6.21. On the right panel the isotherms MCD vs. H/T are represented. Nesting of these isotherms is observed, as is expected in this paramagnetic system, and the behavior (higher temperature isotherms above low temperature ones) is the same as seen in magnetic measurements of the same molecule [44]. In this case, however, the value of the total spin cannot be directly obtained from the saturation of these curves, but they serve as further indication that an MCD measurement is probing the paramagnetism of this species. The fitting routine available is not appropriate for this kind of analysis. But fits may be performed in the MCD vs. H curves, and the results are summarized in table 6.5 and in the figure 6.22.

The next step in the study of the Fe4 SMM in non-crystalline environments was the preparation of SAMs on gold surfaces (see subsection 6.2.1) and their magnetic characterization. The first MCD measurements were performed at 1.5 K with 405 nm light. This choice of wavelength was motivated by the stability of the source with respect to the 476.5 nm line of the Ar:ion

	$\mathbf{g_x}$	$\mathbf{g_y}$	$\mathbf{g_z}$	$\mathbf{D}(\mathrm{cm}^{-1})$
405 nm	2.0180	1.9697	2.0159	-0.4258
476.5 nm	2.0025	2.0185	1.9562	-0.3328
488 nm	2.0088	2.0194	1.9488	-0.3415
496.5 nm	2.0026	2.0223	1.9575	-0.3423
514.5 nm	2.0095	2.0265	1.9406	-0.3457
632.8 nm	2.0093	2.0211	1.9375	-0.3347
EPR values	1.956	1.956	1.956	-0.437

Table 6.4: Zero-field splitting *D* and the components of the *g* factor, from the VTVH MCD fits of the PMMA sample measured at 1.5 K with several wavelengths.

	Transition moments			**Linear polarizations**		
	yz	**xz**	**xy**	**x**	**y**	**z**
1.5 K	0.00354	-0.00448	-0.00015	0.00186	0.00116	0.99697
5 K	-0.01889	0.01818	-0.00008	0.00002	0.00002	0.99996
15 K	4.86851	-5.01355	0.08622	0.00031	0.00030	0.99939
29 K	-34.21659	35.47660	-0.96796	0.00080	0.00074	0.99846

Table 6.5: Effective transition moments and polarizations for Fe4C9SAc in PMMA at measured with 405 nm at several temperatures, from the VTVH MCD fits.

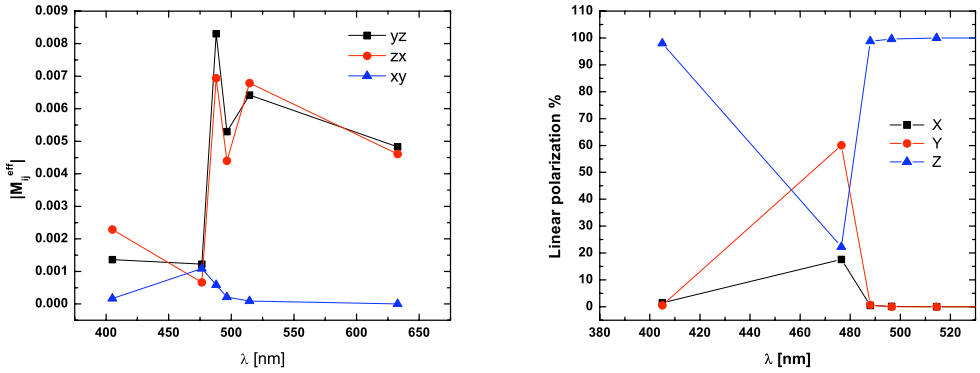

(a) Absolute value of the effective transition moments for 405, 476.5, 488, 496.5, 514.5 nm and 632.8 nm light, at 1.5 K.

(b) Relative linear polarizations, determined according to 6.2

Figure 6.20: Effective transition moments and polarization of the Fe4 SMM for several wavelengths, from VTVH-MCD fits.

laser. Even though this last wavelength produces the largest MCD at saturation (see figure 6.18) compared to the other wavelengths available that are able to probe the paramagnetism of this molecular magnet, it is way too noisy for high sensitivity measurements. The fluctuations of the order of ± 250 μrad observed at saturation (figure 6.18) would mask the signal arising from the sample, of the order of tens of μrad. In fact, the surface density of Fe4 clusters derived from STM images is 0.061 units/nm^2, which for a laser beam spot area of 0.44 mm^2 (the 405 nm laser has a larger spot size) yields a value for the saturation MCD of 0.99 μrad for 1 SAM. This is way below our sensitivity limit, and stacking 5 layers as done with the Mn12 SAMs will increase this value to 5 μrad, still below the minimum sensitivity range, between 6 and 8 μrad. In fact, the measurements showed that the Fe4 SAM and the clean substrate yielded essentially the same curves. In order to increase the signal, a trial measurement was made with an Fe4 SAM deposited on a rough Au substrate. The idea is to exploit the local electric field enhancement expected in the vicinity of rough noble metal surfaces, as for example in single-molecule SERS (Surface Enhanced Raman Scattering [154]). It has been demonstrated that this effect can enhance the MCD of magnetic nanoparticles (Shemer et al. in [155] and Lieberman et al. in [156]) adsorbed on gold surfaces, with a nearly 5-fold increase of the saturation MCD for measurements in transmission. Similar phenomena have also been reported for magnetic nanoparticles bound

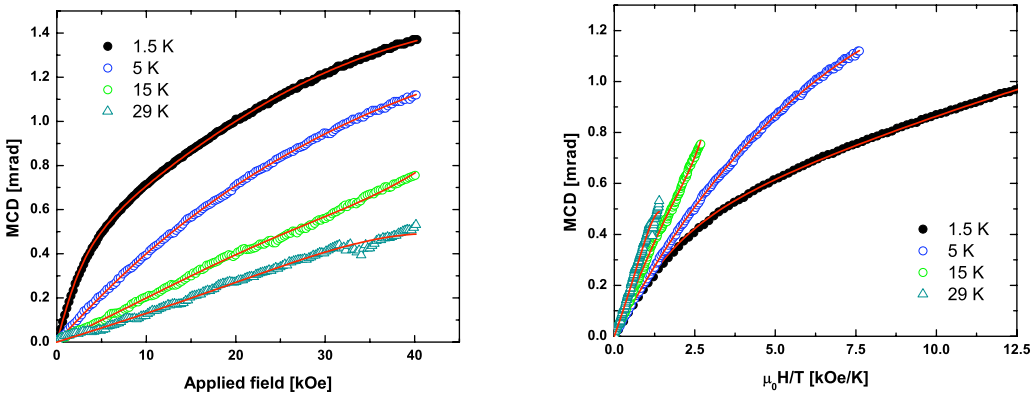

(a) MCD vs. H, 405 nm

(b) MCD vs. H/T, 405 nm

Figure 6.21: Temperature dependence of the MCD magnetization curves of Fe4C9SAc in PMMA, measured at 405 nm. The red lines correspond to the best fit obtained from the model presented in section 3.3. On the right-hand side the MCD vs. H/T curves are shown.

to noble metal nanoparticles [157], and YIG (Yttrium-Iron Garnet) films with Au nanoparticles embedded in them. In all cases significant modifications of the magneto-optical response was observed, generally in the form of enhancements or sigh changes. The origin of these effects is ascribed to the enhancement of the local electric field due to the evanescent mode associated to the surface plasmon resonance of the noble metal.

The substrate was prepared by thermal evaporation of Au on a clean quartz slab. The evaporation was performed in high vacuum conditions (base pressure inside the chamber of the order of $1\text{x}10^{-7}$ mbar) and the thickness of the deposited gold layer was controlled by a calibrated Quartz Crystal Microbalance (QCM), schematized in figure 6.23. This system determines the variation in mass (Δm) deposited on it by tracking the frequency of a quartz oscillator. The relation is given by the Sauerbrey equation:

$$\Delta f = \frac{-2f_0^2}{A\rho_q v_q}\Delta m \tag{6.3}$$

where f_0 is the resonant frequency of the quartz crystal, A is the active area of the crystal (between the electrodes), ρ_q is the density of the quartz and v_q is the shear wave velocity in quartz. A calibration allows the thickness of the evaporated layer to be obtained from Δm. The

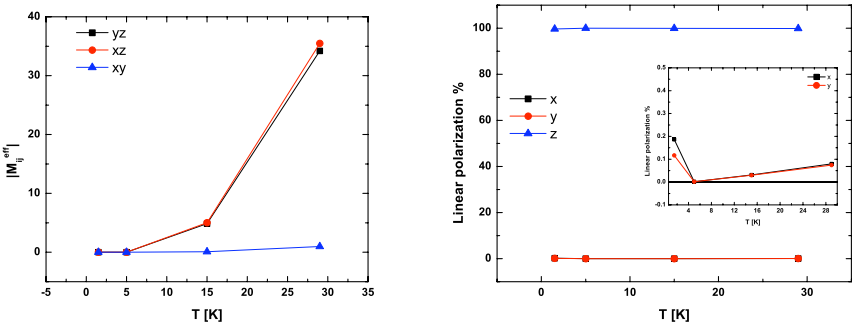

(a) Absolute value of the effective transition moments at 1.5, 5, 15 and 29 K, measured with 405 nm light.

(b) Relative linear polarizations. The inset shows the presence of x and y polarized transitions at low temperature.

Figure 6.22: Effective transition moments and polarizations of the Fe4 SMM for several temperatures, from VTVH-MCD fits.

degree of roughness of the surface depends on the gold evaporation rate.

The Atomic Force Microscopy (AFM) image of the surface obtained by this process is shown in figure 6.24. The average height of the features is 8.18 nm and the RMS roughness is 1.43 nm. A SAM of Fe4C9SAc clusters was then deposited on this substrate following the same methods used before. The MCD of the obtained SAM was then measured at 1.5 K with 405 nm light. The resulting curve, after the substrate contribution was subtracted, is shown in figure 6.25. This is the result of the average of data from 4 consecutive measurements. The behavior resembles the expected behavior of a paramagnetic system, with saturation at fields beyond 20 kOe. The extremities of the curves are noisier because of small displacements of the sample holder rod at high fields during the field sweep (sweep rate 1 T/min). The saturation values are roughly $+16\mu$rad and -18μrad. Considering that the saturation MCD calculated for 1 monolayer was around 1 μrad, this value would suggest an increase of about 16 times in the signal. This agrees with results previously reported by Shemer et al. [155].

Even though this result seems promising, the fact that we are working at about 1K above the blocking temperature of this SMM precludes the observation of hysteresis. Measurements at lower temperatures are not possible with our current setup, as the use of a pumped ^{3}He refrigerator would be mandatory in order to reach the necessary temperature range. An ac susceptibility measurement of this sample could help us establish that the observed data really arises from

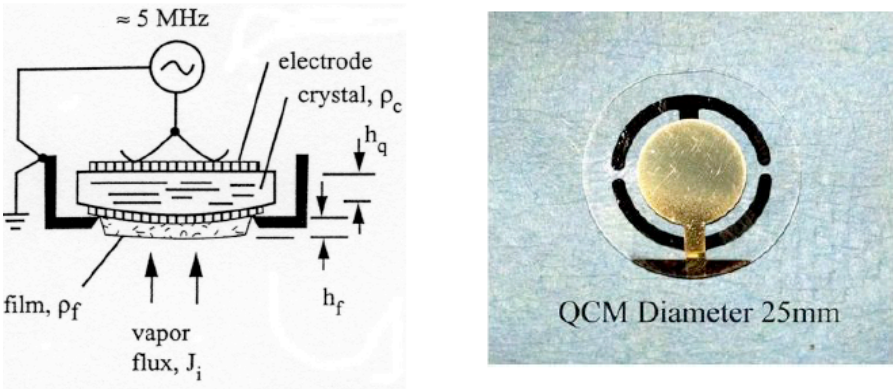

Figure 6.23: The Quartz Crystal Microbalance (QCM).

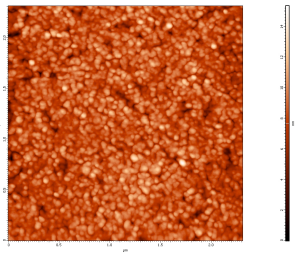

Figure 6.24: AFM image taken in tapping mode of a 13 nm (QCM) thick rough Au surface for the preparation of Fe4C9SAc SAMs.

an intact monolayer of Fe4 SMMs. But, despite our efforts, up to now the magneto-optical ac susceptibility setup described in subsection 4.2.2 has not been sensitive enough to measure ac susceptibility in these conditions. Again, we must mention that the most suitable techniques for the determination of the magnetic moment and slow relaxation of the magnetization of SMM monolayers on surfaces are XAS and XMCD. Further information about the electronic structure and the oxidation state of the deposited molecules may also be obtained, putting these techniques a the forefront of research in surface magnetism. Finally, it is appropriate to mention that recently it has been established, by XMCD measurements, that monolayers of Fe4C9SAc on gold surfaces display hysteresis [158]. This recent result is an important breakthrough in the field of molecular magnetism as it paves the way to a myriad of applications of bistable single molecules deposited on surfaces.

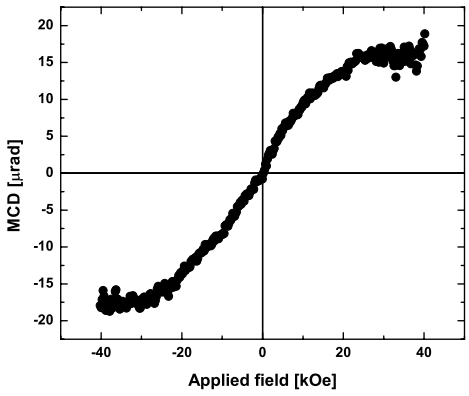

Figure 6.25: MCD vs. applied field for a monolayer of Fe4C9SAc deposited on a rough gold surface. The curve corresponds to an average of several data acquisitions.

6.3 Conclusions

Magneto-optic measurements of hysteresis cycles of derivatives of the Mn12 SMM in different non-crystalline environments indicate that the magnetism of this cluster is highly sensitive to the surroundings. This suggests that care must be taken if it is used in applications where it is not in the single-crystal form. In the ultimate case of a monolayer, Mn12 no longer displays magnetic hysteresis, a fact that seriously hampers its future applications, especially in spintronics and molecular electronics. The same methods were employed in order to study the SMMs of the Fe4 family in diluted solid solutions and monolayers on gold surfaces. As our experimental setups are not capable of operating at temperatures low enough to cause the blocking of this cluster's magnetization, its paramagnetic ground state was investigated by MCD measurements, and fits of the data to a theoretical model allowed the characterization of its electronic states and their relation to the observed MCD. To our knowledge this is the first study of this kind done in a SMM of the Fe4 family. It is demonstrated that the use of high sensitivity magneto-optical techniques such as MCD as a tool to investigate the magnetism of molecular systems offers a tempting alternative to other magnetic characterization techniques, especially because very high sensitivities may be achieved with relatively simple instrumentation. In fact, the simplicity of the MCD instrumentation and measurement procedure in addition to its power to probe the magnetism of highly diluted samples, clearly indicates the importance of further developments

of this technique. Further enhancements in sensitivity can make possible the investigations of the magnetism of nanosystems in a small scale laboratory, in contrast to current magnetic characterization techniques such as XMCD, that rely on the use of large scale facilities (synchrotron laboratories, in this case).

7 Conclusions and Final Remarks

MCD measurements have proved to be a powerful and valuable tool in the magnetic characterization of nanoparticles and single-molecule magnet systems. They present a good alternative to widely used magnetometric methods when the investigated systems are highly diluted in a transparent matrix and for nanostructures such as monolayers whose magnetism cannot be probed by the available magnetic characterization methods due to sensitivity limits. However, particularities arising from the mechanism of magneto-optical response indicate they should be used with care. The orientational selectivity of MCD should be taken in consideration when investigating magnetic molecules, while for magnetic alloy nanoparticles the experimentalist should bear in mind that optically induced changes in electronic structure will produce results different from the ones obtained from traditional magnetometric techniques. These facts indicate that a deep knowledge of the electronic structure of nanostructured systems is fundamental to the interpretation of the data. Of course, it also suggests the power of magneto-optics as a tool to investigate electronic structure. Nevertheless, the magneto-optical methods explored are a good alternative to magnetometric techniques whenever sensitivity becomes an issue. The development of a magneto-optical ac susceptometer adds further possibilities of elucidating interesting phenomena arising in nanostructured magnetic systems as a result of the interaction between light and electronic structure, as was demonstrated in chapter 5. It is a relatively easy technique to implement in a magneto-optics laboratory, with only a few modifications in instrumentation being necessary. This last technique still needs further developments, in order to increase its sensitivity and its signal-to-noise ratio, with the ultimate goal of reaching monolayer sensitivity. The current trends in surface magnetism and molecular magnetism on surfaces could profit much from these developments. Finally, magneto-optical measurements are a practical option to XMCD as this last characterization method needs synchrotron-generated X-rays, while MCD measurements can be easily done in a small laboratory.

Bibliography

[1] S. Accorsi, A.-L. Barra, A. Caneschi, G. Chastanet, A. Cornia, A.C. Fabretti, D. Gatteschi, C. Mortalo, E. Olivieri, F. Parenti, P. Rosa, R. Sessoli, L. Sorace, W. Wernsdorfer, and L. Zobbi. Tuning Anisotropy Barriers in a Family of Tetrairon(III) Single-Molecule Magnets with an $S = 5$ Ground State. *Journal of the American Chemical Society*, 128(14):4742–4755, 2006.

[2] R. L. Novak, F. Pineider, C. de Julian Fernandez, L. Gorini, L. Bogani, C. Danieli, L. Cavigli, A. Cornia, and R. Sessoli. Magneto-optical studies on the molecular cluster Fe4 in different polymeric environments. *Inog. Chim. Acta*, 361:3970, 2008.

[3] Lucia Cavigli. *Nonlinear and Magneto-Optical Properties of Nanosized Magnetic Materials*. Dottorato di ricerca in scienza e tecnologia dei materiali, Dipartimento di Fisica – Università degli Studi di Firenze, 2006.

[4] Dante Gatteschi, Roberta Sessoli, and Jacques Villain. *Molecular Nanomagnets*. Oxford University Press, 2006.

[5] V. L. Mironov. *Fundamentals of the scanning probe microscopy*. The Russian Academy of Sciences – Institute of Physics of Microstructures, 2004.

[6] G. Mattei, C. de Julian Fernandez, P. Mazzoldi, C. Sada, G. De, G. Battaglin, C. Sangregorio, and D. Gatteschi. Synthesis, Structure, and Magnetic Properties of Co, Ni, and Co-Ni Alloy Nanocluster-Doped SiO_2 Films by Sol-Gel Processing. *Chem. Mater.*, 14:3440–3447, 2002.

[7] Lapo Bogani. *Magnetic and Optical Properties of Molecular Magnets*. Dottorato di ricerca in scienze chimiche, Dipartimento di Chimica – Università degli Studi di Firenze, 2006.

[8] A. Hernando, P. Crespo, and M. A. Garcia. Metallic Magnetic Nanoparticles. *The Scientific World Journal*, 5:972 – 1001, 2005.

[9] G. Mattei, C. de Julián Fernández, G. Battaglin, C. Maurizio, P. Mazzoldi, and C. Scian. Structure and thermal stability of Au-Fe alloy nanoclusters formed by sequential ion implantation in silica. *Nucl. Instr. and Meth. B*, 250:225–228, 2006.

[10] Miguel Clemente-León, Hélène Soyer, Eugenio Coronado, Christophe Mingotaud, Carlos J. Gómez-García, and Pierre Delhaès. Langmuir-Blodgett Films of Single-Molecule Nanomagnets. *Angew. Chem. Int. Ed.*, 37:2842 – 2845, 1998.

[11] Laura Zobbi, Matteo Mannini, Mirko Pacchioni, Guillaume Chastanet, Daniele Bonacchi, Chiara Zanardi, Roberto Biagi, Umberto del Pennino, Dante Gatteschi, Andrea Cornia, and Roberta Sessoli. Isolated single-molecule magnets on native gold. *Chem. Commun.*, pages 1640 – 1642, 2005.

[12] L. Néel. *Ann. Geophys.*, 5:99, 1949.

[13] Jr William Fuller Brown. Thermal Fluctuations of a Single-Domain Particle. *Phys. Rev.*, 130:1677–1686, 1963.

[14] C. P. Bean and J. D. Livingston. Superparamagnetism. *J. Appl. Phys.*, 30:120S–129S, 1959.

[15] E. C. Stoner and E. P. Wohlfarth. A Mechanism of Magnetic Hysteresis in Heterogeneous Alloys. *Phil. Trans. Royal Soc. London*, A240:599, 1949.

[16] Xavier Batlle and Amilcar Labarta. Finite-size effects in fine particles: magnetic and transport properties. *J. Phys. D: Appl. Phys.*, 35:R15–R42, 2002.

[17] Q. A. Pankhurst, J. Connolly, S. K. Jones, and J. Dobson. Applications of magnetic nanoparticles in biomedicine. *J. Phys. D: Appl. Phys.*, 36:R167 – R181, 2003.

[18] H. B. Heersche, Z. de Groot, J. A. Folk, H. S. J. van der Zant, C. Romeike, M. R. Wegewijs, L. Zobbi, D. Barreca, E. Tondello, and A. Cornia. Electron Transport through Single Mn_{12} Molecular Magnets. *Physical Review Letters*, 96(20):206801, 2006.

[19] Lapo Bogani and Wolfgang Wernsdorfer. Molecular spintronics using single-molecule magnets. *Nature Materials*, 7:179, 2008.

[20] Michael N. Leuenberger and Daniel Loss. Quantum computing in molecular magnets. *Nature*, 410:789, 2001.

[21] Richard E. P. Winpenny. Quantum Information Processing Using Molecular Nanomagnets As Qubits. *Angew. Chem. Int. Ed.*, 47:7992, 2008.

[22] Filippo Troiani, Marco Affronte, Stefano Carretta, Paolo Santini, and Giuseppe Amoretti. Proposal for Quantum Gates in Permanently Coupled Antiferromagnetic Spin Rings without Need of Local Fields. *Phys. Rev. Lett.*, 94:190501, 2005.

[23] W. Wernsdorfer, K. Hasselbach, A. Benoit, W. Wernsdorfer, B. Barbara, D. Mailly, J. Tuaillon, J. P. Perez, V. Dupuis, J. P. Dupin, G. Guiraud, and A. Perex. High sensitivity magnetization measurements of nanoscale cobalt clusters. *Journal of Applied Physics*, 78(12):7192–7195, 1995.

[24] A. D. Kent, S. von Molnar, S. Gider, and D. D. Awschalom. Properties and measurement of scanning tunneling microscope fabricated ferromagnetic particle arrays (invited). *J. Appl. Phys.*, 76(10):6656–6660, 1994.

[25] Z. Q. Qiu and S. D. Bader. Surface magneto-optic Kerr effect. *Review of Scientific Instruments*, 71(3):1243–1255, 2000.

[26] M. Brust, M. Walker, D. Bethell, D.J. Schiffrin, and R. Whyman. Synthesis of Thiol Derivatised Gold Nanoparticles in a Two Phase Liquid/Liquid System. *J. Chem. Soc., Chem. Commun.*, page 801, 1994.

[27] M. Brust, D. Bethell, D.J. Schiffrin, and C. Kiely. Novel Gold-Dithiol Nano-Networks with Non-metallic Electronic Properties. *Adv. Mater.*, 7:795, 1995.

[28] M.Brust and C.J.Kiely. Some Recent Advances in Nanostructure Preparation from Gold and Silver Particles: A Short Topical Review. *Colloids and Surfaces A*, 202:175, 2002.

[29] Brian L. Cushing, Vladimir L. Kolesnichenko, and Charles J. O'Connor. Recent Advances in the Liquid-Phase Syntheses of Inorganic Nanoparticles. *Chem. Rev.*, 104:3893 – 3946, 2004.

[30] L. Bogani, L. Cavigli, M. Gurioli, R. L. Novak, M. Mannini, A. Caneschi, F. Pineider, R. Sessoli, M. Clemente-León, E. Coronado, A. Cornia, and D. Gatteschi. Magneto-Optical Investigations of Nanostructured Materials Based on Single-Molecule Magnets Monitor Strong Environmental Effects. *Advanced Materials*, 19(22):3906–3911, 2007.

[31] J. L. Dormann, D. Fiorani, and E. Tronc. Magnetic Relaxation in Fine-Particle Systems. *Adv. Chem. Phys.*, 98:283, 1997.

[32] C. de Julián Fernández. Influence of the temperature dependence of anisotropy on the magnetic behavior of nanoparticles. *Phys. Rev. B*, 72:054438, 2005.

[33] Sushin Chikazumi and Stanley Charap. *Physics of Magnetism*. Krieger Publishing Company, 1964.

[34] R. H. Kodama. Magnetic nanopaticles. *J. Magn. Magn. Mater.*, 200:359 – 372, 1999.

[35] C. L. Dennis, R. P. Borges, L. D. Buda, U. Ebels, J. F. Gregg, M. Hehn, E. Jouguelet, K. Ounadjela, I. Petej, I. L. Prejbeanu, and M. J. Thornton. The defining length scales of mesomagnetism: a review. *J. Phys.: Condens. Mater*, 14:R1175 – R1262, 2002.

[36] Claudio Sangregorio. *Magnetic Nanoparticles: The Sol-Gel and the Molecular Approaches*. Dottorato di ricerca in scienza e tecnologia dei materiali, Dipartimento di Chimica – Università degli Studi di Firenze, 1995.

[37] Wolfgang Wernsdorfer. Classical and quantum magnetization reversal studied in nanometer-sized particles and clusters. *Adv. Chem. Phys.*, 118:99, 2001.

[38] J. I. Gittleman, B. Abeles, and S. Bozowski. Superparamagnetism and relaxation effects in granular Ni-Si$O2$ and Ni-$Al2O3$ films. *Phys. Rev. B*, 9(9):3891–3897, May 1974.

[39] R. Sessoli, D. Gatteschi, A. Caneschi, and M.A. Novak. Magnetic bistability in a metal-ion cluster. *Nature*, 365:141, 1993.

[40] L. Thomas, F. Lionti, R. Ballou, D. Gatteschi, R. Sessoli, and B. Barbara. Macroscopic quantum tunnelling of magnetization in a single crystal of nanomagnets. *Nature*, 383:145, 1996.

[41] Jonathan R. Friedman, M.P. Sarachik, J. Tejada, and R. Ziolo. Macroscopic Measurement of Resonant Magnetization Tunnelling in High-Spin Molecules. *Phys. Rev. Lett.*, 76:3830, 1996.

[42] K.M. Mertes, Y. Suzuki, M.P. Sarachik, Y. Myasoedov, H. Shtrikman, E. Zeldov, E.M. Rumberger, D.N. Hendrickson, and G. Christou. Mn_{12} acetate: a prototypical single molecule magnet. *Solid State Communications*, 127:131 – 139, 2003.

[43] A.L. Barra, A. Caneschi, A. Cornia, F. Fabrizi de Biani, D. Gatteschi, C. Sangregorio, R. Sessoli, and L. Sorace. Single-Molecule Magnet Behavior of a Tetranuclear Iron(III) Complex. The Origin of Slow Magnetic Relaxation in Iron(III) Clusters. *Journal of the American Chemical Society*, 121(22):5302–5310, 1999.

[44] Anne-Laure Barra, Federica Bianchi, Andrea Caneschi, Andrea Cornia, Dante Gatteschi, Lapo Gorini, Luisa Gregoli, Monica Maffini, Francesca Parenti, Roberta Sessoli, Lorenzo Sorace, and Anna Maria Talarico. New single-molecule magnets by site -specific substitution: Incorporation of "alligator clips" into Fe4 complexes. *Eur. J. Inorg. Chem.*, pages 4145–4152, 2007.

[45] Andrea Cornia, Antonio C. Fabretti, Pierfrancesco Garrisi, Cecilia Mortalò, Daniele Bonacchi, Dante Gatteschi, Roberta Sessoli, Lorenzo Sorace, Wolfgang Wernsdorfer, and Anne-Laure Barra. Energy-Barrier Enhancement by Ligand Substitution in Tetrairon(III) Single-Molecule Magnets. *Angew. Chem. Int. Ed.*, 43:1136–1139, 2004.

[46] S. Sugano and N. Kojima, editors. *Magneto-Optics*. Springer, 1999.

[47] Michael Faraday. *Diary, 13 September 1845*, volume 4. William Clowes and Sons, 1845.

[48] L. Cavigli, C. de Julian Fernandez, D. Gatteschi, M. Gurioli, C. Sangregorio, G. Mattei, P. Mazzoldi, and L. Bogani. Magneto-optical detection of the relaxation dynamics of alloy nanoparticles with a high-stability magnetic circular dichroism setup. *J. Magn. Magn. Mater.*, 316:e798–e801, 2007.

[49] F. D'Orazio, F. Lucari, C. de Julin, G. Mattei, S. Lo Russo, C. Maurizio, P. Mazzoldi, C. Sangregorio, D. Gatteschi, F. Gonella, E. Cattaruzza, C. Battaglin, and D. Fiorani. Magnetic characterization of ion implanted CoNi-SiO_2 granular film. *Journal of Magnetism and Magnetic Materials*, 242-245(Part 1):627 – 630, 2002.

[50] B. Kalska, J. J. Paggel, P. Fumagalli, M. Hilgendorff, and M. Giersig. Magneto-optics of of thin magnetic films composed of Co nanoparticles. *J. Appl. Phys.*, 92(12):7481, 2002.

[51] C. Petit, S. Rusponi, and H. Brune. Magnetic properties of cobalt and cobalt-platinum nanocrystals investigated by magneto-optical Kerr effect. *J. Appl. Phys.*, 95(8):4251, 2004.

[52] R. L. Novak et al. *To be published*.

[53] C. de Julián Fernández et al. Au-Fe solid solution nanoparticles: magnetic, optical, magneto-optical properties and thermal stability. *To be published*.

[54] Andrew J. Thomson, Myles R. Cheesman, and Simon J. George. Variable-Temperature Magnetic Circular Dichroism. *Methods in Enzymology*, 226:199, 1993.

[55] Vasily S. Oganesyan, Simon J. George, Myles R. Cheesman, and Andrew J. Thomson. A novel, general method of analyzing magnetic circular dichroism spectra and magnetization curves of high-spin metal ions: Application to the protein oxidized rubredoxin, *Desulfovibrio gigas*. *J. Chem. Phys.*, 110(2):762, 1999.

[56] V.S. Oganesyan, M.R. Cheesman, and A.J. Thomson. Magnetic Circular Dichroism Evidence for a Weakly Coupled Heme-Radical Pair at the Active Site of Cytochrome cd1, a Nitrite Reductase. *Inorganic Chemistry*, 46(26):10950–10952, 2007.

[57] B. Beschoten, P. A. Crowell, I. Malajovich, D. D. Awschalom, F. Matsukura, A. Shen, and H. Ohno. Magnetic Circular Dichroism Studies of Carrier-Induced Ferromagnetism in $(Ga_{1-x}Mn_x)As$. *Phys. Rev. Lett.*, 83(15):3073–3076, Oct 1999.

[58] A. Kapitulnik, J. S. Dodge, and M. M. Fejer. High-resolution magneto-optic measurements with a Sagnac interferometer. *J. Appl. Phys.*, 75(10):6872, 1994.

[59] S. Spielman, J. S. Dodge, L. W. Lombardo, C. B. Eom, M. M. Fejer, T. H. Geballe, and A. Kapitulnik. Measurement of the spontaneous polar Kerr effect in $YBa_2Cu_3O_7$ and $Bi_2Sr_2CaCu_2O_8$. *Phys. Rev. Lett.*, 68(23):3472–3475, Jun 1992.

[60] R.C. Jones. A New Calculus for the Treatment of Optical Systems. *J. Opt. Soc. Am. A*, 31:488, 1941.

[61] M.J. Freiser. A Survey of Magnetooptic Effects. *IEEE Trans. Magn.*, 4:152, 1968.

[62] L. Landau and E. Lifchitz. *Electrodynamique des Milieux Continus*. Editions Mir, Moscou, 1969.

[63] P. Paroli. An introduction to magneto-optics. Lecture Notes, Istituto di Elettronica dello Stato Solido, CNR - Roma, Italy.

[64] Petros N. Argyres. Theory of the Faraday and Kerr Effects in Ferromagnetics. *Phys. Rev.*, 97:334, 1955.

[65] J.D. Jackson. *Classical Electrodynamics 3rd Edition*. J. Wiley and Sons, 1999.

[66] M. Born and E. Wolf. *Priciples of Optics, VII Edition*. Cambridge University Press, 1999.

[67] Frank Neese and Edward I. Solomon. MCD C-Term Signs, Saturation Behavior, and Determination of Band Polarizations in Randomly Oriented Systems with Spin $S \geq 1/2$. Applications to $S = 1/2$ and $S = 5/2$. *Inorg. Chem.*, 38:1847, 1999.

[68] Y. Fukuma, H. Asada, J. Yamamoto, F. Odawara, and T. Koyanagi. Large magnetic circular dichroism of Co clusters in Co-doped ZnO. *Applied Physics Letters*, 93(14):142510, 2008.

[69] Eric. J. L. McInnes, Elna Pidcock, Vasily Oganesyan, Myles R. Cheesman, Annie K. Powell, and Andrew Thomson. Optical Detection of Spin Polarization in Single-Molecule Magnets $[Mn_{12}O_{12}(O_2CR)_{16}(H_2O)_4]$. *J. Am. Chem. Soc.*, 124:9219, 2002.

[70] Myles R. Cheesman, Vasili S. Oganesyan, Roberta Sessoli, Dante Gatteschi, and Andrew J. Thomson. Magnetically induced optical bi-stability of the molecular nanomagnet $Mn_{12}O_{12}(OOCMe)_{16}(H_2O)_4$ in an organic glass. *Chem. Commun.*, page 1677, 1997.

[71] Riccardo Moroni, Renato Buzio, Andrea Chincarini, Ugo Valbusa, Francesco Buatier de Mongeot, Lapo Bogani, Andrea Caneschi, Roberta Sessoli, Lucia CAvigli, and Massimo Gurioli. Optically addressable single molecule magnet behaviour of vacuum-sprayed ultrathin films. *J. Mater. Chem.*, 18:109, 2008.

[72] M. A. Zaitoun, W. Roy Mason, and C. T. Lin. Magnetic Circular Dichroism Spectra for Colloidal Gold Nanoparticles in Xerogels at 5.5 K. *J. Phys. Chem. B*, 105:6780, 2001.

[73] P. J. Stephens. Theory of Magnetic Circular Dichroism. *J. Chem. Phys.*, 52:3489, 1970.

[74] P. J. Stephens. Magnetic Circular Dichroism. *Adv. Chem. Phys.*, 35:197, 1976.

[75] Susan B. Piepho and Paul N. Schatz. *Group Theory in Spectroscopy*. John Wiley and Sons, 1983.

[76] W. Roy Mason. *A Practical Guide to Magnetic Circular Dichroism Spectroscopy*. Wiley-Interscience, 2007.

[77] J. Badoz, M. P. Silverman, and J. C. Canit. Wave propagation through a medium with static and dynamic birefringence: theory of the photoelastic modulator. *J. Opt. Soc. Am. A*, 7:672, 1990.

[78] Grant R. Fowles. *Introduction to Modern Optics*. Dover Publications, 1989.

[79] A. Bajpai and A. Banerjee. An automated susceptometer for the measurement of linear and nonlinear magnetic ac susceptibility. *Review of Scientific Instruments*, 68(11):4075–4079, 1997.

[80] Ching-Hwa Ho, Chang-Hsun Hsieh, Ying-Jui Chen, Ying-Sheng Huang, and Kwong-Kau Tiong. Novel electronic design for double-modulation spectroscopy of semiconductor and semiconductor microstructures. *Review of Scientific Instruments*, 72(11):4218–4222, 2001.

[81] L. Koszegi, M. Foldeaki, and R. A. Dunlap. Variable frequency two-phase ac susceptometer for use in dc bias fields over the temperature range of 4.2 to 300 K. *Review of Scientific Instruments*, 62(3):793–796, 1991.

[82] S. Pütter, H. F. Ding, Y. T. Millev, H. P. Oepen, and J. Kirschner. Magnetic susceptibility: An easy approach to the spin-reorientation transition. *Phys. Rev. B*, 64(9):092409, 2001.

[83] J. R. Owers-Bradley, Wen-Sheng Zhou, and W. P. Halperin. Simple wide temperature range ac susceptometer. *Review of Scientific Instruments*, 52(7):1106–1107, 1981.

[84] A. D. Hibbs, R. E. Sager, S. Kumar, J. E. McArthur, A. L. Singsaas, K. G. Jensen, M. A. Steindorf, T. A. Aukerman, and H. M. Schneider. A SQUID-based ac susceptometer. *Review of Scientific Instruments*, 65(8):2644–2652, 1994.

[85] Fernando Palacio, editor. *Introduction to Physical Techniques in Molecular Magnetism – Yesa, 1999*, chapter AC Magnetic Measurements, A. Omerzu and T. Mertelj and J. Demsar and D. Mihailovic, pages 83–101. 1999.

[86] Uwe Bovensiepen. *Phasenübergänge in magnetischen Monolagen und austauschgekoppelten Schichten: Eine* in situ *Studie mit ac-Suszeptibilität und Kerr-Effekt*. Phd in physics, Fachbereich Physik der Freien Universität Berlin, 2000.

[87] Walter S. D. Folly. Construção de um susceptômetro AC simples e seu uso no estudo de processos de relaxação magnética do composto polinuclear Mn12AC. Master of science – physics, Instituto de Física – Universidade Federal do Rio de Janeiro, 1998.

[88] M. I. Youssif, A. A. Bahgat, and I. A. Ali. AC Magnetic Susceptibility Technique for the Characterization of High Temperature Superconductors. *Egyptian Journal of Solids*, 23(2):231–250, 2000.

[89] Martin Nikolo. Superconductivity: A guide to alternating current susceptibility measurements and alternating current susceptometer design. *Am. J. Phys.*, 63:57–65, 1995.

[90] M. J. Dunlavy and D. Venus. Critical slowing down in the two-dimensional Ising model measured using ferromagnetic ultrathin films. *Physical Review B (Condensed Mater and Materials Physics)*, 71(14):144406, 2005.

[91] M. J. Dunlavy and D. Venus. Critical susceptibility exponent measured from Fe/W(110) bilayers. *Phys. Rev. B*, 69(9):094411, 2004.

[92] D. Venus and M. J. Dunlavy. Dissipation in perpendicularly magnetized ultrathin films studied using the complex AC susceptibility. *J. Magn. Magn. Mater.*, 260(1-2):195–205, 2003.

[93] H. B. G. Casimir and F. K. du Pré. Thermodynamic interpretation of paramagnetic relaxation phenomena. *Physica*, 5:507, 1938.

[94] K. S. Cole and R. H. Cole. Dispersion and Absorption in Dielectrics I. Alternating Current Characteristics. *J. Chem. Phys.*, 9:341, 1941.

[95] C. S. Arnold, M. Dunlavy, and D. Venus. Magnetic susceptibility measurements of ultrathin films using the surface magneto-optic kerr effect: Optimization of the signal-to-noise ratio. *Review of Scientific Instruments*, 68(11):4212–4216, 1997.

[96] A. Aspelmeier, M. Tischer, M. Farle, M. Russo, K. Baberschke, and D. Arvanitis. Ac susceptibility measurements of magnetic monolayers: MCXD, MOKE and mutual inductance. *J. Magn. Magn. Mater.*, 146(3):256–266, 1995.

[97] F. Bensch, G. Garreau, R. Moosbühler, G. Bayreuther, and E. Beaurepaire. Onset of ferromagnetism in Fe epitaxially grown on GaAs(001) (4 x 2) and (2 x 6). *J. Appl. Phys.*, 89:7133–7135, 2001.

[98] G. Garreau, E. Beaurepaire, K. Ounadjela, and M. Farle. Spin-reorientation transition in ultrathin Tb/Co films. *Phys. Rev. B*, 53(3):1083–1086, Jan 1996.

[99] A. Berger, A. W. Pang, and H. Hopster. Magnetic reorientation transition of Gd(0001)/W(110) films. *Phys. Rev. B*, 52(2):1078–1089, 1995.

[100] A. Berger, S. Knappmann, and H. P. Oepen. Magneto-optical Kerr effect study of ac susceptibilities in ultrathin cobalt films. *J. Appl. Phys.*, 75:5598–5600, 1994.

[101] U. Bovensiepen, C. Rudt, P. Poulopoulos, and K. Baberschke. AC-susceptibility of Ni/W(1 1 0) ultrathin magnetic films: determination of the Curie temperature and critical behavior. *J. Magn. Magn. Mater.*, 231(1):65–73, 2001.

[102] Ben H. Erne, Maria Claesson, Stefano Sacanna, Mark Klokkenburg, Emile Bakelaar, and Bonny W.M. Kuipers. Low-frequency complex magnetic susceptibility of magnetic composite microspheres in colloidal dispersion. *J. Magn. Magn. Mater.*, 311:145–149, 2007.

[103] M. Farle, W. A. Lewis, and K. Baberschke. Detailed analysis of the in situ magneto-optic Kerr signal of gadolinium films near the Curie temperature. *Applied Physics Letters*, 62(21):2728–2730, 1993.

[104] M. Farle, A. Berghaus, Yi Li, and K. Baberschke. Hard-axis magnetization of ultrathin Ni(111) films on W(110): An experimental method to measure the magneto-optic Kerr effect in ultrahigh vacuum. *Phys. Rev. B*, 42(7):4873–4876, 1990.

[105] M. Farle, K. Baberschke, U. Stetter, A. Aspelmeier, and F. Gerhardter. Thickness-dependent Curie temperature of Gd(0001)/W(110) and its dependence on the growth conditions. *Phys. Rev. B*, 47(17):11571–11574, 1993.

[106] R. L. Rodríguez-Suárez, L. H. Vilela Le ao, F. M. de Aguiar, S. M. Rezende, and A. Azevedo. Exchange anisotropy determined by magnetic field dependence of ac susceptibility. *Journal of Applied Physics*, 94(7):4544–4550, 2003.

[107] C.S. Arnold. *Magnetic Susceptibility Observation of a Spin Reorientation Transition in Fe/2 ML Ni(111)/W(110) Films*. Phd in physics, McMaster University, 1997.

[108] D. C. Meeker. Finite element method magnetics, version 4.0.1. http://femm.foster-miller.net/, 03Dec2006 Build.

[109] P. Le Boulanger, J. L. Doualan, S. Girard, J. Margerie, R. Moncorge, and B. Viana. Excited-state absorption of Er3+ in the $Ca_2Al_2SiO_7$ laser crystal. *Journal of Luminescence*, 86(1):15–21, 2000.

[110] J. Hartmann, P. Voigt, and M. Reichling. Measuring local thermal conductivity in polycrystalline diamond with a high resolution photothermal microscope. *Journal of Applied Physics*, 81(7):2966–2972, 1997.

[111] P. Le Boulanger, J.-L. Doualan, S. Girard, J. Margerie, and R. Moncorgé. Excited-state absorption spectroscopy of Er3+-doped $Y_3Al_5O_{12}$, YVO_4, and phosphate glass. *Phys. Rev. B*, 60(16):11380–11390, 1999.

[112] E. Vasiliadou, G. Müller, D. Heitmann, D. Weiss, K. v. Klitzing, H. Nickel, W. Schlapp, and R. Lösch. Collective response in the microwave photoconductivity of hall bar structures. *Phys. Rev. B*, 48(23):17145–17148, 1993.

[113] Sandip Ghosh and B. M. Arora. Photoreflectance spectroscopy with white light pump beam. *Review of Scientific Instruments*, 69(3):1261–1266, 1998.

[114] A. Comin, M. Rossi, C. Mozzati, F. Parmigiani, and G. C. Banfi. Femtosecond dynamics of Co thin films on Si support. *Solid State Communications*, 129:227–231, 2004.

[115] A. Abragam and B. Bleaney. *Electron Paramagnetic Resonance of Transition Ions*. Clarendon Press, 1970.

[116] E.I. Solomon and A.B.P. Lever, editors. *Inorganic Electronic Structure and Spectroscopy, Volume I: Methodology*, chapter 2 Electron Paramagnetic Resonance Spectroscopy, Alessandro Bencini and Dante Gatteschi. John Wiley and Sons, 1999.

[117] Alessandro Bencini and Dante Gatteschi. *Electron Paramagnetic Resonance of Exchange Coupled Systems*. Springer-Verlag, 1990.

[118] Anne-Laure Barra, Dante Gatteschi, and Roberta Sessoli. High-frequency EPR spectra of a molecular nanomagnet: Understanding quantum tunneling of the magnetization. *Phys. Rev. B*, 56:8192, 1997.

[119] Dante Gatteschi, Anne Laure Barra, Andrea Canschi, Andrea Cornia, Roberta Sessoli, and Lorenzo Sorace. EPR of molecular nanomagnets. *Coordination Chemistry Reviews*, 250:1514, 2006.

[120] S. Hill, J.A.A.J. Perenboom, N.S. Dalal, T. Hathaway, T. Stalcup, and J.S. Brooks. High-Sensitivity Electron Paramagnetic Resonance of Mn_{12}-Acetate. *Phys. Rev. Lett.*, 80:2453, 1998.

[121] John G. Simmons. Generalized Formula for the Electric Tunnel Effect between Similar Electrodes Separated by a Thin Insulating Film. *Journal of Applied Physics*, 34(6):1793–1803, 1963.

[122] John G. Simmons. Electric Tunnel Effect between Dissimilar Electrodes Separated by a Thin Insulating Film. *Journal of Applied Physics*, 34(9):2581–2590, 1963.

[123] G. Mattei, C. Maurizio, C. de Julian Fernandez, P. Mazzoldi, G. Battaglin, P. Canton, E. Cattaruzza, and C. Scian. Size dependent hcp-to-fcc transition temperature in Co nanoclusters obtained by ion implantation in silica. *Nucl. Instr. and Meth. B*, 250:206, 2006.

[124] P. B. Johnson and R. W. Christy. Optical constants of transition metals: Ti,V,Cr,Mn,Fe,Co,Ni and Pd. *Phys. Rev. B*, 9(12):5056 – 5070, 1974.

[125] R. Kubo. Electronic Properties of Metallic Fine Particles. I. *J. Phys. Soc. Jpn.*, 17:975, 1962.

[126] R. Kubo, A. Kawabata, and S. Kobayashi. Electronic Properties of Small Particles. *Annu. Rev. Mater. Sci.*, 14:49, 1984.

[127] O. Madelung. *Introduction to Solid-State Theory*. Springer, 1995.

[128] Oleg A. Yeshchenko, Igor M. Dmitruk, Alexandr A. Alexeenko, and Andriy M. Dmytruk. Optical properties of sol-gel fabricated Ni/SiO_2 glass nanocomposites. *J. Phys. Chem. Solids*, 69:1615, 2008.

[129] Gustav Mie. Beiträge zur Optik trüber Medien, speziell kolloidaler Metallösungen. *Ann. Phys.*, 25(3):377, 1908.

[130] C. Maetzler. MATLAB Functions for Mie Scattering and Absorption. Research report no. 2002-08, Institut fr Angewandte Physik, Universitaet Bern, 2002.

[131] T. C. Bond, G. Habib, and R. W. Bergstrom. Limitations in the enhancement of visible light absorption due to mixing state. *J. Geophys. Res.*, 111:D20211, 2006.

[132] R. W. Teale and D. W. Temple. Photomagnetic anneal, a new magneto-optic effect, in Si-doped yttrium iron garnet. *Phys. Rev. Lett.*, 19(16):904, 1967.

[133] Jr. J. F. Dillon, E. M. Gyorgy, and J. P. Remeika. Photoinduced Magnetic Anisotropy and Optical Dichroism in Silicon-Doped Yttrium Iron Garnet. *Phys. Rev. Lett.*, 22(13):643, 1969.

[134] Richard Alben, E. M. Gyorgy, Jr. J. F. Dillon, and J. P. Remeika. Polarization-Dependent Photoinduced Effects in Silicon-Doped Yttrium Iron Garnet. *Phys. Rev. B*, 5(7):2560, 1972.

[135] A. K. Giri, E. M. Kirkpatrick, P. Moongkhamklang, and S. A. Majetich. Photomagnetism and structure in cobalt ferrite nanoparticles. *Appl. Phys. Lett.*, 80(13):2341, 2002.

[136] R.P. del Real, G. Rosa, and H. Guerrero. Magneto-optical apparatus to measure ac magnetic susceptibility. *Rev. Sci. Instr.*, 75:2351, 2004.

[137] Xiaobin Wang and H. Neal Bertram. Field and temperature-dependent attempt frequency for dynamic-thermal reversal of interacting magnetic grains. *J. Appl. Phys.*, 92(8):4560, 2002.

[138] A. Hernando, P. Crespo, and M. A. Garcia. Metallic magnetic nanopaticles. *The Scientific World Journal*, 5:xxx–xxx, 2005.

[139] P. Kluth, B. Hoy, B. Johannessen, S. G. Dunn, G. J. Foran, and M. C. Ridgway. Formation and characterization of nanoparticles formed by sequential ion implantation of Au and Co into SiO_2. *Nucl. Instr. and Meth. B*, 257:80, 2007.

[140] F. Wilhelm, P. Poulopoulos, V. Kapaklis, J.-P. Kappler, N. Jaouen, A. Rogalev, A. N. Yaresko, and C. Politis. Au and Fe magnetic moments in disordered Au-Fe alloys. *Physical Review B (Condensed Mater and Materials Physics)*, 77(22):224414, 2008.

[141] X. Y. Li, L. T. Kong, and B. X. Liu. Enhanced magnetic moment of Fe in fcc-structured Fe-Ag and Fe-Au alloys synthesized by ion-beam manipulation. *Physical Review B (Condensed Mater and Materials Physics)*, 72(5):054118, 2005.

[142] Lin Guo, Qunjian Huang, Xiao yuan Li, and Shihe Yang. Iron nanoparticles: Synthesis and applications in surface enhanced Raman scattering and electrocatalysis. *Physical Chemistry Chemical Physics*, 3(9):1661–1665, 2001.

[143] T. Hollstein, U. Kreibig, and F. Leis. Optical Properties of Cu and Ag in the Intermediate Region between Pure Drude and Interband Absorption. *Physica Status Solidi (b)*, 82:545 – 556, 1977.

[144] H. Hövel, S. Fritz, A. Hilger, U. Kreibig, and M. Vollmer. Width of cluster plasmon resonances: Bulk dielectric functions and chemical interface damping. *Phys. Rev. B*, 48(24):18178–18188, Dec 1993.

[145] W. Weber, D. A. Wesner, D. Hartmann, and G. Güntherodt. Spin-polarized interface states at the Pd(111)/Fe(110), Pd(111)/Co(0001), and Pt(111)/Co(0001) interfaces. *Phys. Rev. B*, 46(10):6199–6206, 1992.

[146] Satoshi Tomita, Takeshi Kato, Shigeru Tsunashima, Satoshi Iwata, Minoru Fujii, and Shinji Hayashi. Magneto-Optical Kerr Effects of Yttrium-Iron Garnet Thin Films Incorporating Gold Nanoparticles. *Phys. Rev. Lett.*, 96:167402, 2006.

[147] Joel S. Miller and Marc Drillon, editors. *Magnetism: Molecules to Materials*, chapter 14 Magnetic Langmuir-Blodgett Films, Christophe Mingotaud, Pierre Delhaes, Mark W. Meisel and Daniel R. Talham. Wiley-VCH, 2000.

[148] Francesco Pineider, Matteo Mannini, Roberta Sessoli, Andrea Caneschi, Davide Barreca, Lidia Armelao, Andrea Cornia, Eugenio Tondello, and Dante Gatteschi. Solvent Effects on the Adsorption and Self-Organization of Mn_{12} on Au(111). *Langmuir*, 23:11836 – 11843, 2007.

[149] R. G. Nuzzo and D. L. Allara. Adsorption of bifunctional organic disulfides on gold surfaces. *J. Am. Chem. Soc.*, 105:4481 – 4483, 1983.

[150] Monica Soler, Wolfgang Wernsdorfer, Ziming Sun, John C. Huffman, David N. Hendrickson, and George Christou. Single-molecule magnets: control by a single solvent molecule of jahn-teller isomerism in $[Mn_{12}O_{12}(O_2CCH_2Bu^t)_{16}(H_2O)_4]$. *Chem. Commun.*, pages 2672 – 2673, 2003.

[151] Matteo Mannini, Philippe Sainctavit, Roberta Sessoli, Christophe Cartier dit Moulin, Francesco Pineider, Marie-Anne Arrio, Andrea Cornia, and Dante Gatteschi. XAS and XMCD investigation of Mn_{12} monolayers on gold. *Chem. Eur. J.*, 14:7530 – 7535, 2008.

[152] Claus J. H. Jacobsen, Erik Pedersen, Joergen Villadsen, and Hoegni Weihe. ESR characterization of trans-diacidatotetrakis(pyridine)vanadium and -manganese trans-VII(py)4X2 and trans-MnII(py)4X2 (X = NCS, Cl, Br, I; py = pyridine). *Inorganic Chemistry*, 32(7):1216–1221, 1993.

[153] Lorenzo Sorace. *Magnetism and magnetic anisotropy of spin clusters*. Dottorato di ricerca in scienze chimiche, Dipartimento di Chimica – Università degli Studi di Firenze, 2001.

[154] Shuming Nie and Steven R. Emory. Probing Single Molecules and Single Nanoparticles by Surface-Enhanced Raman Scattering. *Science*, 275:1102, 1997.

[155] Gabriel Shemer and Gil Markovich. Enhancement of Magneto-Optical Effects in Magnetite Nanocrystals Near Gold Surfaces. *J. Phys. Chem. B*, 106:9195 – 9197, 2002.

[156] Itai Lieberman, Gabriel Shemer, Tcipi Fried, Edward M. Kosower, and Gil Markovich. Plasmon-Resonance-Enhanced Absorption and Circular Dichroism. *Angew. Chem. Int. Ed.*, 47:4855 – 4857, 2008.

[157] Yanqiu Li, Qiang Zhang, Arto V. Nurmikko, and Shouheng Sun. Enhanced Magnetooptical Response in Dumbbell-like Ag-$CoFe_2O_4$ Nanoparticle pairs. *Nano Lett.*, 5:1689, 2005.

[158] R. Sessoli and M. Mannini et al. *to be published*.